MSc.Thesis

Scaling Methodology for Buckling of Composite Conical Shells in Axial Compression

K. Pareyns

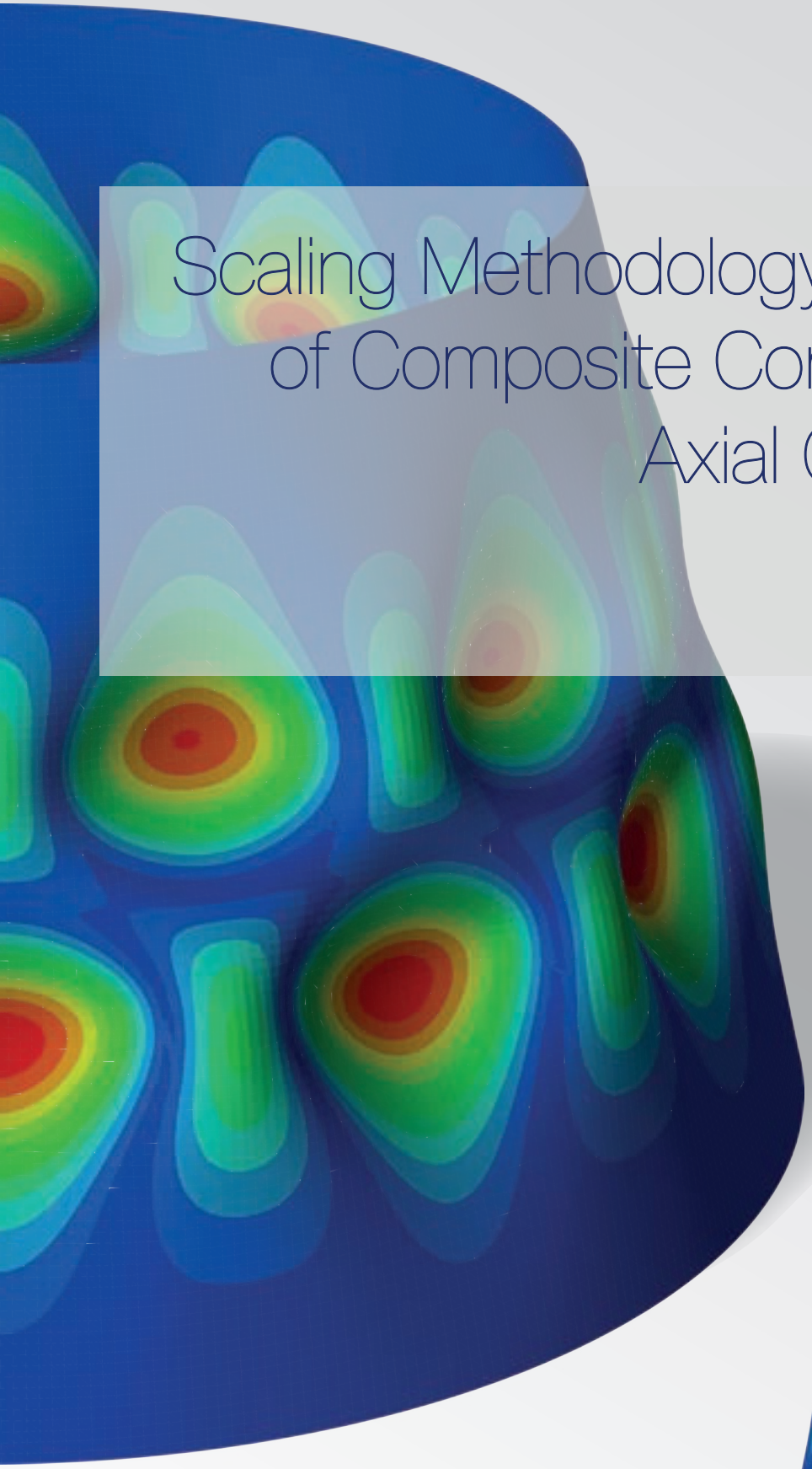

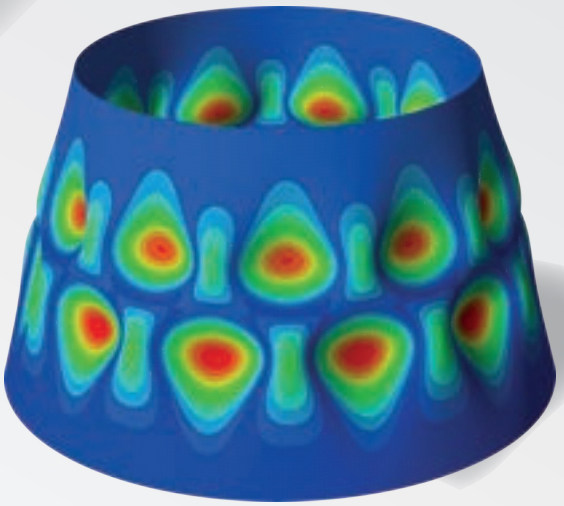

TU Delft

Scaling Methodology for Buckling of Composite Conical Shells in Axial Compression

Master of Science Thesis

For obtaining the degree of Master of Science in Aerospace Engineering
at Delft University of Technology

K. Pareyns

26 May 2021

Faculty of Aerospace Engineering · Delft University of Technology

Delft University of Technology
Faculty of Aerospace Engineering
Department of Aerospace Structures and Materials

GRADUATION COMMITTEE

Dated: 26 May 2021

Chair holder:

Prof. Dr. Chiara Bisagni

Committee members:

Dr. Sergio R. Turteltaub

Dr. Julie J.E. Teuwen

Dr. Marc R. Schultz

Abstract

Launch vehicle structures are commonly composed of cylindrical and conical shells, which are inherently sensitive to buckling. The axial compression experienced during launch can consequently be a sizing load case, so it is important to understand the axial buckling behavior of these shells. Experimental testing is an essential part of studying this phenomenon because manufacturing imperfections can cause large discrepancies between theory and reality. In addition, conical shells have been researched less frequently than cylindrical shells, such that their behavior is less well understood. Experimental testing of launch vehicle structures is difficult and expensive due to their large size, hence it is preferred to test reduced-scale shells, representative of the full-scale ones. In this thesis, a scaling methodology is developed which allows designing representative reduced-scale conical shells for full-scale composite conical shells buckling in axial compression.

The conical shells are assumed to have a symmetric, balanced layup with negligible flexural anisotropy. The scaling methodology is developed using the nondimensional governing equations, obtained through Nemeth's procedure, which allows to directly use the coefficients of the equations as scaling parameters. It also provides a framework to not only compare the buckling load of the shells of different sizes, but also the displacement upon buckling, the deformation shape, and the radial displacement. The methodology is set up such that the reduced-scale design parameters are determined sequentially. The buckling behavior of the two shells is compared using a semi-analytical approach, linear eigenvalue, and implicit dynamic finite element analyses. The eigenmode imperfection sensitivity is also evaluated.

The methodology is successfully applied to isotropic, cross-ply, quasi-isotropic, and sandwich conical shells. The prediction accuracy is mainly affected by not being able to simultaneously satisfy all scaling parameters, by non-negligible flexural anisotropy and transverse shear, and by differences in imperfection sensitivity between the full-scale and reduced-scale shells. In any case, accurate results are obtained for the considered shells. The radial displacement is most difficult to predict, which is attributed to the membrane prebuckling assumption and neglecting the presence of imperfections. Finally, it is observed that larger eigenmode imperfections affect the accuracy, but they do not cause the methodology to fail. For future work, it is recommended to validate the methodology through experimental testing.

Acknowledgments

A year devoted to research work becomes much more interesting and manageable if the topic is fascinating and truly intrigues you. I was lucky to be in this position. Studying the buckling behavior of conical shells combined what I was looking for in research: a captivating application, an extensive analytical framework, and interesting numerical simulations.

Although the interest in the research has been important, the support of many people around me was crucial. First of all, I would like to express my gratitude towards my supervisor, Prof. Chiara Bisagni. Her guidance and expertise were essential for the successful completion of this work. She taught me that progressing slowly and taking your time to fully understand a concept will only help in achieving good results. She also gave me the opportunity to work together with Michelle and Marc from NASA. I would like to thank them for the collaboration and fruitful feedback on the work. Although Michelle was not there during part of the time, knowing that I could reach out to her for suggestions and a second opinion was comforting. Additionally, I would like to express my thanks to Ines for her advice and insights on shell buckling behavior and nondimensional scaling.

I also would like to thank my friends for the necessary distractions and the memorable time in Delft. I hope we can soon celebrate our graduations all together. In particular, I would like to thank Flores, my number one to-go-to for all of my questions in the past six years. I am very happy that our paths have been running parallel, so close together that some people still do not know the difference between us. Next, I cannot imagine how the past year would have been without the continuous support from Isaac, my boyfriend. Thank you for listening to my complaints, putting everything in perspective, and never failing to make me smile.

Finally, there are no words to describe how grateful I am for the support of my parents. Without them, I would not be where and who I am today. I would like to thank them for the possibility to study in Delft, the continuous encouragements, and the enlightening talks.

Kaat Pareyns
Delft, May 2021

Table of Contents

List of Figures

List of Tables

Chapter 1

Introduction

In recent years, there is a revival of interest in space exploration. This is exemplified by the Artemis program from NASA [1] and the Mars & Beyond mission from SpaceX [2]. Because of this increasing interest, the need for reliable and economical launch vehicles is larger than ever. Launch vehicle structures are typically composed of thin-walled components, such as cylindrical and conical shells. Truncated conical shells are commonly used between and on top of cylindrical shells as stage and payload adapters. A sizing load case for the launch vehicle structure is the axial compression caused by the upward pushing thrust and downward pushing payload weight. Axial compression can lead to buckling, which causes loss of stability and consequently to possible mission failure.

Although conical shells are often used for engineering applications, their stability behavior is not yet fully understood. One of the reasons for this is the large difference between theoretical predictions and experimental results, which is mainly caused by the presence of imperfections. These imperfections can be originated by the manufacturing process and are consequently not known during the design phase. This makes it difficult to account for them, thus resulting in design approaches, such as the NASA SP-8019 guidelines [3]. These guidelines are based on tests with isotropic conical shells performed in the 1960s and are considered conservative for the composite shells used nowadays. New design approaches are therefore being investigated, such that lighter launch vehicles can be developed.

Experimental testing plays a fundamental role in studying the buckling behavior and the development of these new design methods. This is, however, challenging and expensive for large-size components. It is therefore preferred to test reduced-scale conical shells, representative of the full-scale ones. The design of these reduced-scale equivalents is not straightforward because the stability behavior is complex and influenced by many parameters, such as the composite layup, dimensions and material. Scaling of conical shells has not been done much in the past. The few applications do not rely on a clearly defined scientific basis, such that the scaling does not cover the complete phenomenon. Scaling approaches have been developed for other structures, such as plates and cylindrical shells. One of the most promising ones is scaling through the nondimensional governing equations. The nondimensional nature allows to use the coefficients of the equations as scaling laws and it simplifies the comparison of

shells of different sizes. Because the governing equations are used, the buckling phenomenon is covered as a whole within the limits of its assumptions. As a result, not only the buckling load, but also the displacement, the deformation shape, and the radial displacement can be scaled.

The research performed for this thesis focuses on the development of a nondimensional scaling methodology for conical shells buckling in axial compression. The work is undertaken in a framework of collaboration between the TU Delft and the NASA Langley Research Center. First, a literature review is performed to understand the state-of-the-art regarding the stability behavior of conical shells, as well as regarding scaling methodologies. From this study, the research objective is defined. Second, the nondimensional governing equations are derived analytically and the scaling methodology is developed. Third, it is explained which methods are used for the analysis of the conical shells. This also includes a discussion of how the scaling methodology is evaluated based on the nondimensional parameters. Next, the methodology is applied to several cases. In chapter 5 and chapter 6, an isotropic and a cross-ply conical shell are scaled, respectively. In chapter 7, the scaling of a quasi-isotropic composite shell is discussed and chapter 8 covers the scaling of a sandwich shell. Finally, the thesis is completed with the conclusions and recommendations.

Chapter 2

Literature Study

Conical shells are commonly used in engineering applications, such as pipelines, submarines and launch vehicles. They are often employed as connector pieces between cylindrical shells of different diameter. The thin-walled construction makes these structures lightweight and, in combination with the curvature, efficient in carrying in-plane loads. Another consequence of the small thickness-to-radius ratio is that the shells are sensitive to buckling, which can lead to loss of load carrying capability. As a result, one of the sizing load cases for launch vehicle shell structures is the axial compression caused by the downward pushing weight and the upward pushing thrust. To ensure a safe, yet lightweight design of the launch vehicles, it is important to understand the stability behavior of these shells. Experimental testing is essential for this because large discrepancies are observed between theoretical predictions and experimental results. This is, however, costly and difficult due to the large size of launch vehicle structures. Scaling methodologies allow to design reduced-scale structures, which are representative of the full-scale structures and which can be tested in a cheaper and more convenient way. The development of these methodologies is not straightforward due to the complexity of the buckling phenomenon.

A literature study is performed on this topic. It sketches the framework in which the thesis is performed and highlights existing research gaps. First, the theoretical and experimental research on the stability behavior of conical shells in axial compression is discussed. Second, commonly used design approaches for conical shells are explained. Third, existing scaling methodologies for shell structures are elaborated upon. Based on this literature review, the research objective and questions for the thesis are defined.

2.1 Stability of Conical Shells

Conical shells have been researched remarkably less than cylindrical shells. This is commonly attributed to the higher complexity in theoretical analysis and manufacturing processes. Therefore, conical shells are sometimes analyzed as equivalent cylindrical shells, based on the similarities between the two shell types. At the same time, there are important differences between cylindrical and conical shells, such that this approach is not considered reliable.

For example, the shells have a different sensitivity to imperfections and the cone angle influences the stability behavior. It is consequently important to investigate the buckling behavior of conical shells separately. This section discusses the theoretical and experimental research performed on this topic. [4, 5]

The structure under consideration is shown in Figure 2.1a: a truncated thin-walled conical shell compressed by an axial load P. The conical shell is assumed to be made of a composite material, which is typically used for applications in which weight plays an important role. The corresponding load-displacement curve is visualized in Figure 2.1b. Upon a certain load, the critical buckling load P_{cr}, the structure becomes unstable and starts to buckle. This can be seen in Figure 2.1b by a sudden drop in load. The buckling behavior is different for a geometrically perfect shell (subscript "per") than for a shell with imperfections (subscript "imp"). This difference will be investigated here as well.

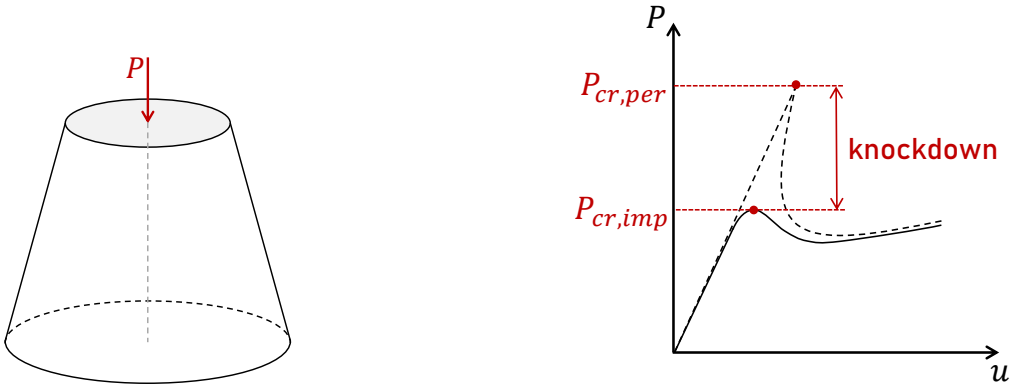

(a) Truncated conical shell under axial compression loading.

(b) Load-displacement curve of the conical shell on the left.

Figure 2.1: Geometry and load-displacement curve of a truncated conical shell under axial compression, after [6].

2.1.1 Analytical Work

It was mentioned above that the theory describing the stability behavior of conical shells in axial compression is complex. More specifically, the behavior is typically described by a set of nonlinear partial differential equations with variable coefficients. Ventsel and Krauthammer [7] and Brush and Almroth [8] give clear overviews of shell theories applicable to conical shells. The nonlinearity and variable coefficients complicate the calculation of the buckling load considerably. A fast analytical tool is preferred for buckling predictions in the early stages of the design [9]. In 1956, Seide [10] derived an analytical solution for the buckling load of an isotropic conical shell in axial compression. The solution P_{cr} is similar to the solution of the cylindrical shell P_{cyl}, and is given by

$$P_{\text{cr}} = \frac{2\pi E t^2 \cos^2 \alpha}{\sqrt{3(1-\nu^2)}} = P_{\text{cyl}} \cos^2 \alpha \,. \tag{2.1}$$

In Equation 2.1, E is the Young's modulus, t the thickness, ν the Poisson's ratio and α the cone angle, measured between the central axis and the inclined surface. This equation

allows for a fast first-order estimation of the buckling load of the shell. One can see that this equation does neither depend on the boundary conditions of the conical shell, nor on the length and radii. It is believed, however, that these parameters have an influence on the buckling performance. For example, the boundary conditions have a stiffening effect on the conical shell, such that a shorter shell has a higher buckling load [6, 11]. In addition, Seide's equation is only valid for isotropic shells. For composite shells, no closed-form solution is available [9]. Many authors have attempted to develop new solution methods or to improve the equation from Seide by taking into account different boundary conditions, statistical test data, the pre-buckling deformation, etc. A compact summary hereof is given by Khakimova [6] and Kazemi et al. [12].

2.1.2 Experimental Testing

To gain a better understanding of the real behavior of structures, experimental tests are carried out. These tests allow to validate and improve theoretical work and to reveal unpredicted phenomena. A typical test setup of a conical shell subjected to axial compression is shown in Figure 2.2.

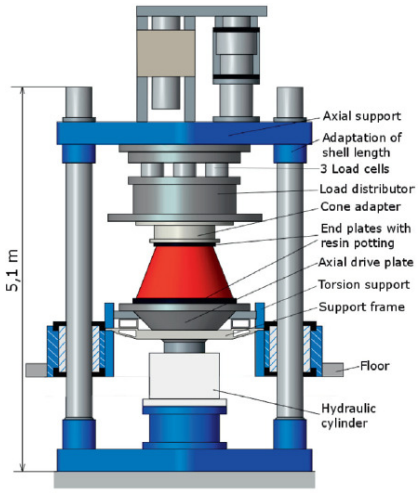

Figure 2.2: Experimental setup for testing a conical shell [13].

At the German Aerospace Center DLR, three composite conical shells, named K01, K06, and K08, were tested in axial compression using the test setup shown in Figure 2.2 [13]. The shell is shown in the middle in red, the black rings on the top and bottom are aluminum end plates with resin potting, in which the edges of the shell are embedded. They allow for uniform load introduction in the shell and for clamping the shell in the machine. During the test, the loads and displacements are recorded via load cells and displacement transducers,respectively. The displacement data is not only used for measurements, but also for controlling the test speed. Buckling experiments are typically displacement controlled, because the load suddenly drops upon buckling while the displacement still increases. If the test would be force controlled, the machine would keep on increasing the load, thus damaging the shell. Finally, 18 strain gauges in a back-to-back configuration are attached to the shell and a DIC system is used to measure and visualize the out-of-plane displacements.

In 2017, Khakimova [6] gave an overview of the buckling experiments carried out on conical

shells since 1961. This overview is consistent with the one given by Ifayefunmi [5] in 2014. According to this list, 19 axial compression buckling experiments have been carried out on isotropic (metal and plastic) conical shells. Often, these shells are rather thick, such that they buckle in the plastic regime. Only six tests were performed on composite conical shells, of which four in axial compression. No more recent literature (after 2017) has been found documenting buckling experiments on composite conical shells in axial compression. The lack of test campaigns can be explained by the corresponding costs and difficulties, especially for large structures, such as launch vehicle components. The amount of effort put into the process is consequently not always balanced with the usefulness of the test data [14, 15].

2.1.3 Discrepancy between Theory and Experiments

When comparing the test data to the theoretical predictions from analytical and numerical models, large discrepancies are observed. The buckling load found during experiments can be several factors smaller than the load predicted by shell buckling theory [3, 16]. Koiter [17] was the first one in 1945 to prove for cylindrical shells that geometric imperfections are responsible for the discrepancy and that the degree of imperfection sensitivity depends on magnitude and shape of the initial imperfections. This is visualized in Figure 2.1b by the knockdown arrow, indicating the difference in reaction load for the perfect and imperfect case. Three imperfection types are typically distinguished: geometric imperfections, loading or boundary imperfections, and stiffness imperfections [18]. These defects are mainly caused by the test setup and the manufacturing process. Below, each of the imperfections is shortly discussed.

Geometric imperfections Geometric imperfections, also called traditional or mid-surface imperfections, are most commonly researched. Geometric imperfections are typically defined as the deviation from the best-fit conical shell [18]. The measured imperfections of the K08 shell previously discussed are associated with the adopted ply piece topology during manufacturing and with the potting of the shell in the end rings, which may have deformed the shell [13]. As explained in subsection 2.1.2, not many conical shells have been tested. Logically, there is also not much data available on measured geometric imperfections. Therefore, geometric imperfection data from cylindrical structures is sometimes scaled to a conical shape and used as measured imperfections input in finite element models. This is, for example, done by Di Pasqua et al. [19] and Sleight et al. [20]. It should be noted that this is not always representative, because imperfection patterns are associated with specific production processes [21, 22].

Loading and boundary imperfections Loading and boundary imperfections are imperfections caused by the test setup. They are attributed to non-uniform load introduction and imperfect boundary conditions. An additional difficulty arises for loading and boundary imperfections due to the unknown loading condition in reality, versus the loading condition during tests.

Due to the inclined surface, it is more difficult to accurately model the boundary conditions for conical shells than for cylindrical shells. In this light, Chryssanthopoulos and Spagnoli [23] compared two types of edge constraints for a stringer-stiffened conical shell. Both are shown in Figure 2.3. The cylinder edge condition restricts motion in the direction perpendicular to

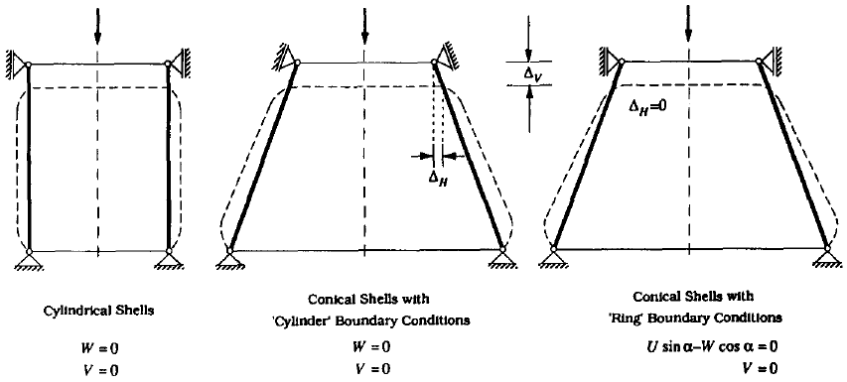

Figure 2.3: Cylinder (left and middle) and ring (right) boundary conditions [23].

the inclined surface, whereas the ring edge condition restricts motion in the direction perpendicular to the axis of revolution. The buckling load was similar for both edge constraints for the conical shell considered. The stiffness, on the other hand, was 15% lower for the ring than for the cylinder edge condition, resulting in a larger displacement upon buckling. The prebuckling deformation state is also different for the two cases. The authors recommend using the ring condition for conical shell design, as it mimics the realistic constraints given by adjacent structures, such as cylindrical shells. They also note that for conical shells with other geometric parameters, the effect of the edge condition may be larger, and the buckling load may be affected.

Stiffness imperfections Stiffness imperfections arise from a non-uniform thickness, from fiber angle variations, and from deviations from the nominal material properties [24]. Due to the varying radius of the conical shell, this imperfection is more pronounced than for cylindrical shells. Its presence is, however, often neglected due to the complexity it brings in analyses.

For metallic shells, which can be integrally machined or formed from a sheet, the thickness can be made more or less uniform within the tolerances of the manufacturing process. For a laminated shell, this is not the case: when plies are laid down next to each other on the large radius edge, they will overlap when approaching the small radius edge. Consequently, the thickness, and thus stiffness, will be larger near the small radius than near the large radius. This causes buckling initiation near the large radius, in contrast to constant stiffness shells, for which buckling initiates near the small radius, where the stresses are higher [25].

Because of the variable geometry, the fiber angle also varies along the surface of the conical shell. This logically also creates variations in stiffness [26]. Fibers can be laid down according to various paths, which determines the angle variation. The most common path is the geodesic path, which has zero in-plane curvature, meaning it is a straight line when the conical shell is folded open to a 2D structure [27]. The geodesic path occurs for conical shells made by filament winding, prepreg hand layup and automated tape layup. When fiber steering is applied, more complex paths, such as constant angle and constant curvature paths, can be obtained, which are out of the scope of this literature study [28, 29].

2.2 Design Approaches for Conical Shells

As the imperfections in conical shells are mainly caused by the production process and the test setup, the severity of their influence on the buckling behavior is not known yet during the design process. It is, however, necessary to account for it, as large discrepancies with theory exist. There are several methods available for reliable conical shell design, which will be elaborated upon here. First, the most commonly used guideline, developed by NASA, is explained. Second, the group of deterministic approaches is elaborated upon, after which the stochastic methods are discussed.

2.2.1 NASA SP-8019 Guidelines

In 1968, NASA [3] published lower-bound design guidelines for the design of conical shells in buckling. Experiments were carried out on isotropic shells, but no effect of the geometry on the factor relating experiments to theory could be found. Therefore, a lower-bound constant knockdown factor (KDF) of $\gamma = 0.33$ was advised for conical shells with cone angle between 10° and 75°. This KDF is applied to the analytical solution of Seide (see subsection 2.1.1), such that

$$P_{\text{cr}} = \gamma P_{\text{Seide}} = \gamma \frac{2\pi E t^2 \cos^2 \alpha}{\sqrt{3(1-\nu^2)}}. \tag{2.2}$$

For conical shells with a cone angle smaller than 10°, the guideline recommends using an equivalent cylinder approach. For orthotropic shells, sandwich shells with orthotropic facesheets and shells with cone angle larger than 75°, no guideline is provided, because no experimental data was available. For sandwich conical shells with isotropic face sheets, guidelines are provided. The guideline consists of formulas to calculate an equivalent stiffness and thickness, which can then be substituted in Equation 2.2. Due to lack of experimental data, the KDF is the same as for isotropic conical shells.

The shells used for the development of the SP-8019 guideline were isotropic shells, whereas nowadays the focus lies more on composites. The imperfection sensitivity of these materials is not well understood and the production processes are completely different from the processes for isotropic materials, such as metals. As a result, the required knockdown factor for a safe design is different from the one for isotropic shells. Recent analytical investigation by Sleight et al. [20] of conical sandwich shells for example showed that for all evaluated shells, the KDF was larger than 0.5. In addition, the accuracy of production processes for isotropic materials has been increased over the years, such that the SP-8019 guidelines might not be representative for shells produced nowadays. Therefore, other methods are being developed to provide a safe design guideline for orthotropic shells, as well as alternatives to the NASA guidelines for isotropic shells [21]. NASA set up a project called the Shell Buckling Knock-Down Factor (SBKDF) with the goal to develop new guidelines to calculate the KDF of shells prone to buckling [30]. In Europe, the DESICOS project (New Robust Design Guideline for Imperfection Sensitive Composite Launcher Structures) has been set up in 2012. This project focused on the single perturbation load methodology, discussed here as well [31]. Up to now, no satisfactory alternative has been found. In 2010, the European Cooperation for Space Standardization still recommended to use the SP-8019 guidelines [32]. As an alternative for the KDF of $\gamma = 0.33$, the guidelines given by the European Convention of Constructional

Steelwork [33] are suggested. Here, the KDF is calculated in terms of the top radius, thickness and cone angle of the conical shell.

2.2.2 Deterministic Approaches

Many deterministic approaches have been developed for cylindrical shells, which are also applied to conical shells or their cylindrical equivalent. Two methods are discussed here and other commonly researched approaches are mentioned, as they are out of the scope of this study.

Measured imperfections The first deterministic approach is the inclusion of measured imperfections in the model. Not only the mid-surface imperfections, but also the thickness imperfections can be measured and taken into account [13]. Loading imperfections can also be measured during the test, as done by Schultz et al. for a sandwich cylindrical shell [34]. These imperfections can be applied as a combination of an axial load and a bending moment, or as a non-uniform distributed load along the top edge. The advantage of using measured imperfections is that the perturbations are realistic. The disadvantage is that the imperfection data is not known during the design phase, so only reference data of other shells can be used. This data is less representative and hardly available, making this approach less reliable.

Eigenmode imperfections The second method is the inclusion of imperfections in the shape of eigenmodes in the model. The eigenmodes are obtained from a linear eigenvalue analysis of the perfect shell and can easily be implemented in the nonlinear analysis, as explained by Castro et al. for the commercial finite element software Abaqus [35]. The reasoning behind this method is that imperfections of this shape have a bias towards buckling and thus result in a conservative design. Sometimes even lower KDFs than the NASA guidelines are obtained, as found by Wang et al. for cylindrical shells [36]. There is no decisive answer on which and how many eigenmodes to use, neither on the amplitude. As a result, a lot of variability in the results is obtained [37].

Other methods Many other methods have been developed, including, but not limited to:

- **Single perturbation load approach (SPLA)**: A lateral concentrated load is applied to the shell to trigger typical buckling initiation [22, 38].
- **Worst multiple perturbation loads approach**: An optimization is carried out to find the worst combination of lateral loads in terms of application location and number of loads. This method is found to be more conservative than the previous method, but it is not clear how to determine the number of perturbation loads [39].
- **Single boundary perturbation approach**: A shim is locally added to the boundary to simulate boundary imperfections [18].
- **Single embedded delamination approach**: Numerically include a local delamination in the model to include the effect of this manufacturing defect [36].
- **Axisymmetric imperfections**: Axisymmetric imperfections are modeled to effectively reduce the membrane stiffness [35].

These guidelines have been developed for cylindrical shells. Khakimova [6] compared the NASA SP-8019, SPLA, measured imperfections (MSI) and linear eigenmode imperfections (LBMI) for a symmetrically laminated conical shell with a cone angle of 45°. The measured imperfections are the imperfections of four cylindrical shells scaled to the conical shell under consideration. The perturbation load for the SPLA is applied halfway the conical shell's height and perpendicular to the surface. The comparative graph is shown in Figure 2.4. The curve for the eigenmode imperfection does not converge, such that the KDF is lower than the NASA SP-8019 guideline for imperfections with an amplitude of 60% of the thickness and larger. The SPLA is less conservative than the eigenmode imperfection, but more conservative than the measured imperfections. The SPLA was also applied numerically and experimentally to the K01, K06 and K08 conical shells discussed in subsection 2.1.2 [16].

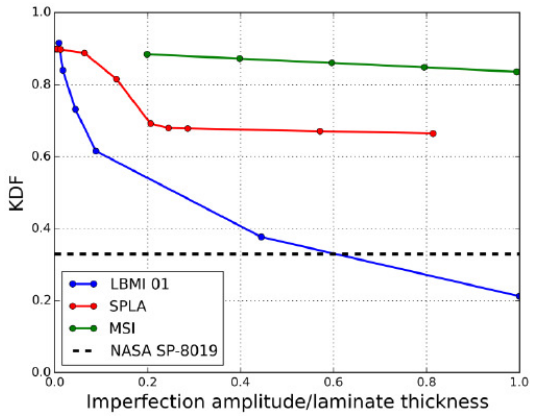

Figure 2.4: Knockdown factor for the four design approaches considered by Khakimova [6].

2.2.3 Stochastic Approaches

Stochastic approaches are reliability-based methods, making use of the probability distribution of the parameters influencing the buckling behavior. The objective function of this stochastic problem is the buckling load, which depends on parameters, such as the imperfection pattern, material properties and ply orientation. If one wishes to say something about the probability of the buckling load being above or below a certain value, one needs to take the integral of the probability density function of these influencing parameters. This integral cannot be solved analytically, so one either uses a semi-analytical approach, such as the first-order second-moment analysis, or a purely numerical one, such as the Monte Carlo method [22,40]. No examples in literature were found applying stochastic approaches to buckling of conical shells. This may be caused by the limited experimental data available, which makes it more difficult to assume reliable distributions for imperfections. For applications to cylindrical shells, one may consult references [24, 40–42].

2.2.4 Finite Element Modeling Techniques

As experimental testing is expensive and analytical solutions are not available or not able to predict the buckling behavior accurately, a lot of numerical analyses are performed. Usually, finite element analyses are performed in commercial software packages such as Abaqus, Nastran and Ansys. This section elaborates on the type of solvers and elements used for modeling

the buckling behavior of shell structures, as well as the modeling of loads and boundary conditions. Note that the focus lies on the solvers and elements in Abaqus, as this software will be used for the research.

Solvers Shell buckling is a nonlinear phenomenon, thus nonlinear analyses are required. This is, however, computationally expensive compared to linear analyses. It is observed that usually in literature a linear analysis is performed first. This gives a first idea of the buckling load. If desired, the linear eigenmode can be easily implemented as an initial imperfection in the nonlinear analysis [35]. There are several nonlinear solvers available in Abaqus. The commonly used static nonlinear solver is the Newton-Raphson (with artificial damping) method and the Riks method. The dynamic solvers can be either explicit or implicit. The dynamic analysis is capable of following the post-buckling path [32]. The static analysis can follow the behavior up to the buckling load. It may not fully capture the discontinuous post-buckling behavior, because it uses tangent lines at the current solution point to find the next solution point. This can be overcome by adding artificial damping to the Newton-Rapshon iterative solver.

For conical shells, the Newton-Raphson procedure with artificial damping is most commonly used as nonlinear solver [13, 16, 19, 43]. In all cases, a damping factor of 10^{-7} is adopted. Wagner et al. [18] used the Newton-Raphson solver to model the Vega interstage 1/2, but as they were not interested in the post-buckling regime, no damping was used. Sleight et al. [20] analyzed sandwich conical shells using a combination of a nonlinear static analysis and a nonlinear transient analysis. For research focused on fiber paths and variable stiffness, only linear eigenvalue analyses are carried out, as they are computationally cheaper [29, 44].

Element Types Another important aspect for the numerical modeling of shell buckling is the choice of the element type. The most commonly used element for analyses of shell structures is the S4R element, a 4-node quadrilateral shell element with reduced integration. Each node has six degrees of freedom. The reduced integration is used to avoid shear locking, which would cause the element to behave overly stiff. Due to the linear interpolation, the transverse shear estimation may become inaccurate for thicker shells. For this, the quadratic element S8(R) can be used. This is an 8-node quadrilateral shell element. This element type is also often used in literature for sandwich shell structure analysis. As a guideline, it is suggested to use quadratic elements if the thickness is larger than 1/15 of the characteristic length of the shell. [45]

Di Pasqua et al. [46] performed a convergence analysis for conical shells with various cone angles, ranging from $\alpha = 15°$ to $\alpha = 75°$. The element type is selected to be the S8R element, based on the results from Castro et al. [35] for cylindrical shells. They consequently analyze conical shells subjected to a lateral perturbation load (SPLA) using the Newton-Raphson solver with artificial damping. The settings for the solver are given in Table 2.1. These settings were consequently used by Di Pasqua et al. [19] and Khakimova et al. [16, 43] as they analyzed the same or similar conical shells.

Loads and Boundary Conditions The boundary conditions and loads in the finite element are usually idealizations of the real ones. For example, the boundary conditions are simplified as fully simply supported or fully clamped, while in reality this is not achievable. The axial compression load for the stability problem is usually introduced as a displacement, rather than a load, similar to the experimental test explained in subsection 2.1.2. Khakimova [6] linked

Table 2.1: Finite element parameters determined by Di Pasqua et al. [46].

Element type	S8R
Number of elements around circumference (top radius)	140
Damping factor	10^{-7}
Minimum increment size	10^{-7} (for $\alpha = 15°$) and 10^{-6} (other)
Initial increment size	0.001
Maximum increment size	0.001
Maximum number of increments	10^5

the nodes of the top edge of the conical shell to a reference point through pin constraints. These constraints act as rigid links, so they do not deform. The axial displacement is then introduced at the reference point, from which it is propagated to the nodes of the top edge. Sleight et al. [20] used the same modeling technique for load and boundary conditions for the sandwich conical shell, but used multi-point constraints.

2.3 Scaling Methodologies for Shell Structures

Although many design approaches have been developed, experimental testing is still a fundamental part of the design and study of shell structures. These structures, for example launch vehicle components, can be rather large, measuring several meters in diameter and length. This requires equal-size equipment for manufacturing and testing, which is costly and complex. Therefore, it is preferred to test reduced-scale structures. The design of representative reduced-scale structures can, however, be challenging. The reduced-scale structure should exhibit the same buckling shape and the buckling load should be scalable to the full-scale structure. Next to this, the scaled structure must stay within the manufacturing and testing facility constraints. [47]

This section elaborates on the currently existing scaling methodologies. First, the theory behind scaling is explained. Then, three scaling methods are explained in detail, after which other methods are shortly highlighted. This is followed by subsection 2.3.6, which gives examples of scaling applied to conical shells. The focus of the section will be on shell structures, but will unavoidably also consider the scaling of beam and plates, which knows a longer history than the scaling of shells.

2.3.1 Similitude Theory

The science behind representative scaling is the similitude theory. It deals with formulating the necessary and sufficient conditions for similarity between two or more systems. The behavior of a system is governed by several parameters, by which the system can also be mathematically described. These parameters are for example the geometry and material. Similitude theory establishes the relations between the mathematical descriptions, such that the full-scale design can be transformed to the reduced-scale design and vice versa [48, 49]. These relations are called scaling laws. Mathematically, it can be put this way. The parameters describing the full-scale system can be structured in a vector $\mathbf{X}_{\mathrm{FS}}$. Similarly, the parameters of the reduced-scale system can be put in a vector $\mathbf{X}_{\mathrm{RS}}$, of same length as $\mathbf{X}_{\mathrm{RS}}$. The two vectors can be related through transformation matrix $\mathbf{\Lambda}$, such that

$$\mathbf{X}_{\mathrm{FS}} = [\mathbf{\Lambda}]\mathbf{X}_{\mathrm{RS}}\,. \tag{2.3}$$

In its simplest form, the transformation matrix is a diagonal matrix. If there are less scaling laws than parameters governing the behavior, there is design freedom for the scaled structure. If the scaling laws are too restricting and conflict with manufacturing or test constraints, one can opt to disobey one or more scaling laws. This is referred to as partial similarity and partially similar models. In this case, more design freedom may be obtained, at the expense of a lower degree of similarity. Depending on which scaling law is relaxed, the obtained similarity may be acceptable or not; the influence of some scaling parameters is smaller than that of others [50]. If all scaling laws are fulfilled, complete similarity is obtained.

Similitude theory and scaling know a long history, of which Coutinho et al. [15] give a clear overview up to 2015. Casaburo et al. [14] also recently published a review of similitude methods. Both review papers extensively refer back to a review by Simitses et al. [51], which gives a clear explanation on size effects and similitude through governing equations, including detailed examples. Casaburo et al. [14] provide historical overviews of the methods, applications and engineering fields dealing with similitude theory, visualized in Figure 2.5. The most investigated structures are beams and unstiffened plates. For shells, only cylinders have been studied. The dimensional analysis method (DA) was the first method developed, followed by similitude theory applied to governing equations (STAGE). It should be noted that the theory of similitude existed already three decades earlier, in 1915 [15]. Around 1980, the empirical similarity method (ESM) was studied. More recently, asymptotical scaled modal analysis (ASMA), energy methods (EM), and asymptotic models for structural-acoustic research applications (SAMSARA) and sensitivity analyses (SA) were used to design scaled structures. Similitude theory was first applied to aerospace applications, such as launch vehicles and space stations, after which other engineering fields followed. Impact engineering has an extensive research background in scaling, especially through dimensional analysis.

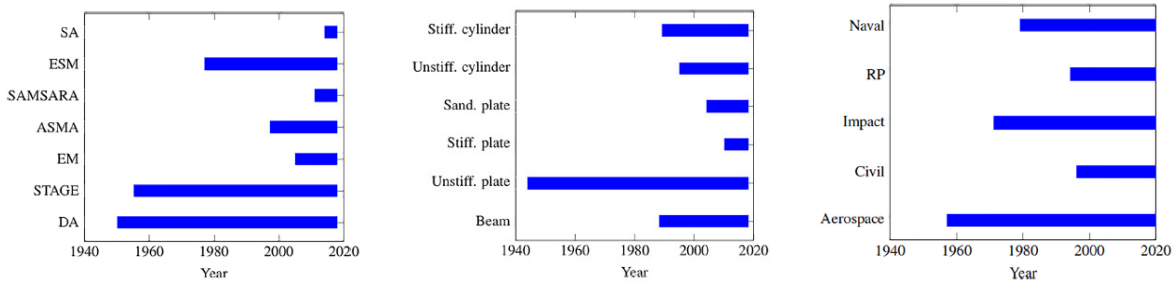

(a) Timeline per method. **(b)** Timeline per application. **(c)** Timeline per engineering field.

Figure 2.5: Historical overview of similitude theory [14].

One of the sources of confusion in similitude theory is the difference between scale and size effect. Simitses et al. [51] extensively discussed this. They define scaling effects as "... the effect of changing the geometric dimensions of a structure or structural component on the response to external causes." [51]. A force is an example of an external cause. Size effects, on the other hand, are concerned with changes in material strength or stiffness due to the physical scaling process [14]. It is not sure whether the latter effect actually exists and if yes, which properties it affects [51,52]. Furthermore, the size effect is generally neglected: material

properties obtained from coupon testing are used as input for large-scale structures design. For the development of scaling methodologies, the effects are usually also neglected [14].

2.3.2 Dimensional Analysis

The dimensional analysis approach is typically applied when the governing equations are unknown or difficult to achieve, while all physical variables influencing the system are known [14, 49]. The methodology consists of creating a set of independent dimensionless parameters according to Buckingham's Π theorem. This theory summarizes the concepts related to dimensional homogeneity: if an equation describes a physical phenomenon, then the two sides of the equation should have the same dimensions. For the scaling methodology, one establishes nondimensional parameters as products of the variables influencing the system's behavior [15, 48]. The obtained parameters are the scaling laws, which are not unique. The choice of parameters, however, is not arbitrary; some parameters are more convenient to control when searching for a scaled configuration of a system and are consequently easier to work with [14]. The analyzer should consequently be experienced and have an in-depth understanding of the physical problem.

From the 1960s, NASA performed a lot of work on the scaling of launch vehicles and space stations, mainly focusing on the vibration response. NASA investigated the vibration characteristics of the Saturn I and the Saturn V through scaled models [53, 54]. Penning [55] reported on the scaling of the second stage of the Saturn V to a 1/20 size system. The most important scaling laws are found to be the geometric scaling laws and the material scaling law, stating that the Young's modulus to density ratio should be the same for full-scale and reduced-scale structures. The adapter of the third to second stage is a conical shell and is scaled by approximating it as an equivalent cylindrical shell with the radius equal to the average radius of the conical shell. The scaling methodology is applied to this cylindrical shell, such that an equivalent cylindrical reduced-scale shell is obtained. This is then translated back to obtain a conical reduced-scale shell. The experimental results of this reduced-scale structure are compared to theoretical predictions for the equivalent cylindrical shell. No agreement is found and it is concluded that the conical shell undergoes complex motions. No comparison is made to the full-scale structure. Next to this, NASA has performed several dynamic scale model tests throughout the years, for example, for the Space Shuttle [56] and the International Space Station [57, 58].

Dimensional analysis has been applied to steel conical shells subjected to impact loading [59]. The input and output parameters are given in Table 2.2. Three equivalent structures are developed, all with cone angle $\alpha = 30°$. The height, length, radius and thickness are all scaled by β, which equals 1, 2 and 4 for the three respective structures. Note that the conical shells are not truncated but end with a cylindrical head. The cylindrical projectiles are scaled accordingly. The conical shells are tested at different impact velocities. The impact velocities at which cracking occurs are compared. It is observed that the small structure resist perforation better than large structures. This is in agreement with literature on size effects [51], but not with the scaling laws dictating that the critical impact velocity should be the same for all sizes. The permanent axial deformation neither follows the scaling law, but are larger than predicted. These discrepancies are attributed to the influence of material strain rate sensitivity, fracture and plastic buckling. These three phenomena do not obey the scaling laws. If their effects are taken into account, the difference between experiment and

theory is smaller.

Table 2.2: Scaling parameters derived by Jiang et al. [59] using Buckingham's Π theorem.

Scale factor	Input parameters	Output parameters
1	Cone angle	Strains
	Impact velocity	Stresses
	Material densities (shell and projectile)	
	Yield stresses (shell and projectile)	
β	Projectile diameter	Impact time
	Conical shell height	Permanent axial displacement
β^2		Impact force
β^3	Projectile mass	
$1/\beta$		Strain rate

2.3.3 Similitude Theory Applied to the Dimensional Governing Equations

A second method to design scaled systems is by applying the similitude theory to the dimensional governing equations. This method relies on the fact that the behavior of the full-scale and reduced-scale systems are described by the same set of equations. The variables of the two systems can be related through a scale factor. By substitution of this relation (i.e. $x_{\mathrm{FS},i} = \lambda_i x_{\mathrm{RS},i}$) into the equation of the full-scale system and imposing that the result should be the equation of the reduced-scale system, one obtains the scaling laws. The adopted equations can be the differential equations or the solution equation. As a result, the methodology can be traced back to the theory, which is convenient to assess its applicability. The derivation of the scaling laws and the application to a specific structure is time consuming. Clearly worked-out examples of the scaling technique are given by Simitses et al. [51] and Casaburo et al. [14]. This method has been mainly used for vibration problems, of which Zhu et al. [60] provide an overview. It has also been extensively applied to laminated structures [50, 51, 61–63]. Here, some of these applications are highlighted.

Buckling of Laminated Cylindrical Shells In 1993, Rezaeepazhand and Simitses investigated the buckling and free vibration behavior of symmetric laminated angle-ply plates [61]. Three years later, they applied this approach to symmetric, cross-ply laminated cylindrical shells in axial compression [62]. They assume that the material behaves linearly elastic, such that there is no size effect. It is also assumed that all shells are free from imperfections, or that imperfections affect the shells in the same way. The authors used the Donnell-type kinematic relations to establish the buckling equations of the simply supported cylindrical shell.

To obtain complete similarity between full- and reduced-scale shells, several scaling laws must be followed. First, ply-level scaling should be fulfilled. This means that the material properties and stacking sequence are identical, but with a different number of plies, namely $[+\theta, -\theta]_s$ and $[+\theta_n, -\theta_n]_s$. Here, θ is the ply angle, subscript n the number of plies and subscript S indicates symmetry. The different stacking sequences are visualized in Figure 2.6. Second, there must be geometric similitude, meaning the radius, length and thickness are scaled by the same factor. Consequently, the curvature parameter $Z = \frac{L^2}{Rt}$ is the same for both structures.

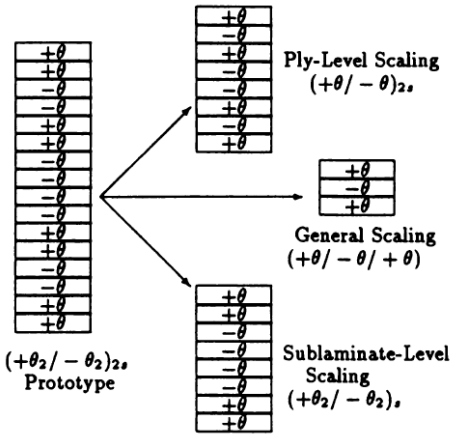

Figure 2.6: The three possibilities for distortion in stacking sequence [63].

These scaling laws are rather restricting and give limited design freedom. The use of partially similar models is also investigated by the authors. They allowed distortion in one of the parameters at a time, while keeping the other scaling laws fulfilled. The distorted parameters are the number of plies, stacking sequence, length, cylinder radius, total thickness, and material properties. Accurate predictions of the full-scale shell by the reduced-scale shell are obtained for distortion of the first three parameters, but not for distortion of the last three parameters.

For the disturbance in the stacking sequence, the opposite layup was considered for the reduced-scale shell, which corresponds to general ply scaling in Figure 2.6. The prediction accuracy increases as the number of plies of the reduced-scale shell increases. which is shown in Figure 2.7. The triangles show the behavior of the reduced-scale shell, the dots show the behavior of the full-scale shell and the circles show the prediction of the behavior of the full-scale shell by the reduced-scale shell. Although a disturbance in length does not affect the prediction accuracy, the curvature parameter Z is also affected by this change. It is known that the imperfection sensitivity is affected by the curvature parameter, which is not investigated in this research. Furthermore, for large distortions in length, the reduced-scale structure has a different mode shape than the full-scale structure. The poor prediction accuracy for a disturbance in radius is shown in Figure 2.8: the data points of the predicted buckling load (circles) and theoretical buckling load (dots) do not coincide.

Tabiei and Simitses [63] extended the work of Rezaeepazhand and Simitses to axially compressed cylindrical shells with initial imperfections. The introduced imperfections are a weighted sum of several linear buckling modes. The buckling equations and scaling laws are identical to the ones used by Rezaeepazhand and Simitses [62]. The results are obtained through a finite element analysis in Abaqus. For the case of complete similarity (ply-level scaling), the same imperfection sensitivity, quantified through the knockdown factor, is observed for varying number of plies. The end-shortening, however, is not scaled: the calculated shortening depends on the number of plies. A distortion in stacking sequence is applied using sublaminate scaling (see Figure 2.6). Almost the same imperfection sensitivity is observed for varying number of plies. The variation of end-shortening with the number of plies is not investigated for this case. Unfortunately, the effect of distortions in geometric parameters,

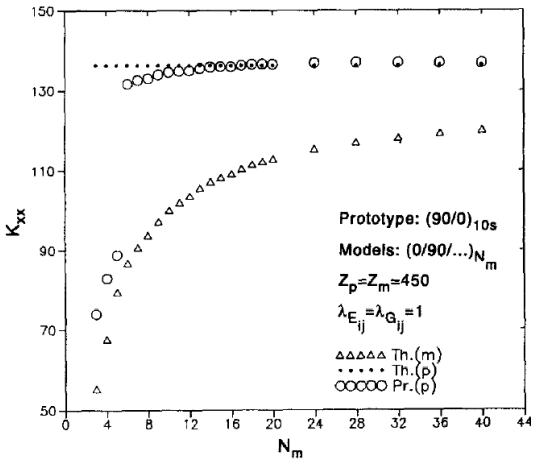

Figure 2.7: Prediction accuracy of the buckling load for a disturbance in stacking sequence and number of plies [62].

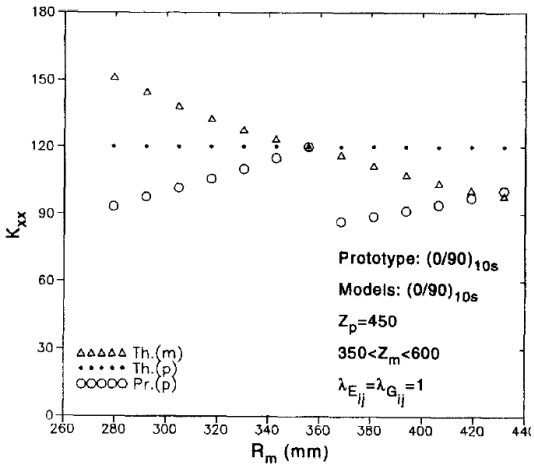

Figure 2.8: Prediction accuracy of the buckling load for a disturbance in radius [62].

which is known to affect the sensitivity to imperfections, is not studied in this paper.

Ungbhakorn and Wattanasakulpong [64] investigated the structural similitude for the buckling and vibration behavior of anti-symmetric cross-ply laminated cylindrical shells through similitude theory. Due to the anti-symmetry, the extension-bending coupling matrix $\boldsymbol{B}$ is non-zero, which is different from the case studied in the papers discussed above. The same equations and scaling laws are used, with the addition of the scaling laws related to the $\boldsymbol{B}$ matrix. In case complete similitude is obtained, the accuracy of the scaling law is high in terms of the buckling load and mode shapes. If the effect of the scaling parameter related to the $\boldsymbol{B}$ matrix is ignored, partial similarity is obtained, but the prediction accuracy is still high with a maximum discrepancy of 1% for the buckling load. The buckling mode shape is correctly predicted in four out of six cases. In contrast, if the $\boldsymbol{A}$ or $\boldsymbol{D}$ matrix effects are ignored, the accuracy reduces by 33% and the buckling mode is predicted correctly one out of twelve times. The influence of ignoring the $\boldsymbol{B}$ matrix effect is larger if the number of plies reduces. This is attributed to the stronger influence of the $\boldsymbol{B}$ matrix (i.e. of the asymmetry) if there are less plies. Distortions in material properties do not give accurate buckling predictions, in line with the findings of Rezaeepazhand and Simitses [62].

Modular Approach In 2018, Coutinho et al. [65] noticed that new scaling laws are derived each time depending on the assumptions of the specific application. This is time-consuming and a general approach, which makes a minimum of assumptions, would be more convenient. They therefore develop a modular approach with three levels for a generalized plate. The first level consists of six modules, each containing the scaling laws corresponding to a set of equations, which are kept as general as possible by making few assumptions. Examples of the equations in the modules are the strain-displacement relations and the equations of motion.

On the second level, the scaling laws of the six modules are combined. In case a multi-body structure is considered, the scaling laws for the interaction between the different bodies are derived on the third level. This is done by imposing continuity of internal forces and displacements at the interfaces. The authors successfully apply the approach to a stiffened

plate under uniform pressure and pinned along the edges. The scaling laws for the stiffeners are derived by simplifying the plate equations to beam equations and deriving the scaling laws from there. Three reduced-scale configurations are explored and they all yield excellent results when numerically compared in finite element software, as can be seen in Figure 2.9.

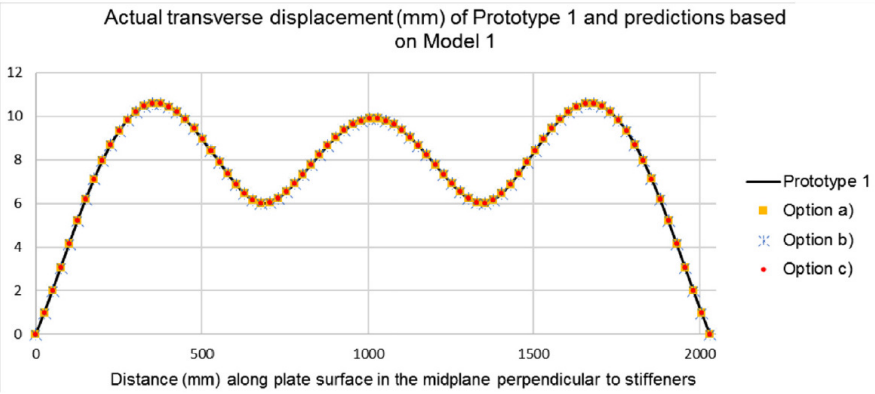

Figure 2.9: Comparison of the actual and predicted transverse displacement [65].

An extension of this approach to other structures, such as shells and solid bodies, would enable scaling of large and complex structures. Additionally, the inclusion of partial similitude, which was not considered yet, would make the method more versatile.

2.3.4 Similitude Theory Applied to the Nondimensional Governing Equations

The third scaling methodology makes use of nondimensional governing equations. As these equations are intrinsically independent of the size of the structure, shells of different size can be easily compared and the coefficients of the equations can be used as scaling parameters. These parameters should be equal for full-scale and reduced-scale systems to obtain similarity. Note that the parameters are not unique and that they depend on the way the equations are made nondimensional. Experience and insight by the designer aid in determining the most convenient nondimensionalization procedure. Compared to the method discussed in subsection 2.3.3, this method requires more effort to determine the scaling parameter, but the design of the reduced-scale systems is more straightforward. This method has not been applied a lot in the past, but is discussed here because of the promising recent developments. Four applications were found, which are all discussed here.

Solar Sail System In 2004, Canfield et al. [66] developed similarity rules for a solar sail system. They approximated the sail as a thin plate with transverse loading and the booms as beams. The governing equations as well as the boundary conditions of the plate and beams are made dimensionless, from which scaling parameters are obtained. The interaction between the sail and booms imposes additional scaling laws. The nondimensional scaling parameters are set equal for full-scale and reduced-scale structures such that scaling laws are obtained of similar type as the ones obtained for similarity through dimensional governing equations. The scaling laws are used for the design of square solar sails with a side length of 20, 30, and 40 meters, based on a design with a side length of 10 meters. The comparison is made through a numerical analysis to predict the out-of-plane deflection of the sail and the lateral deflection of the boom. The material is kept the same for all structures. The 10 meter system was able to predict the deflections for the three larger systems within 0.6%.

Free Vibration of a Stiffened Cylindrical Shell Torkamani et al. [67] investigated the free vibration of an isotropic, orthogonally stiffened cylindrical shell. The full-scale shell has Ω-shaped stiffeners and Z-shaped ribs. For the scaling analysis, the stiffeners are smeared out over the shell by averaging the effect of the stiffeners. From the governing equations, the nondimensional frequency is obtained in terms of nondimensional parameters representing the geometry, loading, stiffness ratios, etc. Through substitution of the full-scale variables in the frequency equation of the reduced-scale shell, scaling laws are derived. These are of similar type as the ones derived by Canfield et al. for the solar sail.

First, a replica model is evaluated. This reduced-scale shell is identical to the full-scale shell, but geometrically scaled down by a factor 3. A modal analysis is performed in finite element software and the first ten natural frequencies are compared. In the finite element model, the stiffeners are applied as discrete elements. The predictions by the reduced-scale structure are all within 1% of the frequencies obtained for the full-scale structure. As the production of small and thin Ω- or Z-shaped stiffeners can be difficult, the authors investigated the possibilities of introducing changes into the design. First, the effect of using equivalent T-shaped stiffeners is evaluated. The frequency is predicted within 3% if the cross-section properties are kept identical to the ones of the original reduced-scale stiffeners. The material of the T-stiffeners can be changed without loss in accuracy such that larger stiffener cross-sectional areas are possible.

Finally, it is investigated if the number of stiffeners can be reduced to increase the cross-sectional area of the stiffeners. This results in an error of larger than 10% for two of the compared modes. This error is attributed to the number of stringers being exactly twice the number of circumferential half-waves in the reduced-scale shell. As a result, there is a frequency difference between the symmetric and anti-symmetric mode shapes, causing a change in natural frequency. Furthermore, it is important to note that the assumption of smearing does not hold anymore if the number of stiffeners is low, thus limiting the applicability of the latter approach.

An experimental comparison is made between a full-scale aluminum alloy shell with Ω-shaped stiffeners and Z-shaped ribs and a reduced-scale steel alloy shell with T-shaped ribs and stiffeners, which is geometrically scaled by a factor 3. The first six frequencies of the full-scale shell are evaluated and predicted within 7% by the reduced-scale shell. Torkamani et al. show with this research that the design freedom obtained due to the number of scaling laws being smaller than the number of variables, can be used smartly. For example, the manufacturing process can become easier and faster, thus reducing cost while increasing accuracy.

Blended Wing Body Aircraft Section Under Internal Pressure and Compression Loading Hilburger et al. [68] investigated sub-scale structural designs of a section of a blended wing body aircraft subjected to internal pressure and a spanwise compressive load. The structure under consideration consists of a cuboid, representing the center body, and a semicylinder, representing the leading edge structure. The full-scale structure is made of a sandwich structure with a honeycomb core and quasi-isotropic carbon fiber facesheets. The equations and scaling laws are derived from first order shear deformation plate theory, which is applied to each component of the structure.

The nondimensionalization procedure developed by Stein [69] and Nemeth [70] is used here. The idea of this procedure is to make the variables of the problem dimensionless, to minimize

the number of independent parameters describing the behavior, and to avoid inserting a direction of preference into the equations. The equations are made dimensionless by introducing nondimensional coordinates and parameters. As this is a multi-body structure, continuity at the interface must be ensured, which introduces additional equations and thus scaling parameters into the analysis. An example of a nondimensional parameter is the nondimensional out-of-plane displacement W,

$$W = \left(\frac{A_{11}A_{22} - A_{12}^2}{\sqrt{A_{11}A_{22}D_{11}D_{22}}} \right)^{1/2} w \,, \tag{2.4}$$

which is a stiffness-weighted function of the dimensional displacement w, depending on the extensional stiffness values A_{ij} and the flexural stiffness values D_{ij}. This nondimensionalization procedure is more complex and more computationally expensive than the one adopted by Canfield et al. [66] and Torkamani et al. [67]. On the other hand, it allows to decouple the structural properties, such that convenient scaling parameters are directly obtained from the equations.

Two reduced-scale structures are developed: one completely similar and one partially similar. The completely similar structure is geometrically scaled down to 1/12 of the full-scale structure and also has a sandwich configuration. The partially similar structure is also geometrically scaled to 1/12 and has a monolithic configuration. It has distortions in four out of ten parameters. The normal stress Q and displacement of the cover panel δ_1 and the aft spar δ_2 are compared in Figure 2.10. These results are obtained through a nonlinear finite element analysis. The full-scale response is indicated by superscript *fs*, the sandwich reduced-scale design prediction by superscript s and the monolithic reduced-scale design prediction by superscript m. The normal stress prediction is accurate for both reduced-scale designs. The sandwich structure also predicts the displacements exactly, as expected due to the complete similarity. The monolithic structure underestimates both displacements. Analyzing the distorted parameters, it is observed that they are related to the transverse shear properties, which are much larger for the monolithic structure. This indicates a higher stiffness, which propagates as a lower displacement prediction for the full-scale shell. If the monolithic design is adjusted such that complete similarity is obtained, the results are improved.

These results indicate that the accuracy of partially similar designs greatly depends on the parameter that is distorted. A sensitivity analysis can point out which scaling laws can be relaxed without loosing too much accuracy for a certain output. It is noted that the sensitivity not only depends on the scaling parameter, but also on the evaluated variable as well as the load case. Furthermore, even if complete similarity is obtained according to the scaling parameters, discrepancies can arise due to simplifications in the applied governing equations. The equations might not account for certain phenomena, which can become significant for the reduced-scale structure. It is therefore important to be aware of the assumptions made in the derivation of the equations.

Axial Buckling of a Sandwich Cylindrical Shell Finally, Uriol Balbin et al. [47] studied the scalability of cylindrical shells buckling in axial compression. The structure under consideration is a sandwich cylindrical shell with a honeycomb core and carbon fiber face sheets. This shell is a simplified subscale structure of a launch vehicle that has been tested by NASA [34]. The nondimensional buckling equations of the Donnell-Mushtari-Vlasov theory are used. The

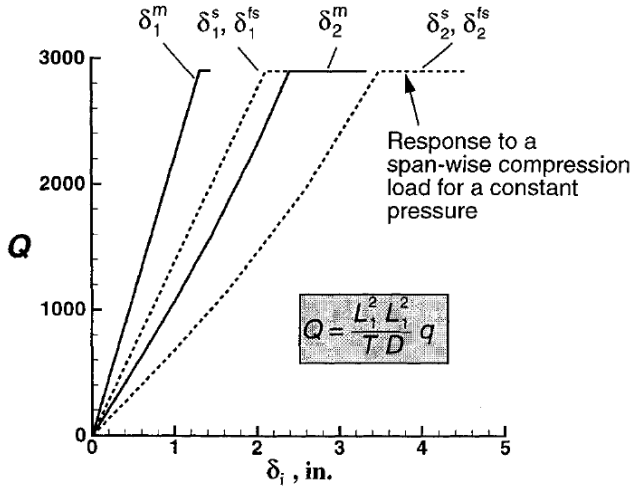

Figure 2.10: The theoretical and predicted response of the cover panel and aft spar of the blended wing body [68].

derivation of these equations for a general shell are derived by Nemeth [70]. The equations are made specific for a cylindrical shell in axial compression by Schultz and Nemeth [71]. It is assumed that the initial imperfections, bending-twisting anisotropy, and transverse shear deformation can be neglected. The derived scaling parameters have a similar structure as the ones for the blended wing body. As the governing equations are different for a shell than for a plate, the combination of variables most convenient for the nondimensionalization is different. For example, the nondimensional out-of-plane displacement is given by

$$W = \frac{w}{\sqrt[4]{a_{11}a_{22}D_{11}D_{22}}}\,. \tag{2.5}$$

Here w is the dimensional out-of-plane displacement, a_{ij} are the extensional compliances and D_{ij} are the flexural stiffnesses. Remarkable to note is that the scaling parameters are decoupled, such that reduced-scale configurations can be found in a sequential, rather than iterative, process.

Two full-scale designs are considered with the same dimensions but different stacking sequence. For both designs, reduced-scale structures are created with two different stacking sequences: $[\theta/-\theta]_s$ and $[\theta/0/-\theta]$. Four reduced-scale shells are designed for each full-scale shell. There are fewer scaling parameters than design parameters, so there is some design freedom: the radius is set to a convenient size for testing. The assumptions regarding the negligible flexural anisotropy and transverse shear are verified for all shells. The $[\theta/0/-\theta]$ reduced-scale shells are excluded from the analysis because the former assumption does not hold. For two out of the four remaining reduced-scale designs, the latter assumption is not valid, such that they are also excluded from the analysis. As a result, for each full-scale design, only one reduced-scale design remains.

The two full-scale shells and their respective reduced-scale shells are consequently modeled in finite element software Abaqus. A linear buckling analysis shows that the first full-scale shell and its reduced-scale version have the same axisymmetric buckling mode. The buckling mode of the second full-scale shell and its reduced-scale version are slightly different: the

full-scale shell has a checkerboard pattern, but the reduced-scale shell has a skewed checkerboard pattern. Next, the nonlinear nondimensional load-displacement curve is obtained from an implicit dynamic analysis. This is shown in Figure 2.11. There is excellent agreement between the full-scale and reduced-scale shells for displacement, load and stiffness. The largest discrepancy of 3.88% is observed for the buckling load prediction of the second full-scale shell. Finally, a preliminary failure check is performed. Facesheet failure and shear crimping are evaluated and are not expected to occur prior to buckling.

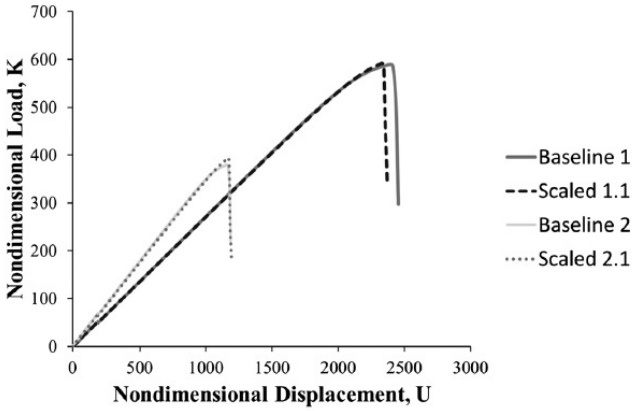

Figure 2.11: The nondimensional load-displacement responses for the full-scale shells (baselines) and their reduced-scale equivalents (scaled) [47].

This application shows the complexity of the scaling process: not only the scaling parameters should match, but the assumptions made for the governing equations should hold for both structures. Furthermore, additional considerations such as minimum core thickness for manufacturing, the possibility of failure and the influence of the vicinity of the boundary conditions on the buckling behavior are to be taken into account. Next to this, the sequential determination of the reduced-scale design variables is promising, because it avoids time-consuming iteration. Furthermore, once the reduced-scale shells are designed, they can easily be compared to their full-scale equivalent because they have exactly the same equations.

2.3.5 Other Methods

Next to the methods discussed above, there are some less conventional methods available for scaling. They are discussed in this section.

Since the early 2000, the energy methods have been studied. This comprises a method based on the principle of conservation of energy and a method called the asymptotical scaled modal analysis (ASMA). The former considers systems as a whole and applies similitude theory to the energy conservation equation. This method has been applied to vibration problems of shallow shells with various stacking sequences by Ungbhakorn and Singhatanadgid [72]. The same scaling laws are obtained as in [64], discussed above. The method has also been successfully applied to stiffened cylindrical shells by Yu and Li [73]. This method is convenient for multi-body structures, because the systems are considered as a whole. On the other hand, it requires a lot calculation effort, especially for complex systems. The latter method, ASMA, is a method for a faster vibration analysis for large structures, especially for high frequencies. A

generalization of ASMA has been developed by De Rosa et al. [74] and is called the similitude and asymptotic models for structural-acoustic research applications (SAMSARA) [14].

Next to this, there are empirical similarity methods for rapid prototyping. The methods consist of testing two specimens: one with simple geometric features produced using rapid prototyping and another simple specimen produced with the actual production process. Their state vectors are measured to obtain a state transformation. This transformation matrix can then be used to relate more complex structures produced by the two methods to each other. As a result, mock-ups of complex structures can be made using alternative, faster production processes. The advantage of this method is that the transformation matrix is empirical, and thus already takes into account manufacturing flaws. The disadvantage is that production and testing are needed for establishing the similarity rules. [65, 75]

Other methods exist, such as the energy distribution approach and the statistical energy analysis, but are not discussed here for sake of brevity and because they are more focused on highly dynamic responses, such as vibrations. Furthermore, methods can be combined with each other or with sensitivity analyses, as was done by Hilburger et al. [68]. More information on these methods can be found in [14, 65].

2.3.6 Scaling of Conical Shells

Two applications of dimensional analysis to conical shells were found, as already discussed in subsection 2.3.2. The other methods discussed above are not found to be applied to conical shells. Additionally, in several review papers [14, 15, 51, 60], conical shells are not mentioned. Although similitude through governing equations seems to not have been applied to conical shells, scaling of conical shells has been done in the past. This section gives an overview of the cases found in literature.

Sleight et al. [20] studied the imperfection sensitivity of conical sandwich composite shells in axial buckling. Two structures are considered, representing two NASA launch vehicle components: the Space Launch System Universal Stage Adapter (SLS USA) and the Space Launch System Payload Attach Fitting (SLS PAF). The former has a small cone angle, the latter a large one. Several combinations of facesheet layups and core thicknesses are combined and for each design, a half-height configuration is developed. The half-height design can be understood as the bottom half conical shell of the full-height design. The materials, stacking sequence, core thickness, bottom radius, and cone angle are the same as the full-scale structure design.

The full-scale and reduced-scale designs are numerically tested in Abaqus. Measured imperfections (scaled from a cylindrical shell) are applied with an amplitude varying from 0x to 10x the measured values. Comparing the results of the half-height configurations to the full-height ones, it is concluded that the buckling loads are almost identical. Furthermore, knockdown factors are calculated by dividing the nonlinear result with imperfections of all magnitudes by the linear result without imperfections. They are also more or less identical for reduced-scale and full-scale structures. The half-height structure sometimes has a higher knockdown factor than the full-height structure, which would result in an unconservative design if its result is used for full-scale design. The buckling mode of the two structures are not identical for full-height and half-height shells. The radial displacements upon buckling are in the same order of magnitude.

This scaling method yields very good results compared to the computational effort it requires. From a testing perspective, this method may not be a useful solution, as there is no circumferential size reduction. However, the production time and cost would be reduced, because the same mold could be used for both structures. Next to this, there is no scientific rationale behind the method given and the buckling mode is not accurately predicted.

Yilmaz et al. [76] developed a similarity approach for the buckling of ring-stiffened isotropic conical shells with high cone angle. They introduced two nondimensional parameters, the equivalent radius-to-thickness ratio and a rigidity parameter of the stiffening ring. The authors develop three conical shells with identical nondimensional parameters. They do this for three different cone angles. They consequently nonlinearly model the shells in finite element software. The obtained buckling load is divided by the buckling load obtained from Seide's formula (Equation 2.1) to find a knockdown factor. It is observed that the knockdown factor is more or less constant for shells with the same cone angle and nondimensional parameters. The authors successfully applied their approach to conical shells with cone angle 70°, 75° and 80°. Only the knockdown factor is compared, not the buckling shape.

2.4 Conclusions, Research Aim and Objective

Conical shells are commonly used in engineering applications, such as launch vehicles. A sizing load case for these structures is axial compression, because it can lead to loss of stability and consequently loss of load carrying capability. Therefore, it is important to understand the buckling behavior of composite conical shells in axial compression. The behavior is, however, described by a complex mathematical problem, which does not allow for a straightforward, accurate analytical solution. Additionally, large discrepancies between test and theory are observed. These are attributed to imperfections, categorized into geometric, stiffness and loading and boundary condition imperfections. To account for the discrepancy during the design, the NASA SP-8019 guidelines have been developed for isotropic shells, which are found to be overly conservative in many cases and are not applicable to composite conical shells. Other approaches have been discussed as well, namely the deterministic and stochastic approaches. Although these approaches give insight in the buckling behavior, they do not always effectively balance the level of conservatism.

To bridge the gap between the design table and reality, experimental testing is still an inevitable part of conical shell development. This is, however, expensive and difficult for large structures and consequently not frequently done. A solution to the size problem is to test representative smaller-scale structures. The design of these reduced-scale structures is done through scaling methodologies, which are based on similitude science. It has mainly been applied to highly dynamic systems and vibration problems. Various methods for scaling are discussed.

The dimensional analysis method is applied less and less to aerospace applications, as preference is given to methods which can be traced back to equations [15]. In-depth understanding of the problem is key to determine convenient scaling parameters. Similitude theory applied to dimensional governing equations has been applied to stability problems, mainly for plates and cylindrical shells. Satisfactory results are obtained for both completely and partially similar configurations. The scalability of the imperfection sensitivity has not been researched extensively yet. A disadvantage of this method is that the reduced-scale system design and

the comparison of results are time-consuming. The most promising method makes use of the nondimensional equations. It has been used much less, probably because the nondimensional equations are less known and complex to achieve. On the other hand, once the equations are derived, the design of the reduced-scale systems and the comparison between the different systems is straightforward.

The scaling of more complex structures, such as multi-body structures, conical shells, and spherical shells, is not done much. For conical shells, the scaling applications found in literature do not rely on an extensive scientific basis. As a result, the methodology scales only part of the phenomenon and the accuracy and the number of scaled parameters remain limited. In addition, if laminate full-scale structures are scaled, the stacking sequences are often not realistic, thus limiting the practical use of the methodology. Finally, the scalability of the imperfection sensitivity should be examined in more detail. Especially for shell structures, the influence of imperfections on real structure behavior cannot be neglected.

This thesis aims to develop a scaling methodology for the stability behavior of composite conical shells in axial compression. The nondimensional governing equations will be used, because it allows to directly derive the scaling laws from the equations and to compare the response of the shells in a straightforward way. The applicability and prediction accuracy of the methodology are evaluated through finite element models. Additionally, the effects of assumptions and geometric imperfections on the prediction accuracy are assessed. The objective of this research, therefore, is

> To develop an analytical scaling methodology for the buckling behavior of composite conical shells in axial compression by means of nondimensionalization of the governing equations and a finite element model comparison as verification.

The following research questions are answered to reach this objective:

- What are the nondimensional scaling parameters making up the scaling methodology?
- How well do the reduced-scale models predict the buckling behavior of the full-scale model in terms of buckling load and mode shape?
- How do the assumptions in the governing equations limit the reduced-scale model design and their prediction accuracy?
- How do geometric imperfections affect the accuracy of the scaling methodology?

Chapter 3

Analytical Derivation of Governing Equations and Scaling Methodology

The scaling methodology will make use of the nondimensional form of the equations governing the stability behavior of composite conical shells in axial compression. Therefore, these equations should be derived before the scaling methodology can be developed. This chapter covers this part of the research, as well as a discussion of the employed semi-analytical solution. The approach for the derivation is visualized in Figure 3.1. As a first step, the geometry and sign conventions are detailed. This consists of, on one hand, sketching a broader framework by outlining the concepts of general shell theory and, on the other hand, specifying the conventions for the conical shell. This allows to define the kinematic and constitutive equations. Next, the dimensional governing equations are derived and written in a stress function formulation. These are consequently used for two purposes: the development of a semi-analytical solution and the nondimensionalization for which the approach established by Nemeth for a general shell is used [77]. This is followed by a discussion of the step-by-step procedures of the scaling methodology.

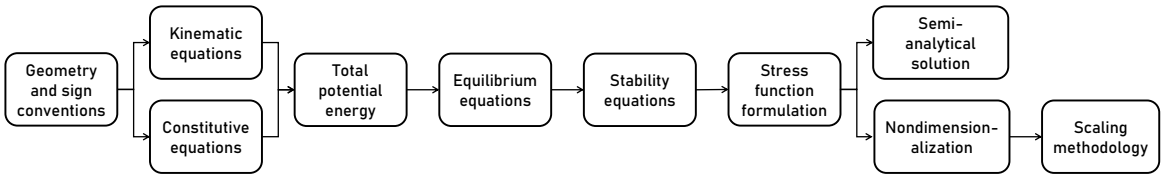

Figure 3.1: Flow chart for the derivation of the scaling methodology and the semi-analytical solution.

3.1 General Shell Theory

First, concepts from general shell theory are outlined in order to understand the equations which are later used for the conical shell. A shell is defined as a body bounded by two surfaces, between which the distance (i.e. the thickness) is much smaller than the in-plane dimensions

of the surfaces [7]. A shell can be distinguished from a plate through its curvature, which gives the shell its efficient load carrying capability. The behavior of a general shell is typically described in a curvilinear (x, y, z) coordinate system, where x and y run parallel to the principle lines of curvature. The z-direction is oriented such that a right-handed coordinate system is created. The radii of curvature are given by R_x and R_y for the respective in-plane axes, as can be seen in Figure 3.2. The in-plane dimensions are given by L_1 and L_2, the thickness by t.

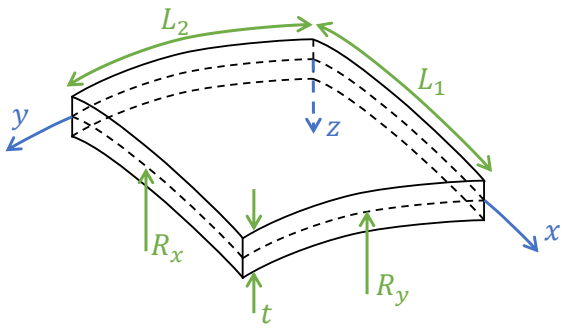

Figure 3.2: General shell geometry and curvilinear coordinate system.

In the nineteenth century, Love [78] presented an approximation shell theory based on linear elasticity. Use was made of the Kirchhoff hypothesis for plate bending theory, as well as some assumptions specific for shells [7]. More specifically, it is assumed that

- lines normal to the mid-surface of the shell remain straight and normal to the mid-surface and do not extend during deformation,
- the through-thickness normal stress σ_{zz} is negligible with respect to the other stress components,
- the shell is thin, and
- displacements are small compared to the thickness.

The first two assumptions are part of Kirchhoff's hypothesis, the latter two were added by Love for the shell theory. The first assumption allows to neglect the through-thickness strains and suggests a state of plane strain. The combination with the second assumption, however, suggests a state of plane stress. These two states can only coexist if the Poisson's ratio is zero, which is usually not the case. This contradiction is known to be present, but it does not affect the accuracy of the theory to a critical extent. For the thinness criterion, a lower limit of $\frac{L_i}{t} = 20\,(i = 1, 2)$ is typically adopted. Because of the last assumption, the nonlinear terms in the strain-displacement relations vanish in comparison with the linear terms. [7]

Based on these assumptions, a general linear theory for thin shells can be derived. This theory is still rather complex and does not account for the large displacements observed during buckling. Donnell [79], Mushtari [80] and Vlasov [81] made additional simplifications and accounted for these larger displacements. It is assumed that

- the shell is in a plane stress state, which requires that the transverse shear forces Q_x and Q_y have a negligible influence on the in-plane equilibrium, and
- the out-of-plane displacement w dominates the bending response, in comparison to the in-plane displacements u and v.

The second assumption here contradicts the last assumption made for the Kirchhoff-Love hypothesis. This is needed to cover the buckling phenomenon. To account for this, the nonlinear expressions are added back to the strain-displacement relations. In addition, this assumption puts constraints on the type of shell to which the theory can be applied. More specifically, the shell should be shallow or, if it is a closed shell, its displacement components should be rapidly varying functions of the coordinates in the deformed state [7, 8]. The conical shell analyzed here falls in the second category. Schultz and Nemeth translated this requirement to the requirement that the deformation should have "more than approximately three circumferential waves" [71].

3.2 Conical Shell Structure

The conical shell under consideration is shown in Figure 3.3. The coordinate system consists of the curvilinear (x, y, z) coordinates, in line with the general shell coordinate system in Figure 3.2. As a result of the curvilinear system, a differential arc length $\mathrm{d}S$ between two neighboring points on the shell surface can be described as

$$(\mathrm{d}S)^2 = (A_x \mathrm{d}x)^2 + (A_y \mathrm{d}y)^2 = (\mathrm{d}x)^2 + (\mathrm{d}y)^2 \ . \tag{3.1}$$

In the equation above, A_x and A_y are the coefficients of the first fundamental form of the surface, which both equal 1, $A_x = A_y = 1$, for this set of coordinates [77].

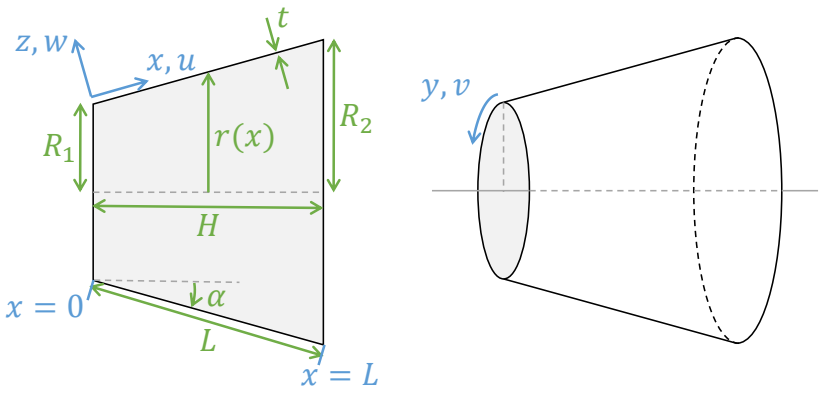

Figure 3.3: Geometry and sign convention for the coordinate system and displacements.

The meridional coordinate x ranges from $x = 0$ at the small radius end to $x = L$ at the large radius end. The corresponding displacement is called u. The circumferential coordinate y ranges from $y = 0$ to $y = 2\pi r(x)$, where $r(x)$ is the varying radius. The corresponding displacement is called v. Usually, an angle coordinate θ is used instead of y, such that $y = r(x)\,\theta$. This is not done here, because the nondimensionalization requires all coordinates

to be expressed in units of length. The through-thickness outward normal coordinate z ranges from $z = -t/2$ to $z = t/2$, where t is the thickness, which is identical to the thickness definition of the general shell in Figure 3.2. As a result, $z = 0$ at the mid-surface of the shell. The corresponding displacement is called w. The thickness is assumed to be constant.

As shown in Figure 3.3, the slant length is given by L, which corresponds to dimension L_1 in the general shell convention given in Figure 3.2. The height is given by H and the cone angle by α. The radius of the conical shell varies from R_1 at the small end to R_2 at the large end. The varying radius $r(x)$ corresponds to dimension L_2 in the general shell convention of Figure 3.2. The variation of the radius with the meridional coordinate is given by

$$r(x) = R_1 + x \sin \alpha \,. \tag{3.2}$$

The conical shell conventions in Figure 3.3 have been linked to the general shell conventions in Figure 3.2 in terms of dimensions and coordinate system. In addition, the radius of curvature in x-direction is given by $R_x \to \infty$ and the radius of curvature in y-direction $R_y = \frac{r(x)}{\cos \alpha}$. This can be understood as the radius normal to the shell's surface.

3.3 Derivation of the Dimensional Governing Equations

This section covers the derivation of the stability equations for a conical shell in axial compression. First, the kinematic relations are explained, after which the constitutive equations are discussed. Then, the equilibrium equations are derived, from which consequently the stability equations are found. For the derivation, use is made of the derivation by Nemeth [77], in which the equations for a general shell are derived. The particularization for the conical shell is verified with references [25, 82].

3.3.1 Kinematic Equations

The kinematic equations define the relations between the strain and displacement components. In accordance with the Kirchhoff-Love hypothesis, the kinematic relations for the thin shell are given by

$$\{\boldsymbol{\epsilon}(x, y, z)\} = \{\overline{\boldsymbol{\epsilon}}(x, y)\} + z \{\boldsymbol{\kappa}(x, y)\} \,, \tag{3.3}$$

where

- $\{\boldsymbol{\epsilon}(x, y, z)\}$ is the strain vector, $\{\boldsymbol{\epsilon}(x, y, z)\} = \{\epsilon_{xx}, \epsilon_{yy}, \gamma_{xy}\}^T$,
- $\{\overline{\boldsymbol{\epsilon}}(x, y)\}$ is the membrane strain at the mid-surface (i.e. the reference surface at $z = 0$),
- $\{\boldsymbol{\kappa}(x, y)\}$ is the change of curvature of the mid-surface.

It is assumed that the conical shells are free from imperfections. The nonlinear mid-surface strains and change of curvature according to the Donnell-Mushtari-Vlasov general shell theory [77] in the adopted coordinate system are consequently given by

$$\{\overline{\boldsymbol{\epsilon}}\} = \begin{Bmatrix} \overline{\epsilon}_{xx} \\ \overline{\epsilon}_{yy} \\ \overline{\gamma}_{xy} \end{Bmatrix} = \begin{Bmatrix} u_{,x} + \frac{w}{R_x} + \frac{1}{2} w_{,x}^2 \\ v_{,y} + \frac{w}{R_y} + \frac{1}{2} w_{,y}^2 \\ u_{,y} + v_{,x} + w_{,x}\, w_{,y} \end{Bmatrix} \tag{3.4}$$

and

$$\{\boldsymbol{\kappa}\} = \begin{Bmatrix} \kappa_{xx} \\ \kappa_{yy} \\ \kappa_{xy} \end{Bmatrix} = \begin{Bmatrix} -w_{,xx} \\ -w_{,yy} \\ -2\,w_{,xy} \end{Bmatrix}. \tag{3.5}$$

Substituting the radii of curvature of the conical shell, yields

$$\{\overline{\boldsymbol{\epsilon}}\} = \begin{Bmatrix} \overline{\epsilon}_{xx} \\ \overline{\epsilon}_{yy} \\ \overline{\gamma}_{xy} \end{Bmatrix} = \begin{Bmatrix} u_{,x} + \frac{1}{2}w_{,x}^2 \\ v_{,y} + \frac{\cos\alpha}{r(x)}w + \frac{1}{2}w_{,y}^2 \\ u_{,y} + v_{,x} + w_{,x}\,w_{,y} \end{Bmatrix} \tag{3.6}$$

and

$$\{\boldsymbol{\kappa}\} = \begin{Bmatrix} \kappa_{xx} \\ \kappa_{yy} \\ \kappa_{xy} \end{Bmatrix} = \begin{Bmatrix} -w_{,xx} \\ -w_{,yy} \\ -2\,w_{,xy} \end{Bmatrix}. \tag{3.7}$$

In the equations above, and in the following, the subscripts $(\,)_{,x}$ and $(\,)_{,y}$ denote the derivatives with respect to the axial and circumferential coordinates.

3.3.2 Constitutive Equations

The conical shell is assumed to be made of a composite material and it is assumed that each ply can be approximated as an orthotropic layer. In addition, it is assumed that failure and damage do not occur and that the material behaves linearly elastic. Classical laminate theory is applied. For an orthotropic ply under plane stress conditions, the stress in the ply $\{\boldsymbol{\sigma}_{\text{ply}}\} = \{\sigma_{11}, \sigma_{22}, \tau_{12}\}^T$ and strain in the ply $\{\boldsymbol{\epsilon}_{\text{ply}}\} = \{\epsilon_{11}, \epsilon_{22}, \epsilon_{12}\}^T$ are related through

$$\{\boldsymbol{\sigma}_{\text{ply}}\} = [\boldsymbol{Q}_{\text{ply}}]\,\{\boldsymbol{\epsilon}_{\text{ply}}\} \tag{3.8}$$

where $[\boldsymbol{Q}_{\text{ply}}]$ is the stiffness matrix. It is given by

$$[\boldsymbol{Q}_{\text{ply}}] = \begin{bmatrix} \frac{E_{11}}{1-\nu_{12}\nu_{21}} & \frac{\nu_{12}E_{22}}{1-\nu_{12}\nu_{21}} & 0 \\ \frac{\nu_{12}E_{22}}{1-\nu_{12}\nu_{21}} & \frac{E_{22}}{1-\nu_{12}\nu_{21}} & 0 \\ 0 & 0 & G_{12} \end{bmatrix} \tag{3.9}$$

where E_{11} is the longitudinal modulus (in the fiber direction), E_{22} is the transverse modulus (perpendicular to the fiber direction) and G_{12} is the in-plane shear modulus. ν_{12} and ν_{21} are the major and minor Poisson's ratio, respectively. [83]

To obtain the ply properties in the general (x, y, z) coordinate system, a transformation must be carried out. The transformation matrix $[\boldsymbol{T}]$ is defined as

$$[\boldsymbol{T}] = \begin{bmatrix} \cos^2\theta & \sin^2\theta & 2\sin\theta\cos\theta \\ \sin^2\theta & \cos^2\theta & -2\sin\theta\cos\theta \\ -\sin\theta\cos\theta & \sin\theta\cos\theta & \cos^2\theta - \sin^2\theta \end{bmatrix} \tag{3.10}$$

where θ is the ply angle which is measured positively from the x-axis to the y-axis. As a result, the stress, strain, and stiffness in the general coordinate system can be obtained using

$$\{\boldsymbol{\sigma}\} = [\boldsymbol{T}]\{\boldsymbol{\sigma}_{\text{ply}}\}\,, \tag{3.11a}$$

$$\{\boldsymbol{\epsilon}\} = [\boldsymbol{T}]^{-T}\{\boldsymbol{\epsilon}_{\text{ply}}\}\,, \tag{3.11b}$$

$$[\boldsymbol{Q}] = [\boldsymbol{T}]^{-1}[\boldsymbol{Q}_{\text{ply}}][\boldsymbol{T}]^{-T}\,. \tag{3.11c}$$

It is more convenient to work with the forces and moments per unit width than with stresses. Therefore, their relation given by

$$\begin{Bmatrix}\{\boldsymbol{N}\}\\ \{\boldsymbol{M}\}\end{Bmatrix} = \int_{-t/2}^{t/2}\{\boldsymbol{\sigma}\}\begin{Bmatrix}\{\boldsymbol{1}\}\\ \{\boldsymbol{z}\}\end{Bmatrix}\mathrm{d}z \tag{3.12}$$

is used to express the forces and moments per unit width as a function of the strain. In the equation above $\{\boldsymbol{N}\} = \{N_{xx}, N_{yy}, N_{xy}\}^T$ represents the membrane forces per unit length and the bending moments per unit length are given by $\{\boldsymbol{M}\} = \{M_{xx}, M_{yy}, M_{xy}\}^T$.

By substitution of the stress-strain relationships into Equation 3.12, and rewriting the continuous integral as a discrete sum across the plies, one obtains

$$\begin{Bmatrix}N_{xx}\\ N_{yy}\\ N_{xy}\\ M_{xx}\\ M_{yy}\\ M_{xy}\end{Bmatrix} = \begin{bmatrix}A_{11} & A_{12} & A_{16} & B_{11} & B_{12} & B_{16}\\ A_{12} & A_{22} & A_{26} & B_{12} & B_{22} & B_{26}\\ A_{16} & A_{26} & A_{66} & B_{16} & B_{26} & B_{66}\\ B_{11} & B_{12} & B_{16} & D_{11} & D_{12} & D_{16}\\ B_{12} & B_{22} & B_{26} & D_{12} & D_{22} & D_{26}\\ B_{16} & B_{26} & B_{66} & D_{16} & D_{26} & D_{66}\end{bmatrix}\begin{Bmatrix}\overline{\epsilon}_{xx}\\ \overline{\epsilon}_{yy}\\ \overline{\gamma}_{xy}\\ \kappa_{xx}\\ \kappa_{yy}\\ \kappa_{xy}\end{Bmatrix} \tag{3.13}$$

where

$$A_{ij} = \sum_{k=1}^{n} Q_{ij}^{(k)}\cdot(z_k - z_{k-1})\,, \tag{3.14}$$

$$B_{ij} = \frac{1}{2}\sum_{k=1}^{n} Q_{ij}^{(k)}\cdot(z_k^2 - z_{k-1}^2)\,, \tag{3.15}$$

$$D_{ij} = \frac{1}{3}\sum_{k=1}^{n} Q_{ij}^{(k)}\cdot(z_k^3 - z_{k-1}^3)\,, \tag{3.16}$$

and where $Q_{ij}^{(k)}$ is the (i,j) element of the stiffness matrix $[\boldsymbol{Q}]$ of the kth ply of the laminate. z_k and z_{k-1} are the through-thickness top and bottom location of the kth ply.

The equation above can be simplified by making assumptions on the nature of the laminate. It is assumed that the layup is symmetric, such that $\boldsymbol{B} = \boldsymbol{0}$, and that the layup is balanced, such that $A_{16} = A_{26} = 0$. The latter means that for every $+\theta$ ply, there is a $-\theta$ ply. Next to this, it is assumed that the bending-twisting coupling is negligible, such that $D_{16} = D_{26} = 0$. It is not possible to achieve zero D_{16} and D_{26} entries with a symmetric layup, unless a cross-ply layup is used, but it is aimed to minimize these two flexural anisotropy parameters. This

is achieved by placing θ and $-\theta$ plies close to each other [83]. As a result, the equations simplify to the equations for an orthotropic laminate, given by

$$\begin{Bmatrix} N_{xx} \\ N_{yy} \\ N_{xy} \\ M_{xx} \\ M_{yy} \\ M_{xy} \end{Bmatrix} = \begin{bmatrix} A_{11} & A_{12} & 0 & 0 & 0 & 0 \\ A_{12} & A_{22} & 0 & 0 & 0 & 0 \\ 0 & 0 & A_{66} & 0 & 0 & 0 \\ 0 & 0 & 0 & D_{11} & D_{12} & 0 \\ 0 & 0 & 0 & D_{12} & D_{22} & 0 \\ 0 & 0 & 0 & 0 & 0 & D_{66} \end{bmatrix} \begin{Bmatrix} \overline{\epsilon}_{xx} \\ \overline{\epsilon}_{yy} \\ \overline{\gamma}_{xy} \\ \kappa_{xx} \\ \kappa_{yy} \\ \kappa_{xy} \end{Bmatrix}. \tag{3.17}$$

Due to the varying radius, thickness differences may arise from overlaps. Furthermore, the fiber angle of the plies varies along the meridional and/or circumferential coordinate, depending on the manufacturing technique. As a result, the thickness and stiffness properties are a function of the coordinates. For simplicity, these effects is not considered in the analysis here: the thickness, the membrane stiffness matrix $\boldsymbol{A}$ and the flexural stiffness matrix $\boldsymbol{D}$ are assumed to be constant for the whole conical shell. In addition, it is assumed that the plies are perfectly bonded to each other.

The scaling methodology will not only be applied to composite conical shells, but also to isotropic conical shells. This gives insight in the prediction accuracy of the methodology for a simplified case, which satisfies the laminate assumptions automatically (i.e. symmetry, balance and negligible flexural anisotropy). An isotropic shell can be understood as a one-layer composite with thickness t, Young's modulus $E = E_{11} = E_{22}$, Poisson's ratio $\nu = \nu_{12} = \nu_{21}$ and shear modulus $G = G_{12} = \frac{E}{2(1+\nu)}$. Consequently, the elastic matrices are given by

$$[\boldsymbol{A}] = \frac{Et}{1-\nu^2} \begin{bmatrix} 1 & \nu & 0 \\ \nu & 1 & 0 \\ 0 & 0 & \frac{1-\nu}{2} \end{bmatrix} \tag{3.18a}$$

and

$$[\boldsymbol{D}] = \frac{Et^3}{12(1-\nu^2)} \begin{bmatrix} 1 & \nu & 0 \\ \nu & 1 & 0 \\ 0 & 0 & \frac{1-\nu}{2} \end{bmatrix} \tag{3.18b}$$

3.3.3 Equilibrium Equations

The equilibrium equations are derived using the principle of stationary total potential energy. This implies that the first variation of the potential energy must equal zero, i.e. $\delta\Pi = 0$ [25,84]. The total potential energy Π is given by

$$\Pi = U + V \tag{3.19}$$

where U denotes the internal strain energy and V the energy due to the external loading. The internal strain energy is given by

$$U = \frac{1}{2} \int_C \{\boldsymbol{\sigma}\}^T \{\boldsymbol{\epsilon}\} \, \mathrm{d}C \tag{3.20}$$

in which C denotes the volume. The integral over the thickness can be carried out using Equation 3.12, such that

$$U = \frac{1}{2}\int_x\int_y \left(N_{xx}\overline{\epsilon}_{xx} + N_{yy}\overline{\epsilon}_{yy} + N_{xy}\overline{\gamma}_{xy} + M_{xx}\kappa_{xx} + M_{yy}\kappa_{yy} + M_{xy}\kappa_{xy}\right)\mathrm{d}y\,\mathrm{d}x\,. \tag{3.21}$$

The energy due to external loading V is given by

$$\begin{aligned} V = &-\int_x\int_y \left(q_u u + q_v v + q_w w\right)\,\mathrm{d}y\,\mathrm{d}x \\ &-\int_y \left(\hat{N}_{xx}u + \hat{N}_{xy}v + \hat{Q}w + \hat{M}_{xx}w_{,x}\right)\,\mathrm{d}y\,\Big|_{x=0}^{x=L} \end{aligned} \tag{3.22}$$

where q_u, q_v and q_w are the external distributed loading in the axial, circumferential, and normal directions, respectively. $\hat{N}_{xx}$, $\hat{N}_{xy}$, $\hat{Q}$ and $\hat{M}_{xx}$ are the axial, torsional, shearing forces and the bending moment, respectively, applied at the two ends of the conical shell, where $x = 0$ and $x = L$. Here, only axial compression is considered, such that the energy due to external loading simplifies to

$$V = -\int_y \left(\hat{N}_{xx}u\right)\,\mathrm{d}y\,\Big|_{x=0}^{x=L}\,. \tag{3.23}$$

Summarizing, the total potential energy is given by

$$\begin{aligned} \Pi = \frac{1}{2}\int_x\int_y &\left(N_{xx}\overline{\epsilon}_{xx} + N_{yy}\overline{\epsilon}_{yy} + N_{xy}\overline{\gamma}_{xy} + M_{xx}\kappa_{xx} + M_{yy}\kappa_{yy} + M_{xy}\kappa_{xy}\right)\mathrm{d}y\,\mathrm{d}x \\ &-\int_y \left(\hat{N}_{xx}u\right)\,\mathrm{d}y\,\Big|_{x=0}^{x=L}\,. \end{aligned} \tag{3.24}$$

The equilibrium equations can be found by evaluation of the Euler-Lagrange equations of the calculus of variations [84] given by

$$\frac{\partial F}{\partial u} - \frac{\partial}{\partial x}\frac{\partial F}{\partial u_{,x}} - \frac{\partial}{\partial y}\frac{\partial F}{\partial u_{,y}} = 0\,, \tag{3.25a}$$

$$\frac{\partial F}{\partial v} - \frac{\partial}{\partial x}\frac{\partial F}{\partial v_{,x}} - \frac{\partial}{\partial y}\frac{\partial F}{\partial v_{,y}} = 0\,, \tag{3.25b}$$

$$\frac{\partial F}{\partial w} - \frac{\partial}{\partial x}\frac{\partial F}{\partial w_{,x}} - \frac{\partial}{\partial y}\frac{\partial F}{\partial w_{,y}} + \frac{\partial^2}{\partial x^2}\frac{\partial F}{\partial w_{,xx}} + \frac{\partial^2}{\partial y^2}\frac{\partial F}{\partial w_{,yy}} + \frac{\partial^2}{\partial x \partial y}\frac{\partial F}{\partial w_{,xy}} = 0\,. \tag{3.25c}$$

In the equations above, F is the integrand of the total potential energy. More specifically,

$$\Pi = \int_x\int_y F\left(u, u_{,x}, u_{,y}, v, v_{,x}, v_{,y}, w, w_{,x}, w_{,y}, w_{,xx}, w_{,yy}, w_{,xy}\right)\mathrm{d}y\,\mathrm{d}x\,. \tag{3.26}$$

Substitution of the kinematic relations and the constitutive relations into the energy expressions allows to express F in terms of the displacements, namely

$$\begin{aligned} F =& \frac{1}{2}\Bigg[A_{11}\left(u_{,x}+\frac{1}{2}w_{,x}^2\right)^2 + A_{22}\left(v_{,y}+\frac{\cos\alpha}{r(x)}w+\frac{1}{2}w_{,y}^2\right)^2 \\ &+ 2A_{12}\left(u_{,x}+\frac{1}{2}w_{,x}^2\right)\left(v_{,y}+\frac{\cos\alpha}{r(x)}w+\frac{1}{2}\frac{1}{r^2(x)}w_{,y}^2\right) \\ &+ A_{66}\left(u_{,y}+v_{,x}+w_{,x}w_{,y}\right)^2\Bigg] \\ &+ \frac{1}{2}\left[D_{11}w_{,xx}^2 + D_{22}w_{,yy}^2 + 2D_{12}\,w_{,xx}w_{,yy} + D_{66}(-2\,w_{,xy})^2\right]. \end{aligned} \tag{3.27}$$

The first derivatives of F with respect to the displacements and their derivatives are taken and substituted into Equation 3.25. This yields to the following equilibrium equations, in agreement with the general shell equilibrium equations [77].

$$N_{xx,x} + N_{xy,y} = 0\,, \tag{3.28a}$$

$$N_{xy,x} + N_{yy,y} = 0\,, \tag{3.28b}$$

$$M_{xx,xx} + 2M_{xy,xy} + M_{yy,yy} - \frac{\cos\alpha}{r(x)}N_{yy} + N_{xx}\,w_{,xx} + N_{yy}\,w_{,yy} + 2N_{xy}\,w_{,xy} = 0\,. \tag{3.28c}$$

3.3.4 Stability Equations

The stability equations are determined using the perturbation technique, also called the method of adjacent equilibrium [8, 77]. Prior to buckling, the shell is assumed to be in a primary equilibrium state, described by displacement field (u^p, v^p, w^p). Near the point of buckling, it is assumed that there exists an adjacent equilibrium state, $(\widetilde{u}, \widetilde{v}, \widetilde{w})$, sufficiently close to the primary equilibrium state, such that $\widetilde{u}, \widetilde{v}$, and $\widetilde{w}$ are infinitesimally small. In addition, it is assumed that the conical shell is in a membrane state prior to buckling. This implies there is no out-of-plane displacement, $w^p = 0$, and that the derivatives of w^p are also zero. This linearizes the strain-displacement relations. The total displacements are given by

$$u = u^p + \widetilde{u}\,, \tag{3.29a}$$

$$v = v^p + \widetilde{v}\,, \tag{3.29b}$$

$$w = 0 + \widetilde{w}\,. \tag{3.29c}$$

Consequently, the mid-surface strains and change of curvatures are given by

$$\{\overline{\boldsymbol{\epsilon}}\} = \{\overline{\boldsymbol{\epsilon}}^p\} + \left\{\widetilde{\overline{\boldsymbol{\epsilon}}}\right\} \tag{3.30a}$$

and

$$\{\boldsymbol{\kappa}\} = \{\mathbf{0}\} + \{\widetilde{\boldsymbol{\kappa}}\} \tag{3.30b}$$

where

$$\{\overline{\boldsymbol{\epsilon}}^{\boldsymbol{p}}\} = \begin{Bmatrix} u_{,x} \\ v_{,y} \\ u_{,y} + v_{,x} \end{Bmatrix}, \tag{3.31}$$

$$\left\{\widetilde{\overline{\boldsymbol{\epsilon}}}\right\} = \begin{Bmatrix} \widetilde{u}_{,x} \\ \widetilde{v}_{,y} + \frac{\cos\alpha}{r(x)}\widetilde{w} \\ \widetilde{u}_{,y} + \widetilde{v}_{,x} \end{Bmatrix}, \tag{3.32}$$

and

$$\{\widetilde{\boldsymbol{\kappa}}\} = \begin{Bmatrix} -\widetilde{w}_{,xx} \\ -\widetilde{w}_{,yy} \\ -2\,\widetilde{w}_{,xy} \end{Bmatrix}. \tag{3.33}$$

Note that products of the variations are neglected in accordance with the assumption that the variations are infinitesimally small [77]. The membrane forces and the bending moments per unit length are

$$\begin{Bmatrix} \{\boldsymbol{N}\} \\ \{\boldsymbol{M}\} \end{Bmatrix} = \begin{Bmatrix} \{\boldsymbol{N^p}\} \\ \{\boldsymbol{M^p}\} \end{Bmatrix} + \begin{Bmatrix} \left\{\widetilde{\boldsymbol{N}}\right\} \\ \left\{\widetilde{\boldsymbol{M}}\right\} \end{Bmatrix}. \tag{3.34}$$

The constitutive equations of the variations are consequently given by

$$\begin{Bmatrix} \left\{\widetilde{\boldsymbol{N}}\right\} \\ \left\{\widetilde{\boldsymbol{M}}\right\} \end{Bmatrix} = \begin{bmatrix} \boldsymbol{A} & \boldsymbol{0} \\ \boldsymbol{0} & \boldsymbol{D} \end{bmatrix} \begin{Bmatrix} \left\{\widetilde{\overline{\boldsymbol{\epsilon}}}\right\} \\ \{\widetilde{\boldsymbol{\kappa}}\} \end{Bmatrix}. \tag{3.35}$$

No increment is applied to the external load. As the new state should still be in equilibrium, Equation 3.34 is substituted into the equilibrium equations in Equation 3.28. As a result,

$$\left(N^p_{xx} + \widetilde{N}_{xx}\right)_{,x} + \left(N^p_{xy} + \widetilde{N}_{xy}\right)_{,y} = 0\,, \tag{3.36a}$$

$$\left(N^p_{yy} + \widetilde{N}_{yy}\right)_{,y} + \left(N^p_{xy} + \widetilde{N}_{xy}\right)_{,x} = 0\,, \tag{3.36b}$$

$$\begin{aligned} &\left(M^p_{xx} + \widetilde{M}_{xx}\right)_{,xx} + 2\left(M^p_{xy} + \widetilde{M}_{xy}\right)_{,xy} + \left(M^p_{yy} + \widetilde{M}_{yy}\right)_{,yy} - \frac{\cos\alpha}{r(x)}\left(N^p_{yy} + \widetilde{N}_{yy}\right) \\ &+ \left(N^p_{xx} + \widetilde{N}_{xx}\right)\widetilde{w}_{,xx} + \left(N^p_{yy} + \widetilde{N}_{yy}\right)\widetilde{w}_{,yy} + 2\left(N^p_{xy} + \widetilde{N}_{xy}\right)\widetilde{w}_{,xy} = 0\,. \end{aligned} \tag{3.36c}$$

The terms related to the primary equilibrium state can be isolated to satisfy equilibrium for this state. As a result, the stability equations are obtained. The terms of quadratic degree and higher in the variations are neglected in accordance with the assumption that the variations are infinitesimally small. The stability equations, in agreement with the stability equations for a general shell [77], are given by

$$\widetilde{N}_{xx,x} + \widetilde{N}_{xy,y} = 0\,, \tag{3.37a}$$

$$\widetilde{N}_{xy,x} + \widetilde{N}_{yy,y} = 0\,, \tag{3.37b}$$

$$\widetilde{M}_{xx,xx} + 2\widetilde{M}_{xy,xy} + \widetilde{M}_{yy,yy} - \frac{\cos\alpha}{r(x)}\widetilde{N}_{yy} + N^p_{xx}\widetilde{w}_{,xx} + N^p_{yy}\widetilde{w}_{,yy} + 2N^p_{xy}\widetilde{w}_{,xy} = 0\,. \tag{3.37c}$$

Because of the assumed membrane state, the primary membrane forces for a conical shell axially compressed by load P [8] are given by

$$N^p_{xx} = \frac{P}{2\pi r(x)\cos\alpha}\,, \tag{3.38a}$$

$$N^p_{yy} = 0\,, \tag{3.38b}$$

$$N^p_{xy} = 0\,, \tag{3.38c}$$

such that the stability equations simplify to

$$\widetilde{N}_{xx,x} + \widetilde{N}_{xy,y} = 0\,, \tag{3.39a}$$

$$\widetilde{N}_{xy,x} + \widetilde{N}_{yy,y} = 0\,, \tag{3.39b}$$

$$\widetilde{M}_{xx,xx} + 2\widetilde{M}_{xy,xy} + \widetilde{M}_{yy,yy} - \frac{\cos\alpha}{r(x)}\widetilde{N}_{yy} + N^p_{xx}\widetilde{w}_{,xx} = 0\,. \tag{3.39c}$$

3.3.5 Stress Function Formulation

To make the stability equations nondimensional, a stress function $\widetilde{\phi}$ is introduced [77], defined by

$$\widetilde{N}_{xx} = \widetilde{\phi}_{,yy}\,, \tag{3.40a}$$

$$\widetilde{N}_{yy} = \widetilde{\phi}_{,xx}\,, \tag{3.40b}$$

$$\widetilde{N}_{xy} = -\widetilde{\phi}_{,xy}\,. \tag{3.40c}$$

Substitution of Equation 3.40 in the stability equations in Equation 3.39, shows that the first two stability equations are automatically satisfied. The third stability equation is written in terms of $\widetilde{\phi}$ and $\widetilde{w}$ making use of the stress function definition and the constitutive equations of the orthotropic laminate, such that

$$D_{11}\,\widetilde{w}_{,xxxx} + 2(D_{12} + 2\,D_{66})\widetilde{w}_{,xxyy} + D_{22}\,\widetilde{w}_{,yyyy} + \frac{\cos\alpha}{r(x)}\widetilde{\phi}_{,xx} - N^p_{xx}\widetilde{w}_{,xx} = 0\,. \tag{3.41}$$

As the first two stability equations have been eliminated, a compatibility equation is introduced to guarantee the continuity of the shell at mid-surface during deformation. The compatibility equation is obtained by eliminating u and v from the kinematic equations given

in Equation 3.6. Therefore, $\overline{\epsilon}_{xx}$ is differentiated twice with respect to y, $\overline{\epsilon}_{yy}$ twice with respect to x and $\overline{\gamma}_{xy}$ once with respect to x and once with respect to y.

$$\overline{\epsilon}_{xx,yy} = u_{,xyy} + w_{,x}\, w_{,xyy} + w_{,xy}^2\,, \tag{3.42a}$$

$$\overline{\epsilon}_{yy,xx} = v_{,yxx} + w_{,y}\, w_{,xxy} + w_{,xy}^2 + \left(\frac{\cos\alpha}{r(x)} w\right)_{,xx}\,, \tag{3.42b}$$

$$\overline{\gamma}_{xy,xy} = u_{,xyy} + v_{,xxy} + w_{,y}\, w_{,xxy} + w_{,xy}^2 + w_{,xx}\, w_{,yy} + w_{,x}\, w_{,xyy}\,. \tag{3.42c}$$

Displacements u and v are eliminated by substituting the expressions for $u_{,xyy}$ and $v_{,yxx}$ from the first two strains, respectively, into the shear strain expression,

$$\overline{\epsilon}_{xx,yy} + \overline{\epsilon}_{yy,xx} - \overline{\gamma}_{xy,xy} = w_{,xy}^2 - w_{,xx}\, w_{,yy} + \left(\frac{\cos\alpha}{r(x)} w\right)_{,xx}\,. \tag{3.43}$$

It is assumed that for shallow shells the curvatures are mildly varying [77], such that

$$\left(\frac{\cos\alpha}{r(x)} w\right)_{,xx} = \frac{\cos\alpha}{r(x)} w_{,xx}\,. \tag{3.44}$$

As a result, the compatibility equation is given by

$$\overline{\epsilon}_{xx,yy} + \overline{\epsilon}_{yy,xx} - \overline{\gamma}_{xy,xy} = w_{,xy}^2 - w_{,xx}\, w_{,yy} + \frac{\cos\alpha}{r(x)} w_{,xx}\,. \tag{3.45}$$

Applying the perturbation technique to the equation above and satisfying the equation for the primary equilibrium state, allows to determine the buckling compatibility equation,

$$\widetilde{\overline{\epsilon}}_{xx,yy} + \widetilde{\overline{\epsilon}}_{yy,xx} - \widetilde{\overline{\gamma}}_{xy,xy} = 2\, \widetilde{w}_{,xy}\, w_{,xy}^p - w_{,xx}^p\, \widetilde{w}_{,yy} - \widetilde{w}_{,xx}\, w_{,yy}^p + \frac{\cos\alpha}{r(x)} \widetilde{w}_{,xx} \tag{3.46}$$

where the terms of quadratic degree are already omitted. Neglecting the primary out-of-plane displacement w^p and its derivatives, yields

$$\widetilde{\overline{\epsilon}}_{xx,yy} + \widetilde{\overline{\epsilon}}_{yy,xx} - \widetilde{\overline{\gamma}}_{xy,xy} = \frac{\cos\alpha}{r(x)} \widetilde{w}_{,xx}\,. \tag{3.47}$$

To express this equation in terms of the stress function $\widetilde{\phi}$, use is made of the inverted form of the buckling constitutive equations

$$\widetilde{\overline{\epsilon}}_{xx} = a_{11}\, \widetilde{\phi}_{,yy} + a_{12}\, \widetilde{\phi}_{,xx}\,, \tag{3.48a}$$

$$\widetilde{\overline{\epsilon}}_{yy} = a_{12}\, \widetilde{\phi}_{,yy} + a_{22}\, \widetilde{\phi}_{,xx}\,, \tag{3.48b}$$

$$\widetilde{\overline{\gamma}}_{xy} = -a_{66}\, \widetilde{\phi}_{,xy}\,, \tag{3.48c}$$

where a_{ij} indicate the coefficients of the inverted form of the membrane constitutive equations, i.e. $[\boldsymbol{a}] = [\boldsymbol{A}]^{-1}$. For asymmetric laminates, $[\boldsymbol{a}]$ also depends on the $[\boldsymbol{B}]$ and $[\boldsymbol{D}]$ stiffness matrices.

Substituting this result in the buckling compatibility equation, yields

$$a_{22}\, \widetilde{\phi}_{,xxxx} + (2a_{12} + a_{66})\, \widetilde{\phi}_{,xxyy} + a_{11}\, \widetilde{\phi}_{,yyyy} = \frac{\cos\alpha}{r(x)} \widetilde{w}_{,xx}\,. \tag{3.49}$$

3.3.6 Summary: Dimensional Governing Equations

Summarizing, the buckling problem is now described by the stability equation,

$$D_{11}\,\widetilde{w}_{,xxxx} + 2(D_{12} + 2\,D_{66})\widetilde{w}_{,xxyy} + D_{22}\,\widetilde{w}_{,yyyy} + \frac{\cos\alpha}{r(x)}\widetilde{\phi}_{,xx} - N^{p}_{xx}\widetilde{w}_{,xx} = 0\,, \tag{3.50}$$

and the compatibility equation,

$$a_{22}\,\widetilde{\phi}_{,xxxx} + (2a_{12} + a_{66})\,\widetilde{\phi}_{,xxyy} + a_{11}\,\widetilde{\phi}_{,yyyy} = \frac{\cos\alpha}{r(x)}\widetilde{w}_{,xx}\,. \tag{3.51}$$

3.4 Semi-analytical Solution

The governing equations described above have variable coefficients, such that a solution to the buckling problem is not easily obtained. It was already discussed in the literature study that there is no closed form buckling solution for composite conical shells in axial compression. It is, however, convenient to have a semi-analytical solution at hand to calculate the buckling load without having to run expensive finite element analyses. A semi-analytical solution has been developed by Schiffner [85] (in German) and by Zhang [86] for the buckling of orthotropic conical shells, which will be used in consequent analyses. Because the solution is rather elaborate, it is shortly explained in this section how it is derived. For clarity, some of the notations of Zhang are changed to the conventions used here.

For the derivation of the semi-analytical solution, Zhang makes use of a (s, θ) system, which is shown in Figure 3.4. Because of this different coordinate system, the varying radius $r(s)$ is given by

$$r(s) = s\,\sin\alpha\,. \tag{3.52}$$

The meridional coordinate s ranges from s_1 at the small radius edge to s_2 at the large radius edge. Circumferential angle coordinate θ ranges from 0 to 2π.

The governing equations are derived using the same assumptions and in a similar way as in section 3.3. As a result, the stability behavior is described by equations similar to Equation 3.50 and Equation 3.51, but in the different coordinate system. To reduce the number of variable coefficients, a change of variables from s to ζ is introduced, given by

$$s = s_1 \mathrm{e}^{\zeta}\,. \tag{3.53}$$

In addition, the stiffness and compliance parameters are made nondimensional using an isotropic equivalent, namely

$$a^{*}_{ij} = E_{11}t\,a_{ij}\,, \tag{3.54a}$$

$$D^{*}_{ij} = \frac{12(1-\nu^{2}_{12})}{E_{11}t^{3}}\,D_{ij}\,. \tag{3.54b}$$

Consequently, a skewed buckling pattern is assumed, which satisfies the boundary conditions that the out-of-plane deformation is zero at the edges. Applying the method of undetermined

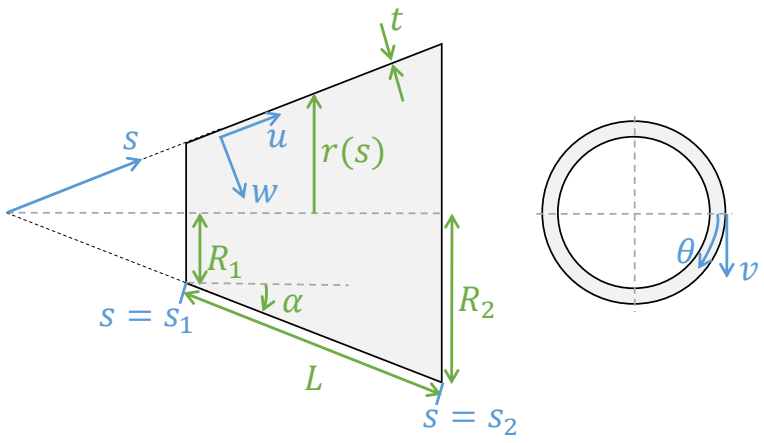

Figure 3.4: Coordinate system and conical shell used for the semi-analytical solution, based on [86].

coefficients to the compatibility equation, the solution for the stress function is found. Finally, Galerkin's procedure is applied and a solution is found, given by

$$\lambda_{m,n} = \frac{c(4k^2+1)\tan\alpha}{(1-e^{-\zeta_0})s_1 t(1+2k^2)}\left[\frac{t^2(1-e^{-2\zeta_0})\gamma_{D^*,m,n}}{16c^2} + \frac{s_1^2\zeta_0(1+k^2)}{2\gamma_{a^*,m,n}\tan^2\alpha}\right] \tag{3.55}$$

where

$$\gamma_{D^*,m,n} = D_{11}^*(k^2-2) + D_{22}^*\left[1+\frac{(1-n^2)^2}{1+k^2}\right] + 2\left(D_{12}^*+2D_{66}^*\right)n^2\,, \tag{3.56a}$$

$$\gamma_{a^*,m,n} = a_{11}^*(1-n^2)^2 + \left(a_{11}^*+a_{22}^*\right)k^2 + a_{22}^*k^4 + \left(2a_{12}^*+a_{66}^*\right)n^2k^2\,, \tag{3.56b}$$

$$c = \sqrt{3(1-\nu_{12}^2)}\,, \tag{3.56c}$$

$$k = \frac{m\pi}{\zeta_0}\,, \tag{3.56d}$$

$$n = \frac{n_1}{\sin\alpha}\,, \tag{3.56e}$$

$$\zeta_0 = \ln\frac{s_2}{s_1}\,. \tag{3.56f}$$

In the equations above, n_1 is the number of circumferential full waves and m is the number of meridional half-waves. The solution given in Equation 3.55 is minimized with respect to these two parameters, which characterize the buckling mode (m,n). The relative buckling load $\lambda_{m,n}$ is then converted to the buckling load P_{cr} using

$$P_{\mathrm{cr}} = \lambda_{m,n}\cdot\frac{2\pi E_{11}t^2\cos^2\alpha}{c}\,. \tag{3.57}$$

3.5 Nondimensionalization of the Governing Equations

In section 3.3, the stability and compatibility equation for an orthotropic conical shell in axial compression are derived. These two governing equations, given by Equation 3.50 and Equation 3.51, are now made nondimensional. The nondimensionalization procedure defined by Nemeth for a general shell [77] is followed and applied to the case of the conical shell. If the nondimensional coefficients in the resulting equations are equal for two or more conical shells, the equations describing the buckling behavior are identical. As a result, the buckling behavior is expected to be identical for those two or more shells.

The equations are made nondimensional by introducing nondimensional coordinates $z_1 = x/L$ and $z_2 = y/r(x)$. The varying radius of the conical shell is consequently expressed as

$$r(z_1) = R_1 + L\, z_1\, \sin\alpha\,. \tag{3.58}$$

3.5.1 Compatibility Equation

The nondimensional coordinates z_1 and z_2 are introduced into the compatibility equation, Equation 3.51, and the equation is multiplied with $\frac{L^2\, r^2(z_1)}{\sqrt{a_{11}\, a_{22}}}$, such that

$$\begin{aligned}\frac{a_{22}}{L^4}\frac{L^2\, r^2(z_1)}{\sqrt{a_{11}\, a_{22}}}\frac{\partial^4\widetilde{\phi}}{\partial z_1^4} + \frac{2\, a_{12} + a_{66}}{L^2\, r^2(z_1)}\frac{L^2\, r^2(z_1)}{\sqrt{a_{11}\, a_{22}}}\frac{\partial^4\widetilde{\phi}}{\partial z_1^2 \partial z_2^2} + \frac{a_{11}}{r^4(z_1)}\frac{L^2\, r^2(z_1)}{\sqrt{a_{11}\, a_{22}}}\frac{\partial^4\widetilde{\phi}}{\partial z_2^4} \\ = \frac{\cos\alpha}{r(z_1)\, L^2}\frac{L^2\, r^2(z_1)}{\sqrt{a_{11}\, a_{22}}}\frac{\partial^2\widetilde{w}}{\partial z_1^2}\,.\end{aligned} \tag{3.59}$$

Upon rewriting,

$$\alpha_m^2\frac{\partial^4\widetilde{\phi}}{\partial z_1^4} + 2\mu\frac{\partial^4\widetilde{\phi}}{\partial z_1^2 \partial z_2^2} + \frac{1}{\alpha_m^2}\frac{\partial^4\widetilde{\phi}}{\partial z_2^4} = \frac{\cos\alpha\, r(z_1)}{\sqrt{a_{11}\, a_{22}}}\frac{\partial^2\widetilde{w}}{\partial z_1^2} \tag{3.60}$$

where two nondimensional membrane coefficients are introduced. The membrane parameter α_m and the membrane orthotropy parameter μ are respectively given by

$$\alpha_m = \frac{r(z_1)}{L}\left(\frac{a_{22}}{a_{11}}\right)^{0.25} \tag{3.61a}$$

and

$$\mu = \frac{2\, a_{12} + a_{66}}{2\sqrt{a_{11}\, a_{22}}}\,. \tag{3.61b}$$

In order to make the equation of order one, the equation is multiplied by $\frac{1}{\sqrt{D_{11}\, D_{22}}}$. Consequently, the newly defined nondimensional stress function $\widetilde{\Phi}$, given by

$$\widetilde{\Phi} = \frac{\widetilde{\phi}}{\sqrt{D_{11}\, D_{22}}}\,, \tag{3.62}$$

can be substituted in the compatibility equation. Furthermore, the out-of-plane displacement $\widetilde{w}$ is replaced by its nondimensional counterpart $\widetilde{W}$ defined by

$$\widetilde{W} = \frac{\widetilde{w}}{(a_{11}a_{22}D_{11}D_{22})^{0.25}}\,. \tag{3.63}$$

The nondimensional compatibility equation is given by

$$\alpha_m^2 \frac{\partial^4 \widetilde{\Phi}}{\partial z_1^4} + 2\mu \frac{\partial^4 \widetilde{\Phi}}{\partial z_1^2 \partial z_2^2} + \frac{1}{\alpha_m^2}\frac{\partial^4 \widetilde{\Phi}}{\partial z_2^4} = \sqrt{12}\, Z_2 \frac{\partial^2 \widetilde{W}}{\partial z_1^2}\,, \tag{3.64}$$

where the equivalent Batdorf-Stein parameter Z_2 is defined by

$$Z_2 = \frac{r(z_1)\cos\alpha}{\sqrt{12}\,(a_{11}a_{22}D_{11}D_{22})^{0.25}}\,. \tag{3.65}$$

3.5.2 Stability Equation

The nondimensional coordinates z_1 and z_2 are introduced into the stability equation, Equation 3.50, and the equation is multiplied with $\frac{L^2\, r^2(z_1)}{\sqrt{D_{11}\, D_{22}}}$, such that

$$\begin{aligned}\frac{D_{11}}{L^4}\frac{L^2\, r^2(z_1)}{\sqrt{D_{11}\, D_{22}}}\frac{\partial^4 \widetilde{w}}{\partial z_1^4} + 2\frac{D_{12}+2\,D_{66}}{L^2\, r^2(z_1)}\frac{L^2\, r^2(z_1)}{\sqrt{D_{11}\, D_{22}}}\frac{\partial^4 \widetilde{w}}{\partial z_1^2 \partial z_2^2} + \frac{D_{22}}{r^4(z_1)}\frac{L^2\, r^2(z_1)}{\sqrt{D_{11}\, D_{22}}}\frac{\partial^4 \widetilde{w}}{\partial z_2^4} \\ + \frac{\cos\alpha}{r(z_1)\, L^2}\frac{L^2\, r^2(z_1)}{\sqrt{D_{11}\, D_{22}}}\frac{\partial^2 \widetilde{\phi}}{\partial z_1^2} - \frac{N_{xx}^p}{L^2}\frac{L^2\, r^2(z_1)}{\sqrt{D_{11}\, D_{22}}}\frac{\partial^2 \widetilde{w}}{\partial z_1^2} = 0\end{aligned}\,. \tag{3.66}$$

Upon rewriting,

$$\alpha_b^2 \frac{\partial^4 \widetilde{w}}{\partial z_1^4} + 2\beta \frac{\partial^4 \widetilde{w}}{\partial z_1^2 \partial z_2^2} + \frac{1}{\alpha_b^2}\frac{\partial^4 \widetilde{w}}{\partial z_2^4} + \frac{r(z_1)\,\cos\alpha}{\sqrt{D_{11}\, D_{22}}}\frac{\partial^2 \widetilde{\phi}}{\partial z_1^2} - K_{xx}\frac{\partial^2 \widetilde{w}}{\partial z_1^2} = 0\,, \tag{3.67}$$

where two nondimensional flexural coefficients are introduced, as well as the nondimensional loading parameter. The bending parameter α_b, the flexural orthotropy parameter β and the loading parameter K_{xx} are respectively given by

$$\alpha_b = \frac{r(z_1)}{L}\left(\frac{D_{11}}{D_{22}}\right)^{0.25}\,, \tag{3.68a}$$

$$\beta = \frac{D_{12}+2\,D_{66}}{\sqrt{D_{11}\, D_{22}}}\,, \tag{3.68b}$$

$$K_{xx} = \frac{N_{xx}^p r^2(z_1)}{\sqrt{D_{11}\, D_{22}}}\,. \tag{3.68c}$$

Multiplying the equation with $(a_{11}a_{22}D_{11}D_{22})^{0.25}$, such that $\widetilde{W}$ can be introduced and substituting Equation 3.62, gives the following nondimensional stability equation

$$\alpha_b^2 \frac{\partial^4 \widetilde{W}}{\partial z_1^4} + 2\beta \frac{\partial^4 \widetilde{W}}{\partial z_1^2 \partial z_2^2} + \frac{1}{\alpha_b^2}\frac{\partial^4 \widetilde{W}}{\partial z_2^4} + \sqrt{12}\, Z_2 \frac{\partial^2 \widetilde{\Phi}}{\partial z_1^2} - K_{xx}\frac{\partial^2 \widetilde{W}}{\partial z_1^2} = 0\,. \tag{3.69}$$

3.5.3 Summary: Nondimensional Governing Equations

The nondimensional equations to describe the stability behavior of an orthotropic conical shell in axial compression have been determined. They are summarized below for clarity.

The compatibility equation,

$$\alpha_m^2 \frac{\partial^4 \widetilde{\Phi}}{\partial z_1^4} + 2\mu \frac{\partial^4 \widetilde{\Phi}}{\partial z_1^2 \partial z_2^2} + \frac{1}{\alpha_m^2} \frac{\partial^4 \widetilde{\Phi}}{\partial z_2^4} = \sqrt{12}\, Z_2 \frac{\partial^2 \widetilde{W}}{\partial z_1^2}\,, \tag{3.70}$$

and the stability equation,

$$\alpha_b^2 \frac{\partial^4 \widetilde{W}}{\partial z_1^4} + 2\beta \frac{\partial^4 \widetilde{W}}{\partial z_1^2 \partial z_2^2} + \frac{1}{\alpha_b^2} \frac{\partial^4 \widetilde{W}}{\partial z_2^4} + \sqrt{12}\, Z_2 \frac{\partial^2 \widetilde{\Phi}}{\partial z_1^2} - K_{xx} \frac{\partial^2 \widetilde{W}}{\partial z_1^2} = 0\,. \tag{3.71}$$

In the equations above, the membrane parameter α_m and bending parameter α_b are given by

$$\alpha_m = \frac{r(z_1)}{L} \left(\frac{a_{22}}{a_{11}} \right)^{0.25}\,, \tag{3.72a}$$

$$\alpha_b = \frac{r(z_1)}{L} \left(\frac{D_{11}}{D_{22}} \right)^{0.25}\,. \tag{3.72b}$$

The membrane orthotropy parameter μ and flexural orthotropy parameter β are defined as

$$\mu = \frac{2\, a_{12} + a_{66}}{2\sqrt{a_{11}\, a_{22}}}\,, \tag{3.72c}$$

$$\beta = \frac{D_{12} + 2\, D_{66}}{\sqrt{D_{11}\, D_{22}}}\,. \tag{3.72d}$$

The equivalent Batdorf-Stein parameter Z_2 is specified as

$$Z_2 = \frac{r(z_1) \cos\alpha}{\sqrt{12}\, (a_{11}\, a_{22}\, D_{11}\, D_{22})^{0.25}}\,, \tag{3.72e}$$

and the loading parameter K_{xx}, making use of Equation 3.38a, is given by

$$K_{xx} = \frac{N_{xx}^p r^2(z_1)}{\sqrt{D_{11}\, D_{22}}} = \frac{P\, r(z_1)}{2\pi \cos\alpha \sqrt{D_{11}\, D_{22}}}\,, \tag{3.72f}$$

3.5.4 Particularization for Isotropic Conical Shells

It was already mentioned in subsection 3.3.2 that the scaling methodology will also be applied to an isotropic conical shell. This allows to evaluate the prediction accuracy of the methodology for a conical shell which automatically satisfies the assumptions regarding symmetry, balance and negligible flexural anisotropy parameters. Because of the simplified constitutive equations, the nondimensional coefficients can be simplified as well. The governing equations are still given by Equation 3.70 and Equation 3.71. Making use of the isotropic elastic

stiffnesses given in Equation 3.18, the membrane parameter α_m and bending parameter α_b become identical and equal to

$$\alpha_{mb} = \alpha_m = \alpha_b = \frac{r(z_1)}{L} \,. \tag{3.73a}$$

The orthotropy parameters μ and β simplify to

$$\mu = \beta = 1 \,, \tag{3.73b}$$

and the equivalent Batdorf-Stein parameter Z_2 becomes

$$Z_2 = \frac{r(z_1)\,\cos\alpha}{t}\sqrt{1-\nu^2} \,. \tag{3.73c}$$

Finally, the loading parameter K_{xx} simplifies to

$$K_{xx} = \frac{P\,r(z_1)}{2\pi\cos\alpha}\frac{12(1-\nu^2)}{Eh^3} \,. \tag{3.73d}$$

3.6 Scaling Methodology

The nondimensional governing equations of the symmetrically laminated, balanced composite conical shell in axial compression are found in the previous section. If the parameters in these equations are identical for two different shells, it is expected that their stability behavior up to the buckling point is identical. More specifically, it is expected that they have the same nondimensional buckling load and displacement, as well as the same deformation shape. In order to find these combinations of shells with identical parameters, a scaling methodology is created. The methodology aims to find an equivalent reduced-scale conical shell for a given full-scale conical shell. First, this methodology is set up for an isotropic shell, for which certain simplifications hold. Second, the methodology is set up for a composite shell with a symmetric, balanced layup with negligible flexural anisotropy.

3.6.1 Isotropic Conical Shells

The simplifications in the nondimensional parameters for isotropic conical shells are explained in subsection 3.5.4. Because the orthotropy parameters equal unity and the membrane and bending parameters are identical, there are less constraints on the reduced-scale shell design. The loading parameter K_{xx} will not be used for scaling, but will be used to evaluate the methodology by comparing K_{xx} for the full-scale and the reduced-scale conical shells. As a result, there are only two distinct parameters constraining the reduced-scale shell design, namely α_{mb} and Z_2. These parameters, however, are linear functions of the meridional coordinate z_1. In order to satisfy the parameters at each meridional location, they are matched at the two extremes, $z_1 = 0$ and $z_1 = 1$. The same holds for loading parameter K_{xx}. As a result, the following parameters are found,

$$\alpha_{mb,z_1=0} = \frac{R_1}{L} \,, \tag{3.74a}$$

$$\alpha_{mb,z_1=1} = \frac{R_1 + L\sin\alpha}{L}\,, \tag{3.74b}$$

$$Z_{2,z_1=0} = \frac{R_1\,\cos\alpha}{t}\sqrt{1-\nu^2}\,, \tag{3.74c}$$

$$Z_{2,z_1=1} = \frac{(R_1 + L\sin\alpha)\,\cos\alpha}{t}\sqrt{1-\nu^2}\,, \tag{3.74d}$$

$$K_{xx,z_1=0} = \frac{P\,R_1}{2\pi\cos\alpha}\frac{12(1-\nu^2)}{Eh^3}\,, \tag{3.74e}$$

$$K_{xx,z_1=1} = \frac{P\,(R_1 + L\sin\alpha)}{2\pi\cos\alpha}\frac{12(1-\nu^2)}{Eh^3}\,. \tag{3.74f}$$

Using these parameters, one can derive intuitive scaling rules such that there is full similarity, meaning that all scaling parameters are satisfied. If Equation 3.74a is identical for full-scale and reduced-scale shells, then it can be derived from Equation 3.74b that the cone angle α should also be identical for the two shells. Consequently, Equation 3.74c or Equation 3.74d can be used to determine the radius-to-thickness ratio, given the material has been chosen. These two equations will yield the same result, if all scaling parameters are satisfied. Similarly, Equation 3.74e and Equation 3.74f will yield the same load P.

Based on the reasoning above, the sequential methodology outlined in Figure 3.5 should be followed to scale a conical shell, isotropic or composite, to a fully similar isotropic conical shell. It is assumed that the geometry and the nondimensional parameters of the full-scale shell are known.

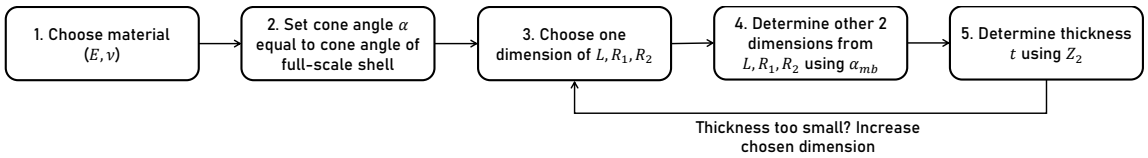

Figure 3.5: Scaling methodology procedure for isotropic conical shells.

Following this procedure, one finds a reduced-scale conical shell, fully similar to the full-scale conical shell. One can consequently analyze the buckling behavior of this reduced-scale conical shell and use Equation 3.74e and Equation 3.74f to estimate the buckling load of the full-scale conical shell. From the methodology, it becomes clear that there is some design freedom: the material and one of the dimensions (length, radius or thickness) can be chosen freely. Therefore, if the available test equipment allows for different cross-sectional sizes or lengths, but the manufacturing facility cannot produce very thin shells, it may be of interest to choose the thickness instead of the length or radius. The latter two parameters are then derived using Equation 3.74a to Equation 3.74d. Finally, it is noted that the scaling methodology allows for a sequential determination of the design parameters of the reduced-scale conical shell. No iteration is required to match the scaling parameters, which limits the computational effort.

3.6.2 Composite Conical Shells

This section discusses the scaling methodology for a composite conical shell with a symmetrically laminated, balanced layup. The nondimensional parameters are given in Equation 3.72.

This time, no further simplifications can be applied. To match the parameters dependent on z_1 for every point on the conical shell, the values at $z_1 = 0$ and at $z_1 = 1$ are used, in line with the isotropic shell.

It can be seen that Equation 3.72c and Equation 3.72d only depend on material and stacking sequence properties. As a result, they can be used first to determine the layup of the reduced-scale conical shell. Next, it can be seen that Equation 3.72a and Equation 3.72b at $z_1 = 0$ depend on two components: the radius-to-length ratio and the layup details. The latter has been fixed already, so α_m and α_b can be used to find a radius-to-length ratio of the reduced-scale shell. Subsequently, the cone angle can be determined using Equation 3.72a and Equation 3.72b at $z_1 = 1$. Finally, Equation 3.72e at $z_1 = 0$ and at $z_1 = 1$ can be used to determine the radius and the length. This results in the methodology given in Figure 3.6 to scale a conical shell, which can be isotropic or composite (symmetric, balanced layup with negligible flexural anisotropy), to a reduced-scale composite (symmetric, balanced layup with negligible flexural anisotropy) conical shell. It is assumed that the geometry and the nondimensional parameters are known for the full-scale shell.

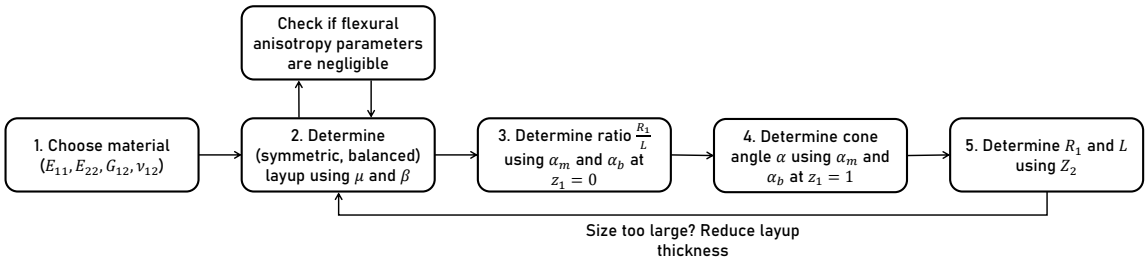

Figure 3.6: Scaling methodology procedure for composite conical shells.

The radius-to-length ratio determined in step 3 is only used to determine the cone angle α of the reduced-scale shell. The length and top radius are determined using the equivalent Batdorf-Stein parameter, because this parameter, also called the curvature parameter, is typically used to characterize the effect of geometry on the buckling behavior [70].

Following the methodology, it becomes clear that this problem is overly constraint: there are more scaling rules than reduced-scale conical shell properties to be chosen. More specifically, there are eight scaling rules, while there are only five shell properties to be determined: the material, stacking sequence, cone angle, small or large radius, and length. Furthermore, there are additional constraints from assumptions and for example, available materials. This is why it is suggested in the methodology to take the average value of the two equations if they cannot be satisfied simultaneously. This approach results in a sequential scaling methodology, such that the effort required for the reduced-scale design remains limited.

There is one type of laminate scaling for which some of the scaling rules from Equation 3.74 become linearly dependent, and thus redundant. This type of scaling is called ply-level scaling, which has been applied to cylindrical shells by Tabiei and Simitses [63]. Ply-level scaling entails that the full-scale structure with stacking sequence $[\theta_n/\gamma_n/...]_S$ is scaled to a reduced-scale structure, made of the same material, with stacking sequence $[\theta_m/\gamma_m/...]_S$ with $m < n$. This also implies that the geometry is scaled by a factor $\frac{m}{n}$ and that the cone angle of the two structures is identical. This type of scaling is investigated to evaluate the methodology for composite conical shells which satisfy all scaling parameters exactly.

Chapter 4

Analysis and Evaluation Methods

The scaling methodology has been set up in the previous chapter. It is evaluated by applying it to different conical shells. This allows to determine its strengths and limitations. The approach for this is visualized in Figure 4.1. First, it should be decided which full-scale (FS) shell will be scaled. Second, the reduced-scale (RS) conical shell is designed using the methodology. The full-scale conical shells and additional constraints for the reduced-scale designs are discussed in section 4.1. Third, the buckling behavior of the two shells is analyzed. The three methods used for this are explained in section 4.2. The details on the finite element modeling techniques are elaborated upon in section 4.3. Recall it is assumed that no failure occurs prior to buckling. This is checked when analyzing the buckling behavior, and is discussed in section 4.4. Finally, the scaling methodology is evaluated by comparing the buckling behavior of the two shells using the nondimensional parameters. This is explained in section 4.5.

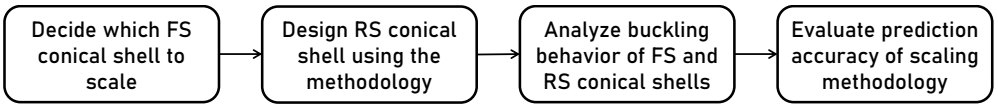

Figure 4.1: Flow chart for the evaluation of the scaling methodology. (FS = full-scale, RS = reduced-scale)

4.1 Conical Shell Details

As explained above, the design of the full-scale conical shells are detailed here. Additional constraints for the reduced-scale shells are also highlighted. Finally, the properties of the materials used for the shells are tabulated.

4.1.1 Full-Scale Reference Conical Shells

In order to evaluate the scaling methodology, it should be applied to large full-scale conical shells. Two conical shell structures from the Space Launch System (SLS) are used as references, visualized in Figure 4.2. The SLS is a heavy-lift launch vehicle in development by

NASA [87]. The structures considered here are representatives of the Universal Stage Adapter (USA) and the Payload Attach Fitting (PAF). The dimensions are taken from reference [20]. The structures analyzed in [20] are sandwich composite shells. For the evaluation of the scaling methodology, the material and stacking sequence are adjusted in order to capture the possibilities and limitations of the methodology. The geometry of the SLS USA and SLS PAF are given in Table 4.1. The main difference between the two shells lies in the cone angle. They are both considered here, in order to investigate the effects of the cone angle on the scaling.

Table 4.1: Geometry description of the SLS USA and PAF structure [20].

	Cone angle α **[deg]**	**Length** L **[mm]**	**Small radius** R_1 **[mm]**	**Large radius** R_2 **[mm]**
SLS USA	15	4996	2910	4203
SLS PAF	45	4831	787	4203

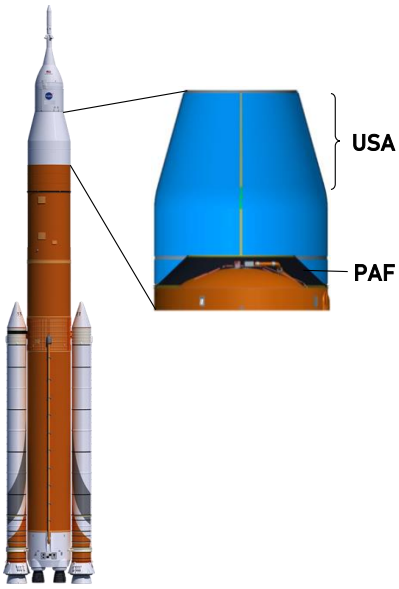

Figure 4.2: The Space Launch System in Block 1B Crew configuration, with Payload Attach Fitting (not visible from outside) and the Universal Stage Adapter [88].

4.1.2 Constraints for Reduced-Scale Conical Shells

The reduced-scale conical shells, which are designed to represent the reference full-scale shells, are subject to constraints from the scaling methodology. In addition, the test facility and manufacturing techniques put limitations on the design freedom of the reduced-scale shells. Typical test equipment sizes are assumed, such that the reduced-scale shells are constraint by the values given in Table 4.2. The limitations originating from the manufacturing technique and facilities are for example the ply angle accuracy and thickness accuracy for isotropic shells. These constraints are assumed to be out of the scope of this research and are therefore not taken into account. If there are concerns about the achievability of the reduced-scale conical shells, they are mentioned in their respective sections.

Table 4.2: Test equipment constraints for the reduced-scale conical shells [47, 89].

Max height H [mm]	Max radius R_2 [mm]	Max compressive load P_{cr} [kN]
1000	400	2500

Finally, recall that it is assumed that the flexural anisotropy is negligible. In subsection 3.3.2 it is explained how D_{16} and D_{26} can be kept low. Although these design guidelines are taken into account, the flexural anisotropy may be not negligible or the guidelines may conflict with the scaling parameters and test facility requirements. It is therefore checked if D_{16} and D_{26} are small with respect to D_{11}, D_{12}, D_{22} and D_{66}. Kassapoglou [83] used a threshold of 15% to verify this assumption for the buckling of plates. This will be used as a reference value.

4.1.3 Material Properties

The properties of all the materials considered in the research are summarized here. The scaling methodology is applied to isotropic, monolithic and sandwich composite conical shells.

- **Isotropic material: Aluminum alloy 2024-T4**

  For the isotropic conical shells, the aerospace graded aluminum alloy 2024-T4 is assumed. The relevant properties are summarized in Table 4.3.

Table 4.3: Material properties of aluminum alloy 2024-T4 [90].

E [MPa]	ν [-]	σ_y [MPa]	ρ [kg/m^3]
73100	0.33	324	2780

- **Composite facesheet material: IM7-8552 carbon fiber**

  For the monolithic shells and the facesheets of the sandwich composite shells, the properties of Hexcel IM7-8552 carbon fiber are used. They are given in Table 4.4 and Table 4.5.

Table 4.4: Stiffness material properties of IM7/8552 carbon fiber [91].

E_{11} [MPa]	E_{22} [MPa]	ν_{12} [-]	G_{12} [MPa]
149916	9370	0.36	5310
G_{13} [MPa]	G_{23} [MPa]	ρ [kg/m^3]	t_{ply} [mm]
5310	2655	1580	0.18

Table 4.5: Strength (F) and strain (E) material properties of IM7/8552 carbon fiber. Strength values are obtained from [91], strain values derived from strength and stiffness properties.

F_{11}^t [MPa]	F_{11}^c [MPa]	F_{22}^t [MPa]	F_{22}^c [MPa]	F_{12} [MPa]
2530	1724	64	286	91
S_{11}^t [$\mu\epsilon$]	S_{11}^c [$\mu\epsilon$]	S_{22}^t [$\mu\epsilon$]	S_{22}^c [$\mu\epsilon$]	S_{12} [$\mu\epsilon$]
16876	11500	6830	30523	17137

- **Core material: Aluminum honeycomb 3.1 pcf 1/8 inch-5056-.0007**

  The core of the sandwich composite shells is assumed to be made of hexagonal 5056 aluminum alloy honeycomb. The properties are summarized in Table 4.6. Note that the strength properties are not given, because core failure is not considered in the finite element models.

Table 4.6: Material properties of aluminum honeycomb 3.1 pcf 1/8-5056-.0007 [47].

E_{11} [MPa]	E_{22} [MPa]	ν_{12} [-]	G_{12} [MPa]
6.7	6.7	0.3	1.5
G_{13} [MPa]	G_{23} [MPa]	ρ [kg/m^3]	
138	310	49.7	

4.2 Analysis Methods

The buckling behavior of the conical shells is analyzed in three ways. This section explains these three approaches and their relevance.

4.2.1 Semi-analytical Solution

As a first step, the buckling behavior of the conical shells is analyzed using the semi-analytical solution given in section 3.4. This gives a first, fast indication of the buckling behavior in terms of the buckling load P_{cr} (see Equation 3.57) and buckling mode (m, n). The obtained buckling load P_{cr} is substituted in Equation 3.72f to obtain the nondimensional loading parameter K_{xx}, which can be compared for full-scale and reduced-scale shells. The predicted buckling modes are also compared.

The semi-analytical solution makes the same assumptions as the governing equations used for the scaling methodology. As a result, if all scaling parameters are satisfied, it is expected that the loading parameter, obtained with the buckling load from the semi-analytical solution, is identical for full-scale and reduced-scale shells. At the same time, it is expected that the semi-analytical solution overestimates the buckling load, because of the membrane prebuckling assumption, which linearizes the prebuckling solution, and the assumption on the deformation shape. The latter assumption results in not capturing buckling modes which do not fit the assumed shape. If these modes correspond to lower buckling loads, they are not found.

4.2.2 Linear Eigenvalue Analysis

As a second evaluation, a linear eigenvalue analysis is carried out in finite element software Abaqus. The subspace solver is opted over the Lanczos solver, because only the first few eigenmodes (i.e. less than 20) are of interest [45]. The eigensolver solves the system given by

$$\left(\boldsymbol{K}_M + \lambda^i \boldsymbol{K}_G\right) \boldsymbol{u}^i = \boldsymbol{0} \tag{4.1}$$

where $\boldsymbol{K}_M$ is the material stiffness matrix and $\boldsymbol{K}_G$ is the geometric stiffness matrix. The i-th eigenvalue is given by λ^i with corresponding eigenvector $\boldsymbol{u}^i$. The eigenvalue λ^i is the value of

λ for which the total stiffness matrix (i.e. the term between the brackets) becomes singular. The obtained eigenvalue is the scale factor with which the applied load should be multiplied to obtain the buckling load. The corresponding buckling mode is given by the eigenvector $\boldsymbol{u}^i$.

This analysis is linear and can consequently not capture the nonlinear behavior prior to buckling. At the same time, it takes into account the flexural anisotropy and puts no constraint on the possible deformation shape, so it is expected to be more accurate than the semi-analytical solution.

4.2.3 Implicit Dynamic Analysis

Lastly, a nonlinear analysis is performed, which can capture the nonlinearity before buckling as well as the postbuckling regime. It is decided to use a dynamic analysis, rather than a static analysis, because it is better at capturing the drop in stiffness right after buckling. The system given by

$$\boldsymbol{M}\ddot{\boldsymbol{u}} + \boldsymbol{C}\dot{\boldsymbol{u}} + \boldsymbol{K}\boldsymbol{u} = \boldsymbol{f} \tag{4.2}$$

is solved. Here, $\boldsymbol{M}$ is the mass matrix, $\boldsymbol{C}$ the damping matrix and $\boldsymbol{K}$ the total stiffness matrix. $\boldsymbol{u}$ and $\boldsymbol{f}$ are the displacement and external force vector, respectively.

The implicit solver is chosen over the explicit one for its computational efficiency. The model is set up such that real testing conditions are mimicked. To that end, a quasi-static application analysis is performed, in which the backward Euler operator is used for time integration [45]. The compression is applied as a displacement. This implies that a displacement rate has to be determined which balances the solution accuracy and the computational effort. This analysis allows to not only evaluate the buckling load, but also the deformation shape during the load application. Nonlinearity before buckling and the postbuckling behavior can be captured.

4.3 Finite Element Modeling Techniques

The last two analyses are performed in finite element software Abaqus. The approach for modeling the buckling phenomenon has to be determined. Here, the mesh size, the element type, load and boundary condition application, and other settings are elaborated upon. The mesh size and some of the implicit dynamic analysis settings depend on the shell size and other shell properties under consideration. This implies that the modeling techniques have to be determined for each analyzed shell separately. Here, all modeling techniques are determined for the full-scale SLS USA structure made of the isotropic aluminum alloy with a thickness of 4.5 mm. The geometry and material details can be found in Table 4.1 and Table 4.3, respectively. The same approach is followed for conical shells of different size and properties.

4.3.1 Mesh Convergence Study

In order to find an appropriate mesh size, a mesh convergence study is carried out. Four mesh sizes are compared, namely 200 mm, 100 mm, 50 mm and 25 mm. The comparison is carried out using a linear eigenvalue analysis with SC8R elements (see subsection 4.3.2). The 1 N reference load and the boundary conditions are applied as described in subsection 4.3.3.

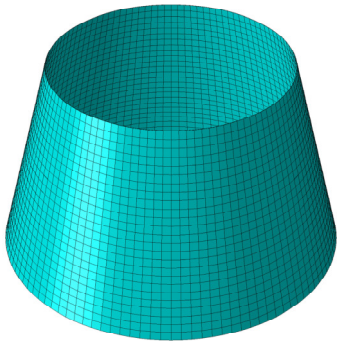

Figure 4.3: The structured mesh with size 200 mm.

As there are no irregularities in the geometry, such as cutouts, it is opted for a structured (regular) mesh, which is shown in Figure 4.3 for a mesh size of 200 mm.

The results are shown in Table 4.7. It should be noted that all analyses are carried out on the same computer (64-bit Intel® Core i5-4670 3.40 GHz CPU processor) and with the same settings, such that the CPU times can be compared. It can be seen that the CPU time increases drastically for decreasing mesh size. The obtained eigenvalues show convergence. Next to the eigenvalues, the first three eigenmodes are compared, shown in Figure 4.4. All mesh sizes result in the same buckling mode shape, but rotated around the central axis. It is decided to use the 50 mm mesh for the consequent analyses. This mesh gives a good balance between computational effort and accuracy of the eigenvalue and eigenmode. It is checked whether there are sufficient elements in each buckling half-wave to accurately represent the mode. This is shown in Figure 4.5. It can be seen that there are approximately five to six elements in one half-wave, which is above the minimum of three elements to capture the sinusoidal shape.

4.3.2 Element Type

Two element types are compared, namely the linear 4-node conventional shell element with reduced integration, S4R, and the linear 8-node continuum shell element with reduced integration, SC8R. These shell elements are considered because they are typically used for structures which have a very small thickness dimension compared to the other dimensions. They both follow the first-order shear deformation theory. The S4R element discretizes the shell to a reference surface, whereas the SC8R element is three-dimensional and has thus two nodes through the thickness. Furthermore, the nodes of the S4R element have six degrees of freedom, while the nodes of the SC8R element only have the three translational degrees of

Table 4.7: Mesh convergence study results for the full-scale isotropic conical shell. The difference with the smallest mesh size value is given between brackets.

Mesh size [mm]	200	100	50	25
Force eigenvalue 1 [kN]	5883 (+10.3%)	5575 (+4.50%)	5404 (+1.29%)	5335
Force eigenvalue 2 [kN]	5886 (+10.3%)	5575 (+4.50%)	5404 (+1.29%)	5335
Force eigenvalue 3 [kN]	5886 (+10.3%)	5577 (+4.52%)	5406 (+1.32%)	5336
CPU time [s]	47.0 (-98.5%)	80.6 (-97.4%)	490.7 (-83.9%)	3051

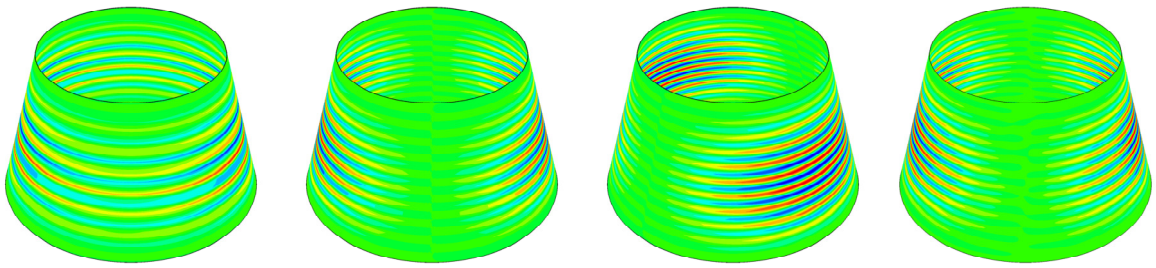

(a) Mesh size of 200 mm. **(b)** Mesh size of 100 mm. **(c)** Mesh size of 50 mm. **(d)** Mesh size of 25 mm.

Figure 4.4: The first eigenmode of the full-scale isotropic conical shell for various mesh sizes, showing radial displacement.

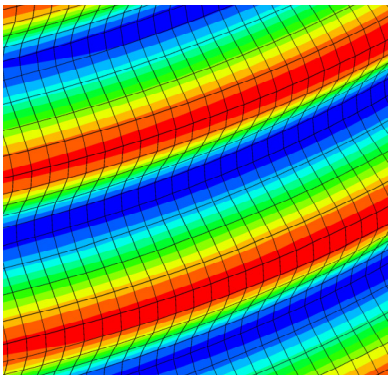

Figure 4.5: Close-up of the first buckling mode, showing the 50 mm mesh deformation.

freedom. The SC8R elements can be stacked on top of each other to obtain more detailed results through the thickness. This part of the behavior is not of specific interest, so only one element through the thickness is considered here.

The element type comparison is carried out using a linear eigenvalue analysis. The converged mesh of 50 mm is used, as well as the load and boundary condition application method as described in subsection 4.3.3. Both the load and the displacement eigenvalues are compared. In the latter case, the concentrated force is replaced by a reference displacement of 1 mm. The results are summarized in Table 4.8. The eigenvalues from the two analyses differ by a maximum of 1.37%. The SC8R element analyses require slightly less CPU time than the S4R element analyses. Next, the eigenmodes corresponding to the first three force eigenvalues are shown in Figure 4.6 for both element types. All three modes are nearly identical for the two element types, they are rotations of more or less the same mode around the central axis. Based on this analysis, no significant difference between the two element types is observed. It is decided to use the SC8R element for consequent analyses, because the behavior is similar and the CPU time is slightly lower. This difference may become larger for the more expensive nonlinear analyses.

4.3.3 Load and Boundary Condition Application

The load and boundary conditions are applied to reference points, which are tied to the edge nodes using rigid body tie constraints, as visualized in Figure 4.7. This constraint connects

Table 4.8: The first three force and displacement eigenvalues of the full-scale isotropic conical shell for the S4R and the SC8R element models. The difference between the two elements is given between brackets.

Element type	S4R	SC8R
Force eigenvalue 1 [kN]	5332	5404 (+1.35%)
Force eigenvalue 2 [kN]	5332	5404 (+1.35%)
Force eigenvalue 3 [kN]	5333	5406 (+1.37%)
CPU time [s]	497.8	490.7 (-1.43%)
Displacement eigenvalue 1 [mm]	3.910	3.953 (+1.10%)
Displacement eigenvalue 2 [mm]	3.910	3.953 (+1.10%)
Displacement eigenvalue 3 [mm]	3.912	3.954 (+1.07%)
CPU time [s]	497.2	486.7 (-2.11%)

all degrees of freedom of the nodes and the reference points through rigid body links. This application method is chosen because it allows for easy postprocessing. The compression is applied as a concentrated force or as a displacement in the reference point connected to the small radius edge nodes. It is oriented in the axial direction. Clamped boundary conditions are used, meaning that all degrees of freedom are constraint in the reference point connected to the large radius edge nodes. The small radius reference point is constraint in all degrees of freedom, except for the axial translational direction. These are idealizations of the loading and boundary conditions in reality.

4.3.4 Sensitivity Analysis for Implicit Dynamic Analysis

When performing an implicit dynamic analysis, several parameters have to be determined. Together, they should yield a converged result. For the quasi-static application, the initial, minimum and maximum increment size must be decided, as well as the maximum total number of increments, the time period and the displacement rate. The maximum number of increments is set to 10^5. The initial and maximum increment size are set to 0.01 s and the minimum increment size is set to 10^{-7} s. The time period and displacement rate are used for the sensitivity analysis. Three different velocities are considered, namely 1, 2, and 5 mm/s. The total time period is derived from here such that a displacement of 5 mm (slightly larger than the linear displacement eigenvalue of 3.95 mm) is reached at the end of the step. The rest of the model is the same as for the linear analyses. These dynamic analyses are compared to a nonlinear static analysis, for which the model is also built up in the same way. The maximum number of increments and the minimum increment size are also set to 10^5 and 10^{-7} s, respectively. The initial and maximum increment size are set to 0.001 s. These settings are in line with the ones used by Di Pasqua et al. [46] for the analysis of a composite conical shell.

Figure 4.8 shows the load-displacement curves for all of these analyses and Table 4.9 gives the obtained buckling loads and displacements and the corresponding CPU time. The buckling load of the implicit dynamic analyses and the nonlinear static analysis show convergence. For increasing displacement in the postbuckling regime, all analyses converge to the same load value, except for the analysis with a displacement rate of 1 mm/s. The difference in results between the 2 mm/s and 1 mm/s analyses is very small, but the CPU time of the former is almost half of the latter. It is therefore decided to use the implicit dynamic analysis with a

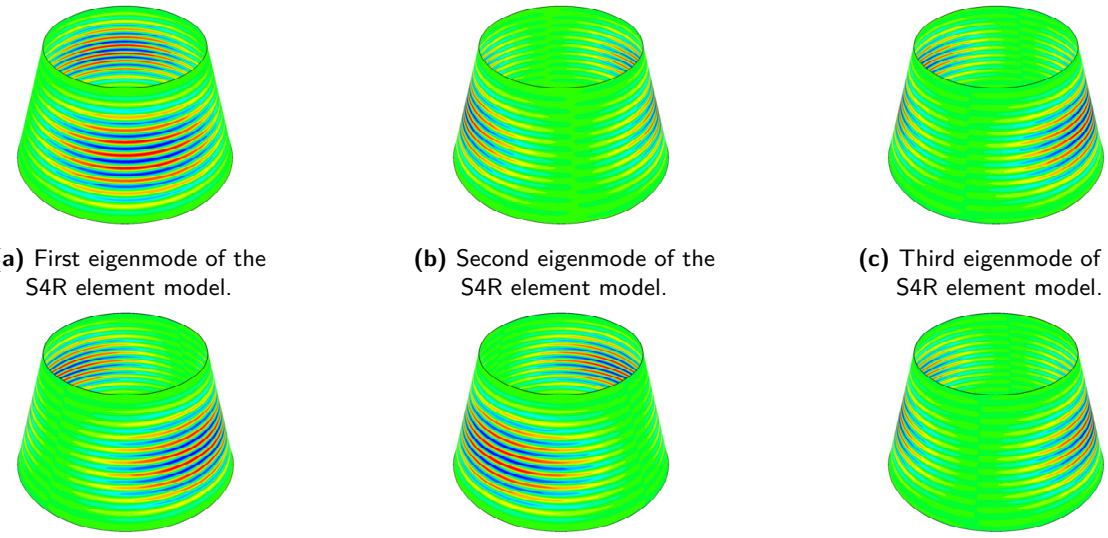

(a) First eigenmode of the S4R element model.
(b) Second eigenmode of the S4R element model.
(c) Third eigenmode of the S4R element model.
(d) First eigenmode of the SC8R element model.
(e) Second eigenmode of the SC8R element model.
(f) Third eigenmode of the SC8R element model.

Figure 4.6: Comparison of the first three eigenmodes of the full-scale isotropic conical shell for the S4R and the SC8R element models, showing radial displacement.

displacement rate of 2 mm/s for further analyses. The other settings are as described above. As a result, a minimum of 250 steps is used to complete the analysis. Additional smaller steps are taken by the solver to reach convergence if the increment size of 0.01 s is deemed too large.

Table 4.9: Comparison of nonlinear buckling load solutions for the full-scale isotropic conical shell. The difference with the nonlinear static analysis is given between brackets.

	Implicit dynamic analysis			**Nonlinear**
	5 mm/s	2 mm/s	1 mm/s	**static analysis**
Buckling load [kN]	5180 (+2.55%)	5079 (+0.554%)	5028 (-0.455%)	5051
Buckling displacement [mm]	3.826 (+2.822%)	3.745 (+0.645%)	3.705 (-0.430%)	3.721
CPU time [s]	4017.8 (-65.1%)	5794.8 (-49.6%)	10412 (-9.44%)	11497

4.4 Failure Assessment

In the derivation of the scaling methodology, it is assumed that damage does not occur prior to buckling. This assumption is checked for the evaluated conical shells. For isotropic shells, this is done by comparing the von Mises stress to the yield strength, given in Table 4.3. For composite shells, the first ply failure criteria available in Abaqus are evaluated at incipient buckling [45]. The strength and strain values of the composite material are given in Table 4.5. The failure index I_F should stay below 1 to not have failure. The following criteria are considered.

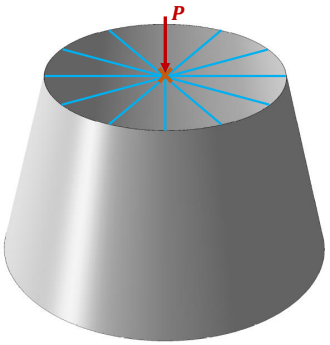

Figure 4.7: Schematic representation of the small radius reference point (orange), the tie constraints (blue) and the load application (red).

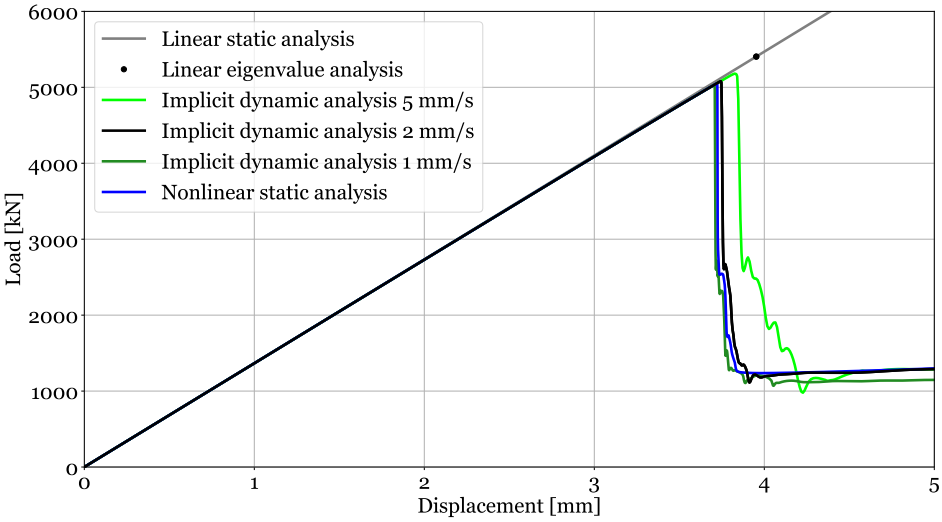

Figure 4.8: Sensitivity of the implicit dynamic analysis to displacement rate and to initial increment size for the full-scale isotropic conical shell.

- **Maximum strain criterion.** The failure index is calculated as

$$I_F = \max\left(\frac{\epsilon_{11}}{S_{11}}, \frac{\epsilon_{11}}{S_{22}}, \left|\frac{\epsilon_{12}}{S_{12}}\right|\right), \tag{4.3}$$

where $S_{11} = S_{11}^t$ if $\epsilon_{11} > 0$ and $S_{11} = S_{11}^c$ otherwise. Accordingly, $S_{22} = S_{22}^t$ if $\epsilon_{22} > 0$ and $S_{22} = S_{22}^c$ otherwise.

- **Maximum stress criterion.** The failure index is calculated as

$$I_F = \max\left(\frac{\sigma_{11}}{F_{11}}, \frac{\sigma_{11}}{F_{22}}, \left|\frac{\sigma_{12}}{F_{12}}\right|\right), \tag{4.4}$$

where $F_{11} = F_{11}^t$ if $\sigma_{11} > 0$ and $F_{11} = F_{11}^c$ otherwise. Accordingly, $F_{22} = F_{22}^t$ if $\sigma_{22} > 0$ and $F_{22} = F_{22}^c$ otherwise.

- **Tsai-Hill criterion.** The failure index is calculated as

$$I_F = \frac{\sigma_{11}^2}{F_{11}^2} - \frac{\sigma_{11}\sigma_{22}}{F_{11}^2} + \frac{\sigma_{22}^2}{F_{22}^2} + \frac{\sigma_{12}^2}{F_{12}^2}\,, \tag{4.5}$$

  where $F_{11} = F_{11}^t$ if $\sigma_{11} > 0$ and $F_{11} = F_{11}^c$ otherwise. Accordingly, $F_{22} = F_{22}^t$ if $\sigma_{22} > 0$ and $F_{22} = F_{22}^c$ otherwise.

- **Tsai-Wu criterion.** The failure index is calculated as

$$I_F = \left(\frac{1}{F_{11}^t} + \frac{1}{F_{11}^c}\right)\sigma_{11} + \left(\frac{1}{F_{22}^t} + \frac{1}{F_{22}^c}\right)\sigma_{22} - \frac{\sigma_{11}^2}{F_{11}^t F_{11}^c} - \frac{\sigma_{22}^2}{F_{22}^t F_{22}^c} + \frac{\sigma_{12}^2}{F_{12}^2}\,. \tag{4.6}$$

- **Hashin criteria.** The failure indices are calculates as follows.

  For fiber tension, if $\sigma_{11} \geq 0$,

$$I_F = \left(\frac{\sigma_{11}}{F_{11}^t}\right)^2 + \left(\frac{\sigma_{12}}{F_{12}}\right)^2\,, \tag{4.7a}$$

  or for fiber compression, if $\sigma_{11} < 0$,

$$I_F = \left(\frac{\sigma_{11}}{F_{11}^c}\right)^2\,. \tag{4.7b}$$

  For matrix tension, if $\sigma_{22} \geq 0$,

$$I_F = \left(\frac{\sigma_{22}}{F_{22}^t}\right)^2 + \left(\frac{\sigma_{12}}{F_{12}}\right)^2\,, \tag{4.7c}$$

  or for matrix compression, if $\sigma_{22} < 0$,

$$I_F = \left(\frac{\sigma_{22}}{2F_{13}}\right)^2 + \left[\left(\frac{F_{22}^c}{2F_{13}}\right)^2 - 1\right]\frac{\sigma_{22}}{F_{22}^c} + \left(\frac{\sigma_{12}}{F_{12}}\right)^2\,. \tag{4.7d}$$

The failure indices are calculated and the results are evaluated: which ply and which location on the shell are critical according to each failure criterion. In addition, the strain distribution of the critical ply according to the maximum strain criterion, is analyzed.

Finally, for sandwich conical shells, core failure due to shear crimping is evaluated. The equation presented by Bert and Reese [92] for cylindrical shells is adjusted for conical shells. This yields the shear crimping load

$$P_{\mathrm{SC}} = 2\pi R_1 \cos\alpha \frac{G_{13}\left(t_{\mathrm{facesheet}} + t_{\mathrm{core}}\right)^2}{t_{\mathrm{core}}} \tag{4.8}$$

where G_{13} is the shear modulus of the core, $t_{\mathrm{facesheet}}$ is the thickness of one facesheet and t_{core} is the core thickness. To ensure that shear crimping occurs after buckling, $P_{\mathrm{SC}} > P_{\mathrm{cr}}$.

4.5 Nondimensional Comparison

Once the analyses detailed above are performed for the full-scale and reduced-scale shell, the results should be compared. It is evaluated whether the reduced-scale shell is capable of predicting the behavior of the full-scale shell. This is checked through the nondimensional parameters linking the two shells. This section explains which parameters are compared and how this is done.

4.5.1 Scaling Parameters

First, the parameters used for scaling, given in Equation 3.72, are compared. If all parameters are used for the design of the reduced-scale shell, it is expected that these are identical. Due to the rounding of dimensions and due to conflicting parameters, differences may arise. These differences are calculated and discussed.

4.5.2 Nondimensional Load-displacement Curves

Second, the nondimensional loads and displacements are compared. This is done for the three evaluation methods, namely the semi-analytical solution, the linear eigenvalue analysis, and the implicit dynamic analysis. For the nondimensional load, use is made of Equation 3.72f. For the nondimensional displacement,

$$U = \frac{u\,L}{\sqrt{a_{11}a_{22}D_{11}D_{22}}} \tag{4.9}$$

is used, which can be found by making the strain-displacement equations nondimensional [70]. Here, u is the displacement in the meridional direction, while the displacement obtained in the finite element models is in axial direction. Therefore, a coordinate transformation should be performed from the cylindrical system in Abaqus to the curvilinear system used for the analytical work, both shown in Figure 4.9. This transformation is given by

$$\begin{Bmatrix} x \\ z \end{Bmatrix} = \begin{bmatrix} \sin\alpha & -\cos\alpha \\ \cos\alpha & \sin\alpha \end{bmatrix} \begin{Bmatrix} r_{\text{cyl}} \\ z_{\text{cyl}} \end{Bmatrix} . \tag{4.10}$$

Due to the boundary conditions, the radial displacement is zero at the edges, such that $u = -\cos\alpha\, u_3$. This can be substituted in Equation 4.9 to find the nondimensional displacement in meridional direction. Consequently, the nondimensional load-displacement curves can be drawn for the two shells and the results can be compared. In addition, the nondimensional stiffness, given by $\frac{K_{xx}}{U}$, is studied.

4.5.3 Deformation Shapes

Finally, the deformation shapes during the analyzed regime can be compared. First, the deformation shapes at several instances during the load application are visually compared. More specifically, the shapes prior to buckling, upon buckling and after buckling are compared. Although the postbuckling regime is not part of the scaling methodology, it is interesting to see if the two shells behave the same after buckling as well. In addition, the deformation shapes predicted by the semi-analytical solution and the linear eigenvalue analysis are compared.

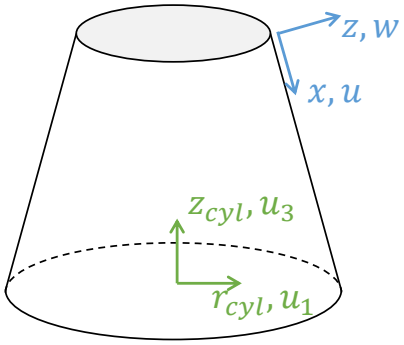

Figure 4.9: The cylindrical coordinate system in Abaqus (green) and the analytical coordinate system (blue).

Second, the postbuckling deformation shape is quantified in terms of the number of meridional half-waves m and circumferential full waves n, given by (m, n), and the (dimensional) magnitude of the radial displacement is evaluated. The latter gives an idea of the difference in size between full-scale and reduced-scale shells. The ratio of minimum to maximum radial displacement is compared for the two shells as well. Finally, the nondimensional radial displacement is also compared. This is calculated using

$$W = \frac{w}{\sqrt[4]{a_{11}a_{22}D_{11}D_{22}}}, \tag{4.11}$$

where w is the displacement in z-direction, which can be calculated using Equation 4.10 [70].

Chapter 5

Scaling of Isotropic Conical Shell

This chapter discusses the application of the scaling methodology to an isotropic conical shell. This allows to evaluate the methodology for a simplified case, which intrinsically satisfies the laminate assumptions. First, the full-scale shell is described and the reduced-scale shell is designed using the scaling methodology. Second, the two shells are analyzed. Finally, the results are compared nondimensionally.

5.1 Conical Shell Designs

This section elaborates on the designs of the isotropic full-scale and reduced-scale shells. The full-scale shell is first described, after which the reduced-scale shell is designed using the scaling methodology.

5.1.1 Full-Scale Conical Shell Description

As discussed in section 4.1, the SLS USA and PAF structures are used as full-scale reference shells. Here, the full-scale conical shell has the SLS USA geometry and is assumed to be made of aluminum 2024-T4, of which the properties are given in Table 4.3. The thickness is assumed to measure 4.5 mm. The geometry of the conical shell is described in Table 5.1.

5.1.2 Reduced-Scale Conical Shell Design

The full-scale isotropic conical shell is scaled to a smaller conical shell. The procedure described in subsection 3.6.1 is followed. First, it is decided to use the same material for the reduced-scale conical shell as for full-scale shell, namely aluminum 2024-T4, of which the properties are given in Table 4.3. Second, the cone angle α is set equal to the full-scale cone angle of 15°. Third, the large radius R_2 is set equal to 400 mm (9.52% of the full-scale large radius), which is a size compatible with many test machines as described in subsection 4.1.2. Fourth, the length and thickness are determined using Equation 3.74a and Equation 3.74c. Because the same material is used, all dimensions are scaled by the same factor, namely to 9.52% of the full-scale values. This results in the dimensions given in Table 5.1. Figure 5.1 shows the

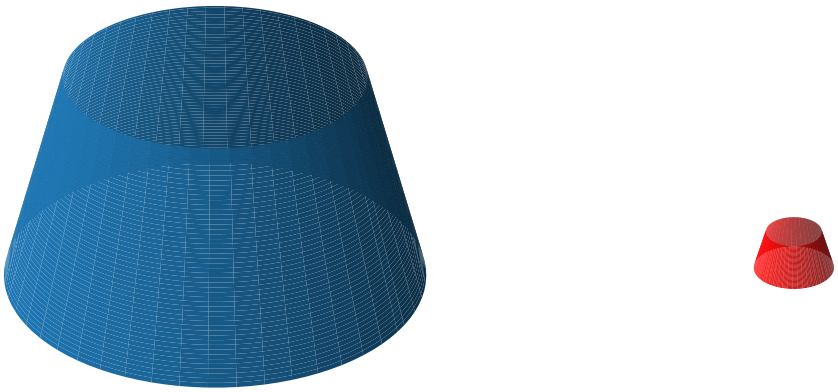

Figure 5.1: Visualization of the full-scale (blue, left) and reduced-scale (red, right) isotropic conical shells. Full-scale is 73x smaller than in reality, reduced-scale is 36x smaller than in reality.

relative size of the two shells. It should be noted that the thickness is small and that the required accuracy of 0.01 mm may both be difficult to achieve with common manufacturing equipment.

Table 5.1: Geometry descriptions of the full-scale (FS) and reduced-scale (RS) isotropic conical shells.

	Cone angle α [deg]	**Length L [mm]**	**Small radius R_1 [mm]**	**Large radius R_2 [mm]**	**Thickness t [mm]**
FS	15	4996	2910	4203	4.5
RS	15	476	277	400	0.43

5.2 Buckling Analyses

With the design of the conical shells determined, their buckling behavior is analyzed using the three methods described in section 4.2.

5.2.1 Semi-analytical Solution

As a first step, the buckling behavior of the two conical shells is analyzed using the semi-analytical solution. For both shells, the semi-analytical solution predicts a (2,14) buckling mode, which has two meridional half waves and 14 circumferential full waves. The obtained buckling loads measure 5336 kN for the full-scale shell and 48.71 kN for the reduced-scale shell.

5.2.2 Linear Eigenvalue Analysis

The two shells are modeled with a linear eigenvalue analysis in Abaqus. The modeling techniques used for the full-scale shell are explained in section 4.3. For the reduced-scale shell, the same approach is taken, but a new mesh convergence study is required. Because the shell is approximately one-tenth of the full-scale shell, the mesh sizes considered here are one tenth of the ones used for full-scale structure, namely 20 mm, 10 mm, 5 mm and 2.5 mm. The results

are very similar to the full-scale mesh convergence results and are therefore not repeated here. The mesh size of 5 mm yields converged results and is consequently used for further analyses. The other modeling techniques are identical to the ones of the full-scale conical shell.

The results of the linear eigenvalue analyses (force and displacement eigenvalues) are given in Table 5.3. The buckling modes are visualized in Figure 5.2. These are different from the modes predicted by the semi-analytical solution. It may be the case that the semi-analytical solution cannot capture this buckling mode due to the assumed shape. Another possible explanation for the difference is that the eigenvalues are very close together, such that the obtained eigenmode is affected by numerical errors and rounding. In addition, the semi-analytical solution does not impose boundary conditions on the conical shells, whereas the model for the eigenvalue analysis has clamped boundary conditions. This may increase the buckling load and change the mode.

(a) Full-scale conical shell. **(b)** Reduced-scale conical shell.

Figure 5.2: First eigenmode of the isotropic conical shells, showing radial displacement.

A linear static analysis is performed for both shells as well. This allows to compute the linear stiffness of the conical shell, which can be used to compare the linear eigenvalue analysis and the implicit dynamic analysis to. A compression load of 6000 kN is applied to the small radius reference point for the full-scale shell. For the reduced-scale shell, a load of 60 kN is applied.

5.2.3 Implicit Dynamic Analysis

Next, an implicit dynamic analysis is performed. The details of the analysis are discussed in chapter 4 for the full-scale shell. For the reduced-scale shell, the same sensitivity analysis is performed, but with displacement rates equal to one-tenth of the displacement rates used for the full-scale shell. More specifically, velocities of 0.5 mm/s, 0.2 mm/s and 0.1 mm/s are investigated. The desired final displacement is 0.5 mm, which is slightly larger than the linear buckling displacement of 0.385 mm. These rates and this final displacement are chosen such that the minimum total number of increments required per analysis is identical to the minimum total number of increments per analysis of the full-scale shell (i.e. 250 increments). It is assumed that all other modeling parameters can be kept the same as for the full-scale conical shell.

The results of the sensitivity analysis are visualized in Figure 5.3 and the buckling loads, buckling displacements and CPU time are reported in Table 5.2. The implicit dynamic analyses of 0.2 and 0.1 mm/s show strong nonlinearity prior to buckling, such that the buckling displacement predicted by these analyses is larger than the linear buckling displacement. This phenomenon is commonly referred to as a load plateau and is caused by extremely stable behavior originating from the numerically idealized geometry [93]. As a result, the numerical shell model shows an axisymmetric deformation pattern, visualized in Figure 5.4, in which

the radial displacement continues to increase and remain stable. This is not realistic, because there are always imperfections present in the real structure. Therefore, a small imperfection is added to avoid this numerical error. More specifically, an imperfection in the shape of the first eigenmode is introduced with an amplitude of 1% of the thickness. This is done using the **IMPERFECTION* keyword in Abaqus [35,45]. It is decided to use the implicit dynamic analysis of 0.2 mm/s, because it shows convergence with respect to the 0.1 mm/s analysis.

Table 5.2: Comparison of nonlinear buckling load solutions for the reduced-scale isotropic conical shell. The difference with the nonlinear static analysis is given between brackets.

	Implicit dynamic analysis			**Nonlinear static analysis**
	0.5 mm/s	0.2 mm/s	0.1 mm/s	
Buckling load [kN]	50.82 (+3.65%)	51.03 (+4.08%)	51.03 (+4.08%)	49.03
Buckling displacement [mm]	0.391 (+5.02%)	0.403 (+8.19%)	0.402 (+8.00%)	0.372
CPU time [s]	4668 (-53.7%)	8996 (-10.7%)	9375 (-6.98%)	10078

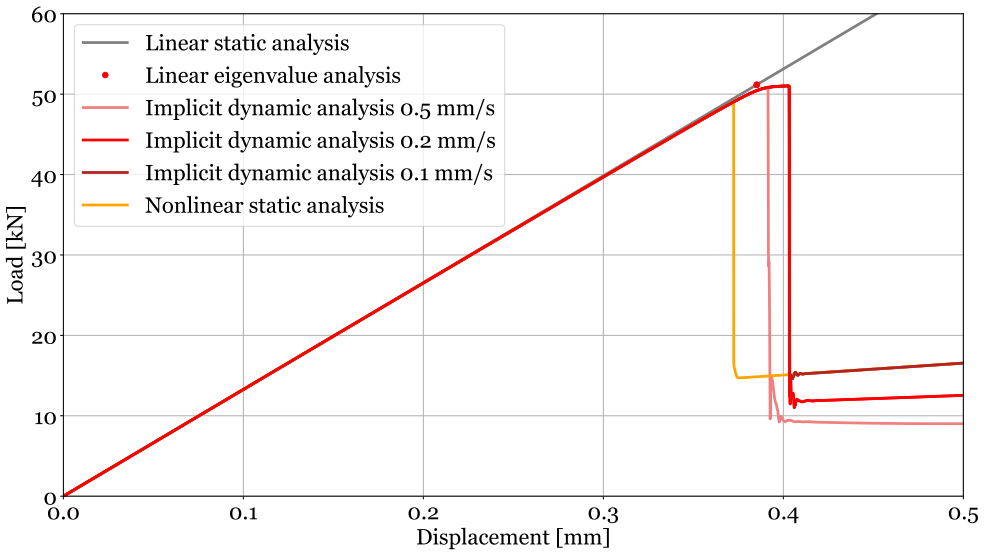

Figure 5.3: Sensitivity of the implicit dynamic analysis to displacement rate for the reduced-scale isotropic conical shell.

Because the eigenmode imperfection is applied to the reduced-scale shell, it is also applied to the full-scale shell to be able to compare the two shells. The results of the imperfect shells are summarized in Table 5.3. The load-displacement curves of the imperfect shells are compared to the ones of the imperfection-free shells in Figure 5.5. As expected, the load plateau does not occur. The stiffness is similar for the imperfection-free and imperfect case for the full-scale shell. For the reduced-scale shell, the stiffness is also similar up to the initiation of the load plateau. The reduction in buckling load is large for both shells. To quantify this, the knockdown factor is calculated as

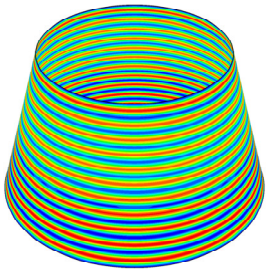

Figure 5.4: Stable axisymmetric deformation shape prior to buckling due to the idealized, imperfection-free geometry.

$$\mathrm{KDF} = \frac{P_{\mathrm{cr,imperfect}}}{P_{\mathrm{cr,linear}}}\,. \tag{5.1}$$

For both shells, the knockdown factor equals 0.88. This is already a large reduction for an imperfection with an amplitude of only 1% of the thickness. This is in agreement with results from literature on conical and cylindrical shells. Typically, the reduction in buckling load is very large for small imperfections, but becomes more gradual for larger imperfections [6, 94].

Table 5.3: Buckling load and displacement for the isotropic conical shells.

		Buckling load P_{cr} [kN]	**Buckling displ. u_{cr} [mm]**
Semi-analytical solution	FS	5336	n.a.
	RS	48.71	n.a.
Eigenvalue analysis	FS	5404	3.95
	RS	51.17	0.385
Implicit dynamic analysis	FS	4766	3.52
	RS	45.03	0.342

Table 5.3 summarizes the results of the performed analyses for the two isotropic shells, which are also visualized in Figure 5.5. For both shells, the linear analysis and the implicit dynamic analyses predict approximately the same stiffness, indicating a good correlation between all analyses. Prebuckling nonlinearity is present, but limited for both shells. The semi-analytical solution assumes a membrane prebuckling solution, such that the nonlinearity introduced by the boundary conditions is not taken into account. The difference in results between the linear eigenvalue and the implicit dynamic analyses is mainly caused by the applied imperfection.

The scaling methodology assumes that the shells are elastic, meaning that they cannot undergo plastic deformation. It is therefore checked by comparing the von Mises stress at incipient buckling to the yield strength, reported in Table 4.3. Right before buckling, the stress in the imperfect full-scale conical shell never exceeds 79.5 MPa. The von Mises stress in the reduced-scale shell reaches a maximum of 80.4 MPa prior to buckling. These values are well below the yield strength of 324 MPa, thus ensuring that the shell will buckle before undergoing plasticity.

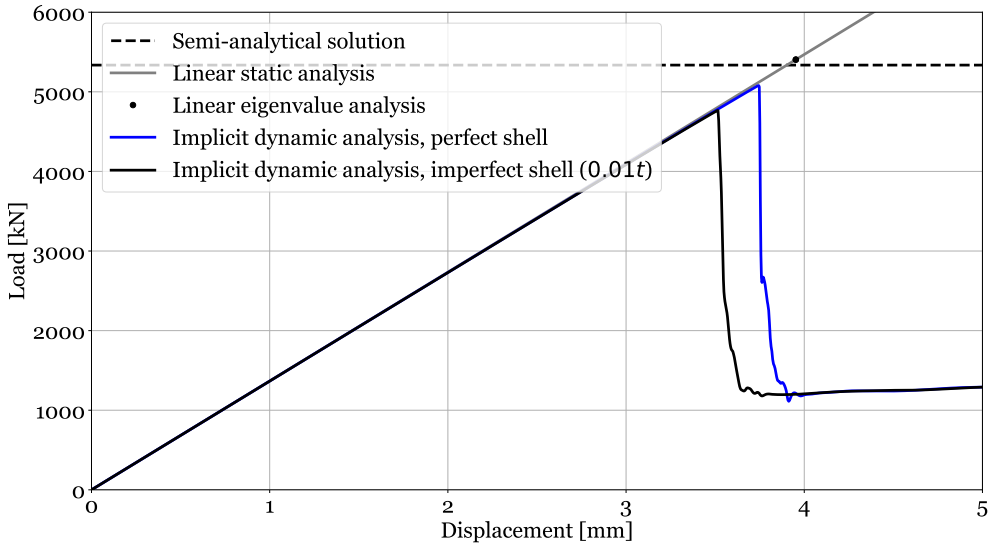

(a) Full-scale conical shell.

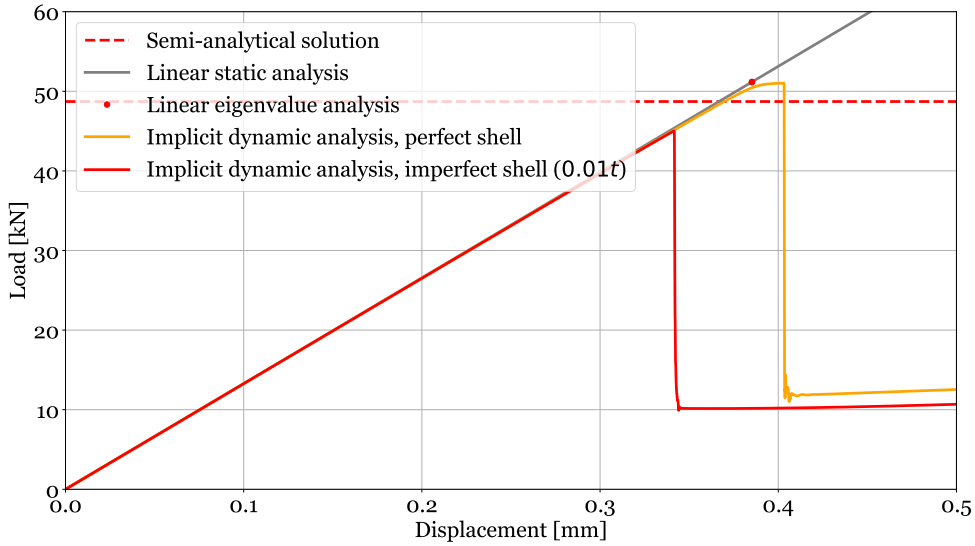

(b) Reduced-scale conical shell.

Figure 5.5: Load-displacement curves of the imperfection-free and imperfect isotropic conical shells.

5.3 Comparison of the Full-Scale and Reduced-Scale Conical Shells

Finally, the full-scale and reduced-scale conical shell can be compared to assess the accuracy of the scaling methodology for this isotropic conical shell. First, the nondimensional parameters are compared. Second, the nondimensional buckling loads and the load-displacement curves are evaluated. For the nonlinear comparison, the results of the imperfect shells are compared. Third, the deformation shapes are compared.

5.3.1 Scaling Parameters

The nondimensional scaling parameters are compared in Table 5.4, where slight differences are observed. The largest difference measures 0.373% and occurs for the Batdorf-Stein-equivalent parameter at the small radius end. These small differences are caused by the rounding of the dimensions of the reduced-scale conical shells to a manufacturable accuracy.

Table 5.4: The nondimensional scaling parameters of the full-scale and reduced scale isotropic conical shells.

	Membrane-bending parameter α_{mb}		**Batdorf-Stein equivalent parameter Z_2**		**Membrane orthotropy parameter μ**	**Flexural orthotropy parameter β**
	$z_1 = 0$	$z_1 = 1$	$z_1 = 0$	$z_1 = 1$	$z_1 \epsilon [0, 1]$	$z \epsilon [0, 1]$
FS	0.5824	0.8413	589.6	851.7	1	1
RS	0.5819	0.8403	587.4	848.6	1	1
Δ	(-0.0859%)	(-0.119%)	(-0.373%)	(-0.364%)	(0.0%)	(0.0%)

5.3.2 Nondimensional Load-Displacement Curves

Next, the nondimensional load-displacement curve is compared, as shown in Figure 5.6. For simplicity, only the nondimensional loads K_{xx} calculated using the equation for $z_1 = 0$ are visualized in the figure. The nondimensional buckling load and displacement for the full-scale and reduced-scale shells are also given in Table 5.5 for the three analyses.

The difference in accuracy between the prediction at $z_1 = 0$ and at $z_1 = 1$ is negligible. This makes sense, because the scaling parameters at both meridional locations are satisfied. The semi-analytical nondimensional load is nearly identical for the two shells. The small difference is caused by the rounding of the dimensions of the reduced-scale shell. The prediction accuracies obtained with the eigenvalue analysis and the nonlinear analysis are very close together, indicating little influence from nonlinearity and imperfections on the methodology. Indeed, the effect of the 1% eigenmode imperfection is identical for the two shells in terms of the knockdown factor, which measures KDF=0.88 for both shells. The discrepancies between full-scale and reduced-scale shells may be caused by slight differences in the numerical models. The nondimensional stiffness is predicted accurately, with a maximum difference of 1.73%. In the postbuckling regime, the load-displacement curves of the two shells converge to a different nondimensional load value. This does not come as a surprise, because the postbuckling equations are not taken into account in the scaling methodology.

5.3.3 Deformation Shapes

The buckling mode predictions of the semi-analytical solution are identical, namely a (2,14) mode. The linear eigenvalue analyses predict similar modes, see Figure 5.2. Figure 5.7 and Figure 5.8 display the nonlinear deformation shapes of the two conical shells at various points throughout loading. The displayed shapes correspond to the blue crosses in Figure 5.6. The deformation shapes look similar for the two shells. Prior to buckling, the linear eigenmode can easily be recognized. Upon buckling, the deformation shapes are slightly different. This is in line with the load-displacement graphs, which are not coincident here. After buckling, the

Table 5.5: Comparison of nondimensional buckling load, displacement and stiffness for the isotropic conical shells.

		Buckling load K_{xx}		**Buckling displ.** U	**Stiffness** K_{xx}/U	
		$z_1 = 0$	$z_1 = 1$	$z_1 \epsilon [0, 1]$	$z_1 = 0$	$z_1 = 1$
Semi-	FS	4106.9	5931.9	n.a.	n.a.	n.a.
analytical	RS	4090.7	5910.1	n.a.	n.a.	n.a.
solution	Δ	(-0.394%)	(-0.368%)			
Eigenvalue	FS	4160	6008	10073	0.4130	0.5964
analysis	RS	4296	6207	10243	0.4194	0.6060
	Δ	(+3.27%)	(+3.32%)	(+1.69%)	(+1.55%)	(+1.61%)
Implicit	FS	3668	5298	8960	0.4094	0.5913
dynamic	RS	3781	5463	9082	0.4163	0.6015
analysis	Δ	(+3.08%)	(+3.11%)	(+1.36%)	(+1.69%)	(+1.73%)

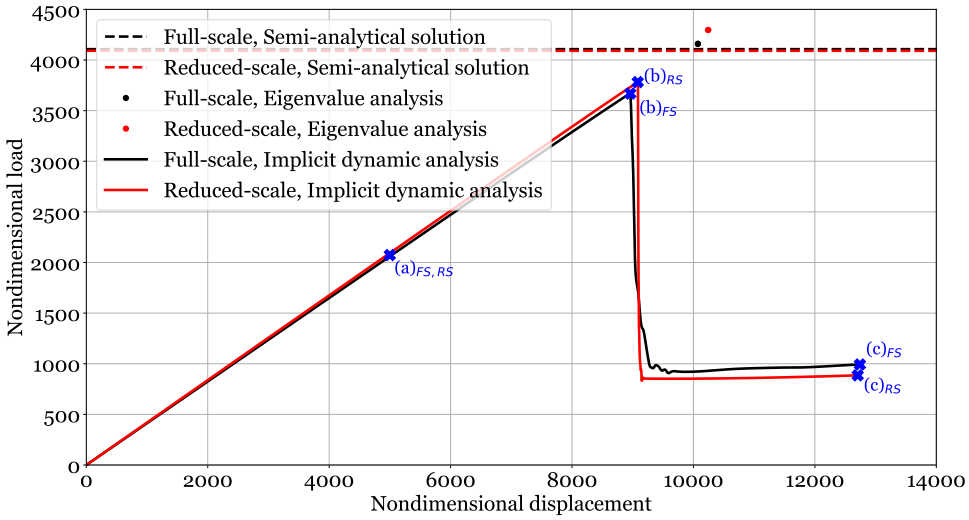

Figure 5.6: Nondimensional load-displacement curve of the (imperfect) isotropic conical shells, using K_{xx} at $z_1 = 0$..

deformation shapes are similar, but not identical. The full-scale shell has a (2,14) deformation shape, whereas the reduced-scale shell has a (2,13) pattern. This can also be seen in the load-displacement graph, because the two shells converge to a different load. In addition, the waves of the full-scale shell are positioned a bit lower than the ones of the reduced-scale shell. This difference may be caused by the discrete increment steps taken in the finite element analysis, such that the nondimensional displacement is slightly different for the two shells.

Figure 5.9 shows the dimensional postbuckling deformation shapes. The radial displacement is also scaled by more or less a factor 10. The ratio of maximum to minimum radial displacement equals -0.459 and -0.463 for full-scale and reduced-scale shells. This is within 1% of each other. The scalability of the radial displacement is analyzed by evaluating its nondimensional form. The minimum and maximum values are compared in Table 5.6. Larger differences

are observed than for the load-displacement graphs, but the results are in the same order of magnitude. For the equations used for the scaling methodology, a membrane prebuckling shape is assumed and the presence of imperfections is not taken into account. This has an effect on the radial displacement of the two shells, thus creating the difference.

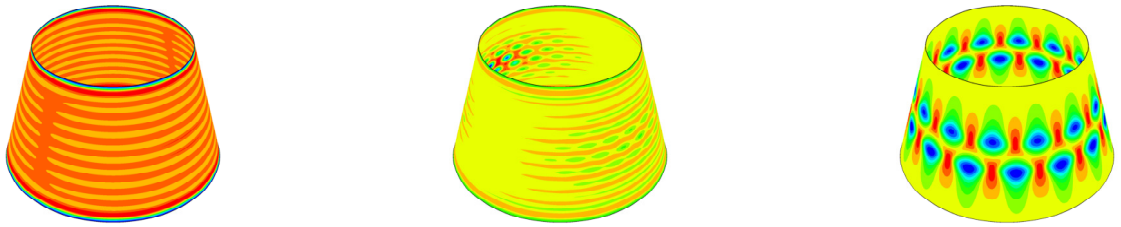

(a) Before buckling, for $U = 5000$.

(b) At buckling, for $U = 8960$.

(c) After buckling, for $U = 12742$.

Figure 5.7: Deformation shapes (radial displacement) of the imperfect full-scale isotropic conical shell at the points indicated in Figure 5.6.

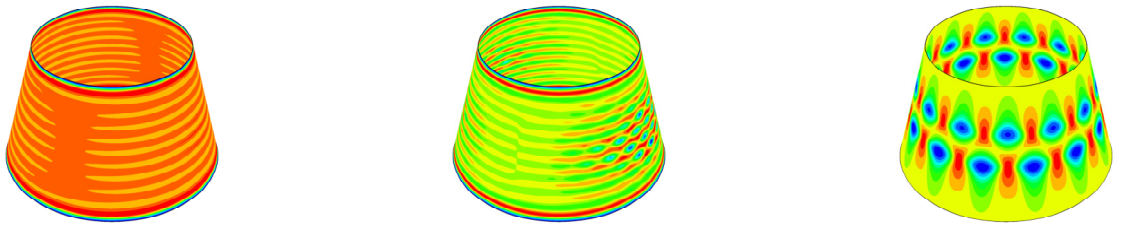

(a) Before buckling, for $U = 5000$.

(b) At buckling, for $U = 9082$.

(c) After buckling, for $U = 12758$.

Figure 5.8: Deformation shapes (radial displacement) of the imperfect reduced-scale isotropic conical shell at the points indicated in Figure 5.6.

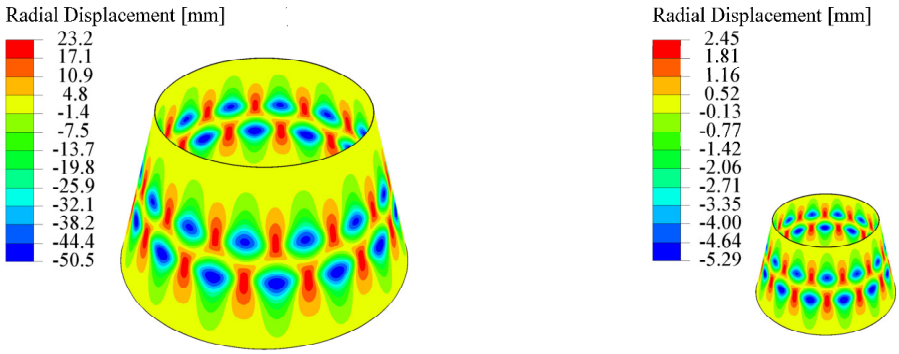

(a) Full-scale conical shell.

(b) Reduced-scale conical shell.

Figure 5.9: Comparison of the dimensional postbuckling deformation shape. Reduced-scale shell is 5x enlarged compared to the full-scale shell for visibility.

Table 5.6: Comparison of the minimum and maximum nondimensional radial displacement for the isotropic conical shells.

	Minimum radial displacement $W_{\min}$	**Maximum radial displacement $W_{\max}$**	**Ratio $W_{\max}/W_{\min}$**
FS	-38.2	17.3	-0.453
RS	-41.8	19.1	-0.457
Δ	(+9.42%)	(+10.4%)	(+0.883%)

5.4 Concluding Remarks

This chapter covers the application of the scaling methodology to an isotropic conical shell. The prediction accuracy of the reduced-scale conical shell was good: the nonlinear buckling load and displacement of the full-scale shell were overestimated by 3.08% and 1.36%. These results are satisfactory, especially because an imperfection was applied and it did not cause the methodology to fail. More specifically, a knockdown factor of KDF=0.88 was found for both shells. At the same time, the imperfection has an amplitude of only 1% of the thickness and is of similar shape for the two shells, so it cannot be concluded that the methodology is robust against all kinds of imperfections. This could be investigated further through the application of different and larger imperfections, for example, the inclusion of measured imperfections.

The deformation shapes are accurately predicted, especially up to buckling. In the postbuckling regime, the two load-displacement graphs converge to a different nondimensional load. The postbuckling deformation shapes are slightly different: a (2,14) shape for the full-scale shell and a (2,13) shape for the reduced-scale shell. The postbuckling behavior is not taken into account in the methodology, so this result is not surprising. The nondimensional radial displacement was in the same order of magnitude for the two shells, but differences of up to 10.4% were observed. This shows that this parameter is more difficult to predict than the buckling load and displacement. This was explained by the membrane assumption made in the methodology and the presence of the imperfection.

Overall, it can be concluded that the application of the scaling methodology to the isotropic conical shell was successful. It should be noted, however, that this result cannot be extracted to all isotropic conical shells. It was for example assumed that the curvatures are mildly varying. This assumption may not be valid for conical shells with larger cone angles. In addition, the manufacturability should be kept in mind. The thickness of the reduced-scale conical shell is small, which may complicate the production of this shell.

Chapter 6

Scaling of Cross-Ply Composite Conical Shells

In the previous chapter, the scaling methodology was successfully tested for isotropic conical shells. The methodology is now applied to a composite conical shell which satisfies the laminate assumptions. In addition, scaling is done in a way such that all scaling parameters are satisfied. More specifically, this means that a cross-ply layup is applied in combination with ply-level scaling. The chapter is built up in the same way as for the isotropic shells.

6.1 Conical Shell Designs

The designs of the full-scale and reduced-scale cross-ply shells are discussed here.

6.1.1 Full-Scale Conical Shell Description

Similar to the isotropic shell scaling, the full-scale conical shell considered here is based on the SLS USA. Again, the dimensions are the same as the original structure, but the material and stacking sequence are changed. More specifically, the full-scale conical shell is assumed to be made of IM7/8552 carbon fiber, of which the properties are listed in Table 4.4 and Table 4.5. The stacking sequence is decided to be $[0_2/90_2]_{3S}$. This stacking sequence is opted for because it allows for ply-level scaling (see Figure 2.6 and subsection 3.6.2) and because it is symmetric, balanced and has zero flexural anisotropy, satisfying all laminate requirements. The geometry is summarized in Table 6.1.

6.1.2 Reduced-Scale Conical Shell Design

The full-scale cross-ply composite conical shell is scaled to a smaller conical shell. The procedure described in subsection 3.6.2 is followed and ply-level scaling is used. First, it is decided to use the same material for the reduced-scale conical shell as for full-scale conical shell, namely IM7/8552 carbon fiber. Second, the layup is determined. The full-scale conical shell has a layup in which there are always two plies of the same angle next to each other. By

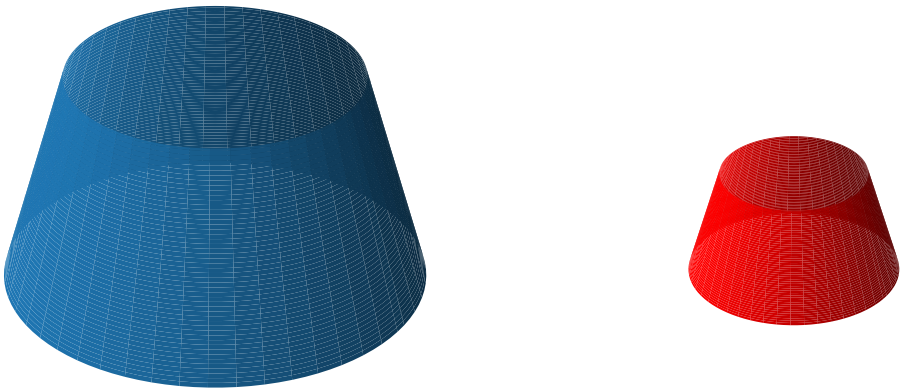

Figure 6.1: Visualization of the full-scale (blue, left) and reduced-scale (red, right) cross-ply composite conical shells. Both shells are 73x smaller than in reality.

applying ply-level scaling, the same layup structure is used but with only one ply of the same angle every time. As a result the layup becomes $[0/90]_{3S}$. Note how this is equivalent to reducing the thickness of each ply by a half. Third, the radius-to-length ratio is determined using Equation 3.72a and Equation 3.72b at $z_1 = 0$. They both yield a radius-to-length ratio of 0.5825. Using the same equations but for $z_1 = 1$, the cone angle is found to equal 15°, identical to the full-scale cone angle. Finally, the radius and length are determined using Equation 3.72e, resulting in a top radius of 1.455 m and a meridional length of 2.498 m. The obtained radius and length satisfy the radius-to-length ratio requirement from step 3. These results are summarized in Table 6.1. As explained in subsection 3.6.2, the dimensions are scaled by the same factor as the thickness, so in this case by a factor 2. This limits the usefulness of ply-level scaling, because the reduced-scale shell size remains large. In addition, stacking sequences in which many plies with the same orientation are placed next to each other are rarely used in reality to avoid rapid damage propagation. The structures are visualized in Figure 6.1.

Table 6.1: Geometry description of the full-scale (FS) and reduced-scale (RS) cross-ply composite conical shell.

	Cone angle α [deg]	**Length L [mm]**	**Small radius R_1 [mm]**	**Large radius R_2 [mm]**	**Stacking sequence [deg]**
FS	15	4996	2910	4203	$[0_2/90_2]_{3S}$
RS	15	2498	1455	2102	$[0/90]_{3S}$

6.2 Buckling Analyses

The buckling behavior of the full-scale and reduced-scale conical shells is analyzed using the three methods described in section 4.2.

6.2.1 Semi-analytical Solution

The buckling load of the two shells is estimated using the semi-analytical solution. The results are summarized in Table 6.2. For both shells, a (8,21) buckling mode is predicted.

6.2.2 Linear Eigenvalue Analysis

Next, linear eigenvalue analyses are performed. As the full-scale structure size is identical to the full-scale isotropic shell, the same mesh of 50 mm is used. The other analysis settings are also identical. For the reduced-scale shell, a mesh convergence check is performed. The mesh sizes considered for the check are half the size of the mesh sizes of the full-scale study: 100 mm, 50 mm, 25 mm and 12.5 mm. The other modeling techniques are kept the same as for the isotropic shells. The convergence results are very similar. Mesh convergence is obtained for the mesh size of 25 mm, which will consequently be used. The results can be found in Table 6.2. The semi-analytical solution and the linear eigenvalue are only 1.01% and 1.90% apart for full-scale and reduced-scale shell, respectively. This indicates good correlation between the two solutions. The semi-analytical prediction is lower than the linear eigenvalue analysis, which may be caused by the difference in boundary conditions. The finite element model has clamped boundary conditions, whereas semi-analytical solution does not impose any condition on the boundary. The linear eigenmodes are shown in Figure 6.2 and are similar, but the full-scale deformation shape is more skewed than the reduced-scale shape.

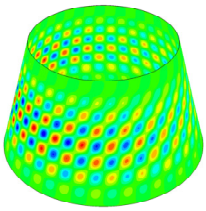

(a) Full-scale conical shell.

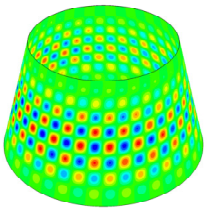

(b) Reduced-scale conical shell.

Figure 6.2: First eigenmode of the cross-ply composite conical shells, showing radial displacement.

6.2.3 Implicit Dynamic Analysis

Next, the implicit dynamic analysis is carried out to capture the nonlinear behavior and the postbuckling regime. For the isotropic conical shell, the displacement rate, time period and initial increment size were set such that $250+x$ steps were used to complete the analysis,where the extra steps x are due to increment cutbacks due to buckling. For the analysis of the cross-ply composite shells, it is aimed to have approximately the same number of steps. Therefore, the time period and the initial increment size are kept at 2.5 s and 0.01 s. For the full-scale shell, the linear buckling displacement was found to be 1.34 mm, so the implicit dynamic analysis is set such that 1.7 mm is reached at the end of the time period. Thus, the displacement rate is set to 0.68 mm/s. The other analysis settings are the same as for the isotropic conical shell. Following the same reasoning, a displacement rate of 0.34 mm/s is used for the reduced-scale shell.

The load-displacement curves of the implicit dynamic analysis are visualized in Figure 6.3. For both shells, the stiffness is very similar to the linear stiffness. The nonlinear buckling load is larger than the linear prediction for both shells, which can also be seen in Table 6.2. This is unexpected and therefore, additional analyses are run with a displacement rate half of the original ones for a period of 5 s (so $500+x$ steps). For both shells, the buckling load and displacement are within 1% of the original values and are consequently considered converged.

The difference with the linear result may be caused by a stiffening effect of the nonlinear prebuckling deformation. The buckling values are given in Table 6.2. Note how the buckling displacements of full-scale and reduced-scale shells differ by approximately a factor 2, like the geometry, and how the buckling loads differ by approximately a factor 4.

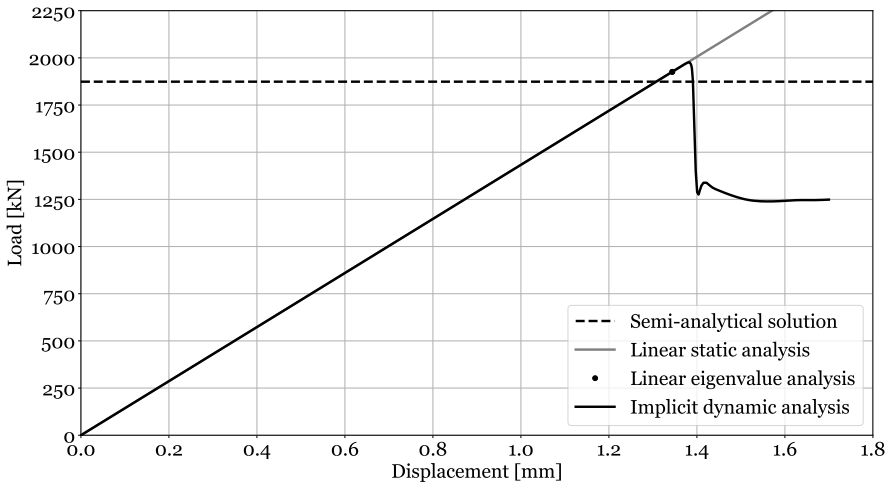

(a) Full-scale conical shell.

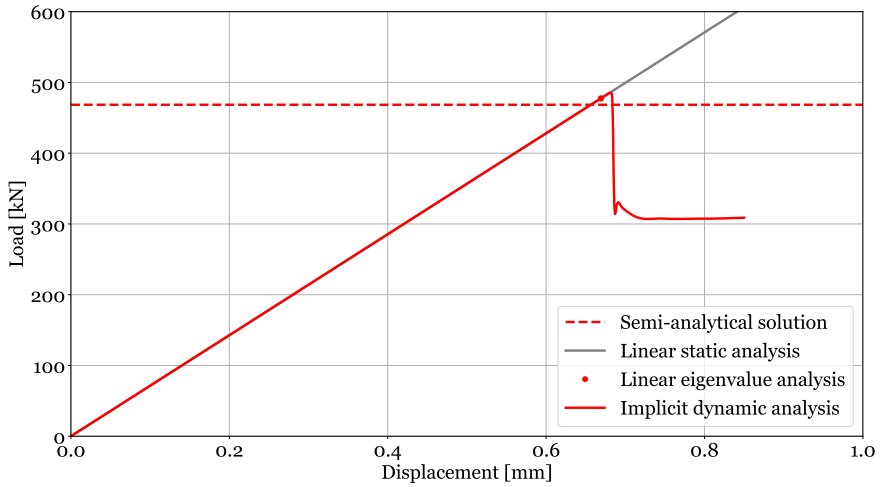

(b) Reduced-scale conical shell.

Figure 6.3: Load-displacement curves of the cross-ply composite conical shells.

6.3 Failure Assessment

Next, it is checked if failure occurs after buckling. The failure indices at incipient buckling are all well below 1, as can be seen in Table 6.3. Failure is therefore not expected prior to buckling. According to the Hashin criteria, the indices for both fiber and matrix damage are smaller than 0.01 in all plies of both shells and are therefore not reported. For the reduced-scale shell, the critical ply is the innermost ply (i.e. ply 1), which is a 0° ply. For the full-scale

Table 6.2: Buckling load and displacement for the cross-ply composite conical shells.

		Buckling load P_{cr} [kN]	**Buckling displ. u_{cr} [mm]**
Semi-analytical solution	FS	1874	n.a.
	RS	468.5	n.a.
Eigenvalue analysis	FS	1926	1.34
	RS	477.4	0.669
Implicit dynamic analysis	FS	1977	1.38
	RS	485.7	0.681

shell, the different criteria predict a different critical ply, namely the innermost and outermost plies (i.e. ply 1 and 24), both 0° plies. The maximum failure index in the other, noncritical ply is always within 3% of the one in the critical ply. The first and last ply are furthest away from the mid-surface, such that they experience the most bending strain. It is therefore not surprising that these are the critical plies. The critical location is identical for all indices and for the two shells and occurs close to the top edge, but not at it, as indicated in Figure 6.4. This is in line with the expectations. Typically, reinforcements in the form of extra plies are added close to the boundaries to avoid preliminary failure in this region.

The strains in the inner and outer plies are given in Table 6.4. The critical ones, yielding to the maximum failure index, are indicated in bold face. It can be seen that the strains in the full-scale and reduced-scale shells are similar, but slightly larger for the full-scale shell. Both analyzed plies have 0° orientation. As a result of the axial compression, the strain in fiber direction ϵ_{11}, aligned with the meridional direction, is negative and the strain in transverse direction ϵ_{22}, aligned with the circumferential coordinate, is positive.

Table 6.3: Maximum failure indices at incipient buckling for the cross-ply composite conical shells.

Failure criteria	FS	RS
Max strain	0.029 (ply 1, 0°)	0.028 (ply 1, 0°)
Max stress	0.029 (ply 24, 0°)	0.028 (ply 1, 0°)
Tsai-Hill	0.029 (ply 24, 0°)	0.028 (ply 1, 0°)
Tsai-Wu	0.024 (ply 1, 0°)	0.023 (ply 1, 0°)
Hashin	<0.01	<0.01

Table 6.4: Maximum strain values at incipient buckling in the inner and outer plies for the cross-ply composite conical shells.

	FS			RS		
	ϵ_{11} $[\mu\epsilon]$	ϵ_{22} $[\mu\epsilon]$	ϵ_{12} $[\mu\epsilon]$	ϵ_{11} $[\mu\epsilon]$	ϵ_{22} $[\mu\epsilon]$	ϵ_{12} $[\mu\epsilon]$
Inner ply (0°)	**-330.7**	43.5	180.5	**-323.5**	31.3	114.9
Outer ply (0°)	-330.5	53.4	47.5	-318.0	38.3	33.1

6.4 Comparison of the Full-Scale and Reduced-Scale Conical Shells

With the analyses performed, the full-scale and reduced-scale shells can be compared nondimensionally to evaluate the scaling methodology.

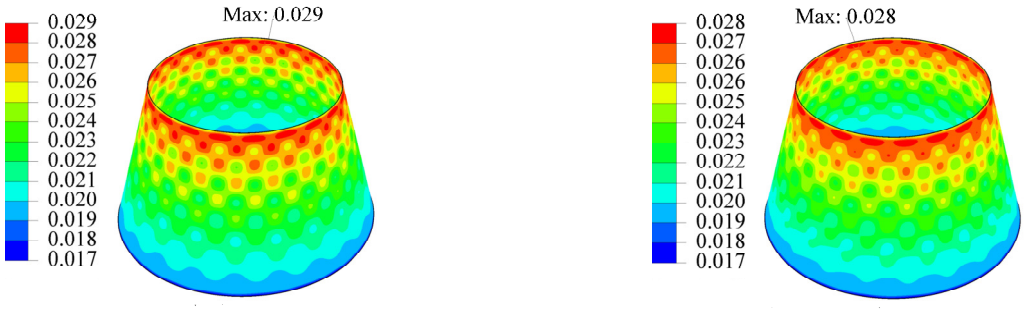

(a) Full-scale conical shell.

(b) Reduced-scale conical shell.

Figure 6.4: Maximum strain criterion plot of ply 1 (0°) of the cross-ply composite conical shells.

6.4.1 Scaling Parameters

The nondimensional parameters are reported in Table 6.5. All the values agree perfectly, in line with the expectation for ply-level scaling. The rounding of the dimensions does not affect the accuracy in this case.

Table 6.5: The nondimensional scaling parameters of the full-scale and reduced scale cross-ply composite conical shells.

	Membrane parameter α_m		**Bending parameter α_b**		**Batdorf-Stein equivalent parameter Z_2**		**Membrane orthotropy parameter μ**	**Flexural orthotropy parameter β**
	$z_1 = 0$	$z_1 = 1$	$z_1 = 0$	$z_1 = 1$	$z_1 = 0$	$z_1 = 1$	$z_1 \epsilon [0, 1]$	$z \epsilon [0, 1]$
FS	0.5825	0.8413	0.6516	0.9411	658.2	950.7	7.505	0.1790
RS	0.5825	0.8413	0.6516	0.9411	658.2	950.7	7.505	0.1790
Δ	(0.0%)	(0.0%)	(0.0%)	(0.0%)	(0.0%)	(0.0%)	(0.0%)	(0.0%)

6.4.2 Nondimensional Load-Displacement Curves

Next, the nondimensional load-displacement curves are compared, shown in Figure 6.5. The nondimensional load, displacement and stiffness are summarized per analysis in Table 6.6. The buckling load according to the semi-analytical solution match perfectly. The results of the eigenvalue analyses are also excellent, with differences below 1%. The implicit dynamic analysis results are also very good. The largest discrepancy occurs for the buckling load and measures 1.73%. The nondimensional stiffness is predicted very well. These differences may be caused by assumptions made in the scaling methodology, such as the membrane prebuckling shape, but also from discrepancies in the finite element models. The load-displacement curves have a similar shape and also converge to the same postbuckling load. The initial postbuckling path is slightly different due to the different buckling load. Recall from the dimensional analysis in section 6.2 that the buckling load is scaled by a factor 4. Looking at Equation 3.72f, this makes sense. In the numerator of the loading parameter there is the radius, which is scaled by a factor 2. In the denominator, the square root of two flexural stiffnesses is taken. These are both scaled by a factor 2^3, as a result of the cubic thickness dependency. Consequently, the load is multiplied with a factor $\frac{2}{\sqrt{2^3 . 2^3}} = \frac{1}{4}$.

Table 6.6: Comparison of nondimensional buckling load, displacement and stiffness for the cross-ply composite conical shells.

		Buckling load K_{xx}		**Buckling displ. U**	**Stiffness K_{xx}/U**	
		$z_1 = 0$	$z_1 = 1$	$z_1 \epsilon [0, 1]$	$z_1 = 0$	$z_1 = 1$
Semi-analytical solution	FS	1708	2466	n.a.	n.a.	n.a.
	RS	1708	2466	n.a.	n.a.	n.a.
	Δ	(0.0%)	(0.0%)			
Eigenvalue analysis	FS	1755	2535	4268	0.4111	0.5940
	RS	1740	2513	4251	0.4093	0.5912
	Δ	(−0.849%)	(−0.868%)	(−0.402%)	(−0.443%)	(−0.451%)
Implicit dynamic analysis	FS	1801	2602	4389	0.4103	0.5928
	RS	1770	2557	4327	0.4091	0.5909
	Δ	(-1.72%)	(-1.73%)	(-1.40%)	(-0.340%)	(-0.325%)

6.4.3 Deformation Shapes

For the semi-analytical solution, the buckling mode was predicted to be (8,21) for both conical shells. The linear buckling modes, shown in Figure 6.2, are also very similar, except that the full-scale deformation pattern is more skewed. The nonlinear deformation shapes at three instances are compared in Figure 6.6 and Figure 6.7. Prior to buckling, the resemblance is excellent. Upon buckling, the deformation of full-scale and reduced-scale shells are similar, but not identical. This deformation shape is similar to the predictions by the semi-analytical solution and the linear eigenvalue analysis. After buckling, the deformations are nearly identical as well. Both shells have a (3,20) deformation shape. The magnitude of the radial displacement is shown in Figure 6.8. In line with the geometry and axial displacement, the radial displacement is approximately scaled by a factor 2. The ratio of maximum to minimum radial displacement equals -0.478 and -0.479 for full-scale and reduced-scale shell. The scalability of the radial displacement is analyzed by evaluating its nondimensional form. The minimum and maximum values are compared in Table 6.7. The results are excellent, they match perfectly.

Table 6.7: Comparison of the minimum and maximum nondimensional radial displacement for the cross-ply composite conical shells.

	Minimum radial displacement $W_{\min}$	**Maximum radial displacement $W_{\max}$**	**Ratio $W_{\max}/W_{\min}$**
FS	-17.1	8.08	-0.473
RS	-17.1	8.09	-0.473
Δ	(0.0%)	(+0.124%)	(0.0%)

6.5 Effect of Large Cone Angle

During the derivation of the compatibility equation, it was assumed that the curvature is mildly varying with the shell coordinates. For small cone angles, this assumption is expected to hold, because the radius of the conical shell varies with $\sin\alpha$, which is small for small α.

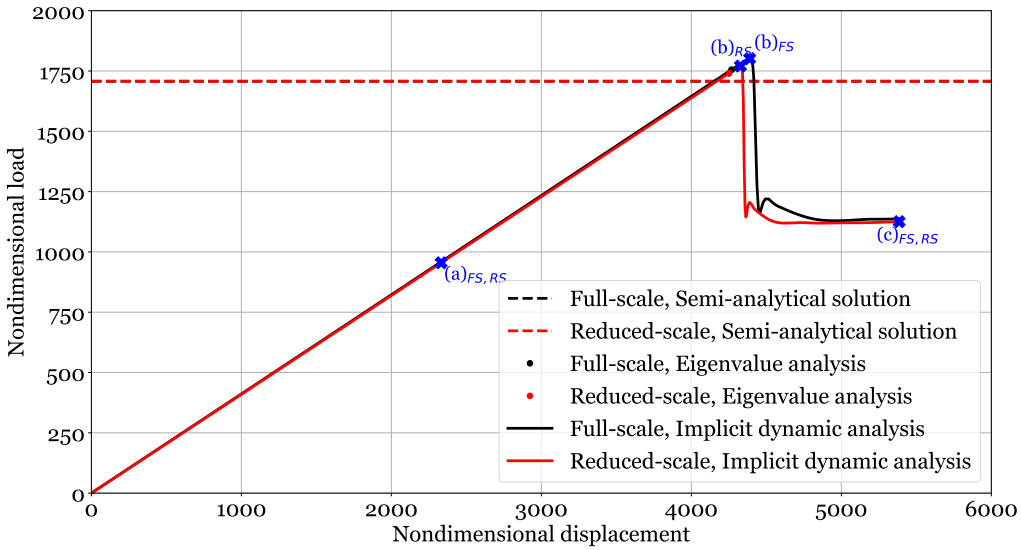

Figure 6.5: Nondimensional load-displacement curve of the full- and reduced-scale cross-ply composite conical shells, using K_{xx} at $z_1 = 0$.

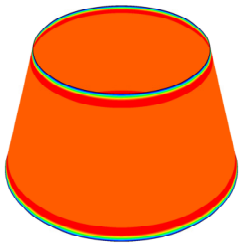

(a) Before buckling, for $U = 2333$.

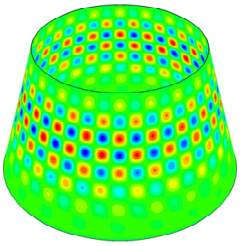

(b) At buckling, for $U = 4389$.

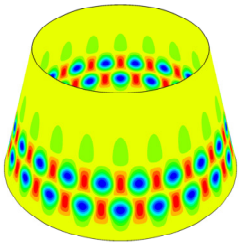

(c) After buckling, for $U = 5399$.

Figure 6.6: Deformation shapes (radial displacement) of the full-scale cross-ply composite conical shell at the instances indicated in Figure 6.5.

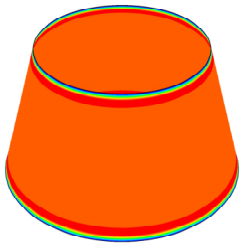

(a) Before buckling, for $U = 2333$.

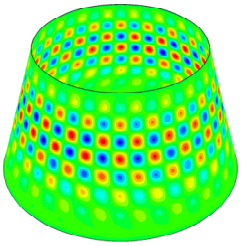

(b) At buckling, for $U = 4327$.

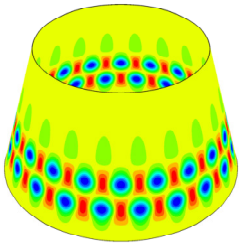

(c) After buckling, for $U = 5399$.

Figure 6.7: Deformation shapes (radial displacement) of the reduced-scale cross-ply composite conical shell at the instances indicated in Figure 6.5.

For larger cone angles, however, this assumption must be checked and the effect on the scaling

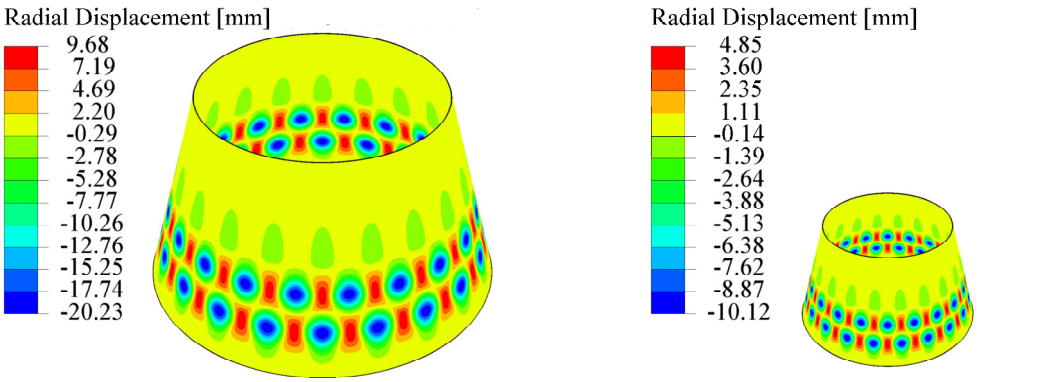

(a) Full-scale conical shell. **(b)** Reduced-scale conical shell.

Figure 6.8: Comparison of the dimensional postbuckling deformation shape. Relative size of the two shells is as in reality.

should be evaluated. Therefore, the Payload Attach Fitting (PAF) of the SLS is analyzed, which has a cone angle α of 45° [20]. The geometric dimensions and layup of the full-scale and reduced-scale conical shells are detailed in Table 6.8. The same material and layup are used as for the cross-ply SLS USA conical shell previously discussed. Moreover, ply-level scaling is applied. The two conical shells are compared using the semi-analytical solution, a linear eigenvalue analysis, and an implicit dynamic analysis.

Table 6.8: Geometry description of the cross-ply composite SLS PAF conical shells.

	Cone angle α [deg]	**Length L [mm]**	**Small radius R_1 [mm]**	**Stacking sequence [deg]**
FS	45	4831	787	$[0_2/90_2]_{3S}$
RS	45	2419	394	$[0/90]_{3S}$

As this is another structure than the previously investigated SLS USA conical shell, a new mesh convergence study is performed using the linear eigenvalue analysis. For the full-scale shell, convergence is achieved for the mesh of 50 mm. Similarly, for the reduced-scale conical shell, a mesh size of 25 mm yields convergence. For the implicit dynamic analysis, the same reasoning is applied as in subsection 6.2.3 for the SLS USA. Based on the linear buckling displacement, the displacement rates for the full-scale and reduced-scale shells are determined to be 1.2 mm/s and 0.6 mm/s, respectively. Because of the different geometry, the results are checked by performing an additional analysis with displacement rates of 0.75 mm/s and 0.375 mm/s. The results of the two analyses are within 1% of each other for both the full-scale and the reduced-scale shell. It is therefore concluded that the results are converged. The dimensional results for the two conical shells are summarized in Table 6.9. Good correlation is observed between the three analysis types for both shells. It is checked if failure occurs after buckling. Prior to buckling, the failure indices for full-scale and reduced-scale shell never exceed 0.077 and 0.076, respectively.

The full-scale and reduced-scale shells are compared nondimensionally. The scaling parameters are all satisfied within 0.15%. The buckling load, displacement and stiffness are given in Table 6.10 and Figure 6.9. The agreement between full-scale and reduced-scale shells is very

Table 6.9: Buckling load and displacement for the cross-ply composite SLS PAF conical shells.

		Buckling load P_{cr} [kN]	**Buckling displ. u_{cr} [mm]**
Semi-analytical solution	FS	1103	n.a.
	RS	275.8	n.a.
Eigenvalue analysis	FS	1053	2.28
	RS	259.8	1.14
Implicit dynamic analysis	FS	1074	2.33
	RS	262.6	1.15

good across all analyses. The differences for the scaling parameters and the semi-analytical solution can be attributed to rounding of the dimensions of the reduced-scale shell. The same semi-analytical buckling mode (8,12) is predicted for the two shells. The accuracy of the linear reduced-scale prediction is good as well with errors of 1.17% and 0.507% for the buckling load and displacement, respectively. The linear buckling modes are not shown here but they are similar to the deformation shapes at buckling shown in Figure 6.10b and Figure 6.11b. They are nearly identical as well.

The same conclusions can be drawn for the implicit dynamic analysis, for which errors of 2.12% and 1.52% are observed for load and displacement prediction, respectively. The load-displacement paths do not converge to the same postbuckling load. The postbuckling deformation shapes in Figure 6.10 and Figure 6.11 are also slightly different: the full-scale shell has a (2,12) deformation shape, whereas the reduced-scale shell has a (2,11) shape. The deformation shapes before and at buckling are similar for the two shells. The radial displacements are not shown here, but the nondimensional minimum and maximum values are compared in Table 6.11. The difference is larger than for the SLS USA. This can be explained by the different postbuckling path and deformation shape. The reduced-scale shell minimum and maximum values are more pronounced than the ones of the full-scale shell.

Table 6.10: Comparison of nondimensional buckling load, displacement and stiffness for the cross-ply composite SLS PAF conical shells.

		Buckling load K_{xx}		**Buckling displ. U**	**Stiffness K_{xx}/U**	
		$z_1 = 0$	$z_1 = 1$	$z_1 \epsilon [0, 1]$	$z_1 = 0$	$z_1 = 1$
Semi-analytical solution	FS	371.4	1983	n.a.	n.a.	n.a.
	RS	371.8	1986	n.a.	n.a.	n.a.
	Δ	(+0.119%)	(+0.134%)			
Eigenvalue analysis	FS	354.4	1893	5135	0.06902	0.3686
	RS	350.3	1871	5108	0.06858	0.3663
	Δ	(−1.17%)	(−1.16%)	(−0.526%)	(−0.637%)	(−0.624%)
Implicit dynamic analysis	FS	361.7	1932	5246	0.06895	0.3683
	RS	354.1	1891	5167	0.06853	0.3660
	Δ	(-2.10%)	(-2.12%)	(-1.51%)	(-0.609%)	(-0.624%)

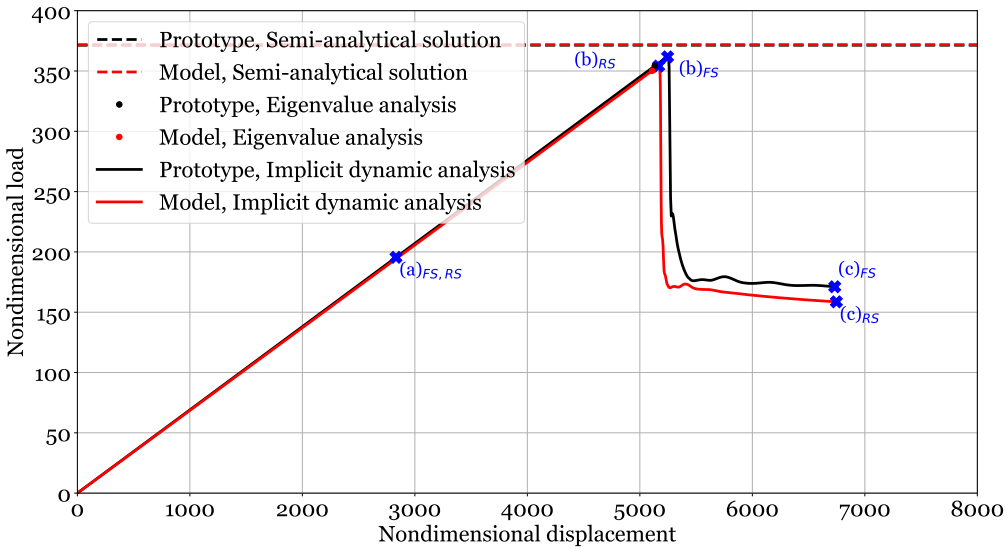

Figure 6.9: Nondimensional load-displacement curve of the full- and reduced-scale cross-ply composite SLS PAF conical shells, using K_{xx} at $z_1 = 0$.

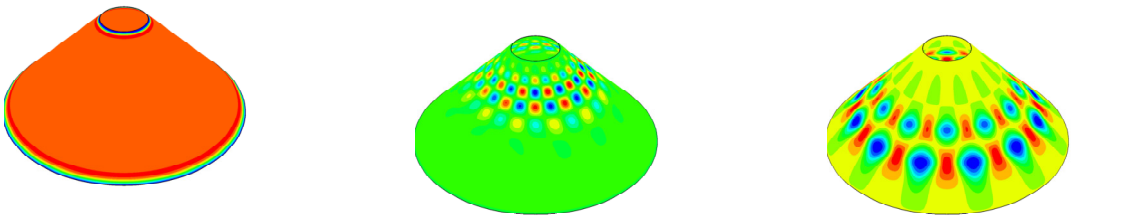

(a) Before buckling, for $U = 2829$.

(b) At buckling, for $U = 5246$.

(c) After buckling, for $U = 6748$.

Figure 6.10: Deformation shapes (radial displacement) of the full-scale cross-ply composite SLS PAF conical shell at the instances indicated in Figure 6.9.

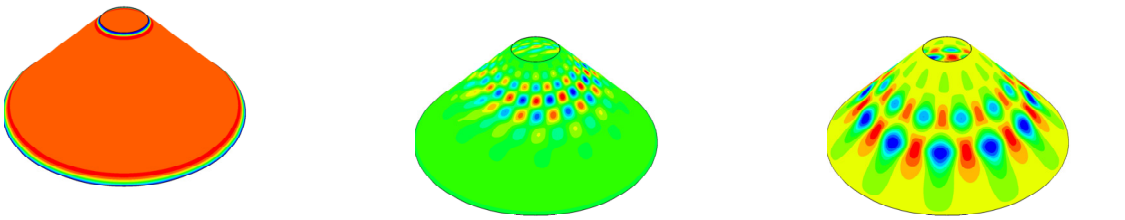

(a) Before buckling, for $U = 2829$.

(b) At buckling, for $U = 5167$.

(c) After buckling, for $U = 6748$.

Figure 6.11: Deformation shapes (radial displacement) of the reduced-scale cross-ply composite SLS PAF conical shell at the instances indicated in Figure 6.9.

Table 6.11: Comparison of the minimum and maximum nondimensional radial displacement for the cross-ply composite SLS PAF conical shells.

	Minimum radial displacement $W_{\mathbf{min}}$	**Maximum radial displacement $W_{\mathbf{max}}$**	**Ratio $W_{\mathbf{max}}/W_{\mathbf{min}}$**
FS	-26.9	12.9	-0.482
RS	-28.9	13.8	-0.476
Δ	(+7.43%)	(+6.98%)	(-1.24%)

6.6 Concluding Remarks

This chapter discusses the scaling of a cross-ply laminated conical shell. By using ply-level scaling, all scaling parameters and all assumptions could be satisfied. This scaling technique can be understood as reducing the ply thickness by a constant factor, by which the geometry is also scaled. Instead of actually reducing the ply thickness, the number of identical adjacent plies is reduced. The semi-analytical solution prediction accuracy is excellent, both for buckling load and deformation shape. This verifies the nondimensional equations and the scaling methodology. The linear eigenvalue analysis and implicit dynamic analysis predictions are very accurate for all compared parameters. Although postbuckling is not taken into account in the scaling methodology, the load-displacement curve is similar in this regime as well. The deformation shapes are identical for the whole analysis and the minimum and maximum nondimensional radial displacements agree excellently.

In addition, the assumption of the mildly varying curvature was checked using the scaling of a conical shell with cone angle $\alpha = 45°$. This was successful and the prediction accuracy of the analyzed parameters was similar to that of the small cone angle shell. The postbuckling behavior was not identical for the two shells; the deformation shape was slightly different and the radial displacement was not scaled with the same accuracy as the other parameters.

These results show that the scaling methodology is capable of scaling cross-ply composite conical shells. This layup type satisfies all laminate requirements (i.e. symmetry, balance and negligible flexural anisotropy). The buckling load, displacement, deformation shape and radial displacement were scaled accurately. Although these results are satisfactory, the practical use of this scaling remains limited. Cross-ply stacking sequences are hardly used for applications, let alone cross-ply stacking sequences where several same angle plies are adjacent. Additionally, it is not recommended to have many same angle plies next to each other to avoid rapid damage propagation. As a result, the size of the reduced-scale shell will still be rather large, because the geometry is scaled by the same number as the thickness. The analysis is, however, still relevant, because it shows the accuracy of the scaling methodology in the ideal case, so when the laminate assumptions and all scaling parameters are satisfied.

Chapter 7

Scaling of Composite Conical Shell

In the previous chapters, the scaling methodology has been applied to isotropic and cross-ply composite conical shells. Although these analyses verify the scaling methodology, they are not relevant for other, more realistic composite shells. Ply-level scaling can only be applied to laminates with adjacent identical plies, which are typically avoided to prevent rapid damage propagation. Therefore, this chapter discusses the application of the methodology to a quasi-isotropic composite conical shell without using ply-level scaling. First, the conical shell designs are elaborated upon, after which the buckling behavior is analyzed and it is checked if material failure occurs after buckling. Then, the full-scale and reduced-scale results are compared in their nondimensional form.

7.1 Conical Shell Designs

The design of the full-scale composite shell is discussed in this section. Furthermore, it is explained which reduced-scale configurations can be designed for this full-scale shell and how these designs are found using the methodology.

7.1.1 Full-Scale Conical Shell Description

The SLS USA is analyzed again, of which the geometry is detailed in Table 4.1. The original stacking sequence is a sandwich composite with a 1 inch (i.e. 25.4 mm) aluminum honeycomb core and a quasi-isotropic facesheet layup, $[45/90/\text{-}45/0]_S$ [20]. A monolithic composite stacking sequence is created which results in a buckling load similar to the one of the original sandwich laminate. To limit the computational effort, this comparison is made using the semi-analytical solution. Because the facesheets are quasi-isotropic, the monolithic composite layup also uses a quasi-isotropic basis. The IM7/8552 carbon fiber is used as material for the full-scale shell.

It should be noted that reference [20] uses a different ply thickness (i.e. $t_{\text{ply}} = 0.135$ mm) than the ply thickness adopted here (i.e. $t_{\text{ply}} = 0.18$ mm). For the determination of the equivalent monolithic composite, the original, smaller ply thickness is used for the sandwich shell, such

that the results could be compared to the results in the paper. For the monolithic composite shell, the thickness of 0.18 mm is used, to be consistent with the other shells analyzed here. The stacking sequence $[45/90/\text{-}45/0]_{7S}$ results in a semi-analytical buckling load 2.7% lower than the semi-analytical buckling load of the sandwich structure. The structure details are summarized in Table 7.1.

7.1.2 Reduced-Scale Conical Shell Design

There are several options for the design of the reduced-scale conical shell. More specifically, the shell can be made of an isotropic material, or from a composite material. In the latter case, one can opt for a monolithic or a sandwich laminate. The sandwich design is not considered here, because if large reductions in size are desired, the reduced-scale core thickness will also be very small, which leads to unproducible designs. For the monolithic composite, the same material is used as for the facesheets of the full-scale shell. Aluminum alloy 2024-T4, specified in Table 4.3, is assumed to be used for the isotropic shell.

With the material chosen, the first step in the scaling methodology is completed, see Figure 3.5 and Figure 3.6. For the composite shell, the next step is to determine the layup. The number of stacking sequence options is immense, so choices have to be made to limit this. At the same time, this is the only design freedom for composite reduced-scale shells, so it should be used smartly: it influences the geometry and size of the shell. Below, it is explained which limitations are set and how strictly they are enforced. The resulting layup designs are also discussed. Afterwards, it is exemplified how one of the designs is obtained using the step-by-step scaling procedure. Finally, all reduced-scale shell designs are summarized and discussed.

Imposed Limitations and Layup Designs

Below, the considerations for the reduced-scale layup choice are explained, together with how strictly the limitations are followed.

1. **Symmetry and balance requirement.** These requirements are strictly enforced, in agreement with the assumptions made in the scaling methodology.
2. **Layup types.** One can combine various ply orientations in one layup, but the analysis here is limited to two layup types.
    a. **Same layup basis as full-scale shell.** For this full-scale shell, this means that a [45/90/-45/0] basis is repeated and mirrored, such that the symmetry and balance requirements are satisfied.
    b. **One variable ply angle θ.** Repetitions and inversions of the ply group $[\theta, -\theta]$ are combined to yield a symmetric, balanced layup. The choice for only allowing one ply angle variable is made to limit the total number of variables to be determined.
3. **Flexural anisotropy assumption.** This assumption is not strictly enforced, because through experience with the methodology, it is observed that it would limit the design options too much. Designs with and without negligible flexural anisotropy are considered, such that the results can be compared and the influence of the assumption can be evaluated.

4. **Conform to common test equipment sizes.** Once the layup is determined and the shell is designed, it is checked if the shell would complies with common lab test equipment constraints, as detailed in Table 4.2. This is also not strictly enforced for the same reason as given for the flexural anisotropy.

Based on these considerations, three composite designs are created. In addition, an isotropic reduced-scale shell is designed. This shell automatically satisfies the symmetry, balance and flexural anisotropy requirements. As a result, the shell is designed such that it would conform to common test equipment sizes. The four designs are listed below.

A. **Same layup basis as full-scale shell.** The ply group [45/90/-45/0] is used as layup basis. To satisfy the symmetry and balance assumptions, the group is mirrored, such that a $[45/90/\text{-}45/0]_S$ layup is obtained. The flexural anisotropy parameters and the size of the shell are checked later.

B. $\boldsymbol{[\theta/\text{-}\theta/\overline{0}]_S}$**.** This layup considers one variable ply angle. The symmetry and balance requirements are satisfied. For this design, priority is given to the test equipment size over the flexural anisotropy assumption. The 0° ply is added because it reduces the flexural anisotropy parameters, while still satisfying the size constraints set by test equipment. The flexural anisotropy is, however, not negligible.

C. $\boldsymbol{[\theta/\text{-}\theta]_{S^3}}$**.** This layup also considers only one variable ply angle and the symmetry and balance requirements are satisfied. In contrast to configuration B, the priority is given to the flexural anisotropy assumption over the test equipment size. The flexural anisotropy is negligible, but the shell does not comply with common test equipment constraints.

D. **Isotropic.** This shell intrinsically satisfies the symmetry, balance and flexural anisotropy requirements. The size is chosen such that the reduced-scale shell fits in common test equipment.

Step-by-Step Application of the Methodology

Below, it is explained how configuration B is found using the scaling methodology in Figure 3.6.

1. **Choose material.** As explained before, the same material is used for the reduced-scale shell as for the full-scale shell.

2. **Determine (symmetric, balanced) layup using $\boldsymbol{\mu}$ and $\boldsymbol{\beta}$.** The layup structure has been chosen already. The variation of the orthotropy parameters with the ply angle θ is shown in Figure 7.1. The full-scale values for μ and β are indicated with black horizontal lines. The reduced-scale values of these parameters are calculated for θ ranging from 0° to 90°. For $\theta = 16°$, the reduced-scale orthotropy parameters are both approximately equal to the full-scale values. Note that the ply angle is rounded to an integer value for manufacturing considerations.

3. **Determine ratio $\boldsymbol{\frac{R_1}{L}}$ using $\boldsymbol{\alpha_m}$ and $\boldsymbol{\alpha_b}$ at $\boldsymbol{z_1 = 0}$.** Based on the membrane parameter in Equation 3.72a, the radius-to-length ratio should be 0.308. Based on the bending parameter in Equation 3.72b, it should be 0.304. Therefore, a value of 0.306 is used for the next step.

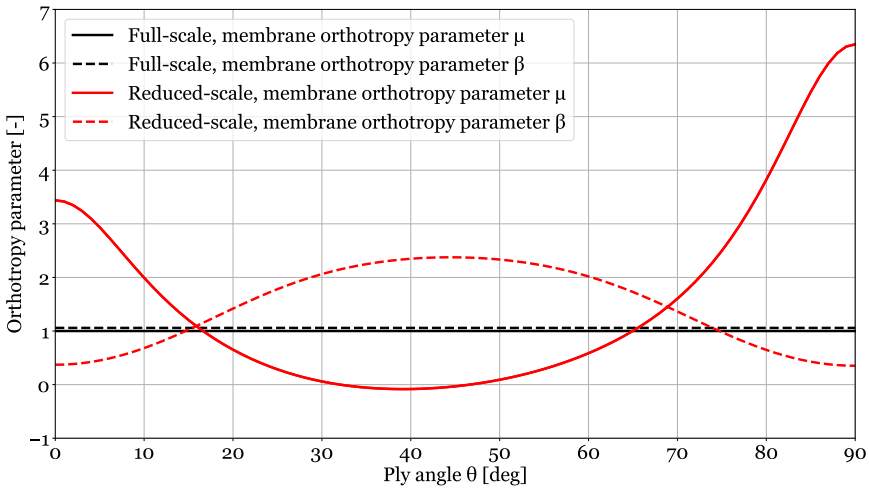

Figure 7.1: Variation of the orthotropy parameters with ply angle for a $[\theta/-\theta/\overline{0}]_S$ layup.

4. **Determine cone angle α using α_m and α_b at $z_1 = 1$.** Based on the membrane parameter (Equation 3.72a), the cone angle should be 8.01°. Based on the bending parameter (Equation 3.72b), it should be 7.62°. Only integer values of the cone angle are considered, so $\alpha = 8°$.

5. **Determine R_1 and L using Z_2.** From the equivalent Batdorf-Stein parameter (Equation 3.72e) at $z_1 = 0$, the top radius is found to be 253 mm. Similarly for $z_1 = 1$, the length is found to be 808 mm. This results in a $\frac{R_1}{L} = 0.313$, which is slightly higher than the values required to satisfy α_m and α_b in step 3.

The same procedure is applied for configurations A and C. For configuration A, the layup is already fixed, so the values of μ and β cannot be tailored to match the full-scale values anymore. They are therefore not part of the design procedure in this case, so step 2 is skipped. For configuration C, two ply angles are found in step 2 which satisfy the μ and β requirements. As a result, there are two designs based on configuration C. The isotropic design of configuration D is obtained by following the methodology shown in Figure 3.5. The large radius is set to approximately 400 mm, from which the other dimensions are derived.

Final Reduced-Scale Shell Designs

The designs in Table 7.1 are created. All shells satisfy the symmetry and balance requirements. The large radius of configuration A is too large to fit in common test equipment. In order to reduce the radius, a thinner layup would be required. This is, however, not possible while complying with the symmetry and balance requirements. Priority is given to the laminate requirements, so the design is not altered. Configuration B, on the other hand, fits in common test equipment. Configurations C.i and C.ii are both too large, as expected. Only one of these two configurations will be analyzed further, because they are similar. Configuration C.i is excluded from the analysis, because it exceeds both the maximum height requirement of 1000 mm and the maximum radius requirement of 400 mm. Lastly, configuration D fits in common

test equipment. It should be noted that thickness is small and the accuracy up to 0.01 mm may be difficult to achieve.

Table 7.1: Geometry description of the full-scale (FS) quasi-isotropic composite conical shell and its reduced-scale (RS) configurations.

Config.	Cone angle α [deg]	Length L [mm]	Small radius R_1 [mm]	Large radius R_2 [mm]	Stacking sequence [deg]
FS	15	4996	2910	4203	$[45/90/\text{-}45/0]_{7S}$
RS A	16	625	387	559	$[45/90/\text{-}45/0]_{S}$
RS B	8	808	253	365	$[16/\text{-}16/\overline{0}]_{S}$
RS C.i	8	2607	816	1179	$[15/\text{-}15]_{S^3}$
RS C.ii	29	847	924	1335	$[75/\text{-}75]_{S^3}$
RS D	15	472	275	397	Isotropic, $t = 0.94$ mm

7.2 Buckling Analyses

This section discusses the buckling analyses. In the subsequent steps, the least promising reduced-scale configurations are eliminated from the analysis to limit the computational cost.

7.2.1 Semi-analytical Solution

The full-scale shell and the reduced-scale configurations A, B, C.ii, and D are analyzed using the semi-analytical buckling solution. In addition, it is checked if the flexural anisotropy parameters are negligible. The results are given in Table 7.2. The buckling mode of the full-scale shell is correctly predicted by all reduced-scale configurations. The buckling load prediction is accurate for all shells, except for configuration A. Recall that parameters μ and β were not taken into account for the design of this shell. The μ parameter is identical to the full-scale value, but β differs by 44.3%. This large discrepancy explains the low buckling load prediction accuracy. This result is also in agreement with Rezaeepazhand et al. [95] for cylindrical shells, who found that the accuracy of this type of layup scaling reduces for large differences in laminate thickness. Because of this low prediction accuracy, configuration A is excluded from further analysis. Furthermore, configuration B is excluded based on its high flexural anisotropy parameters. Configurations C.ii and D are analyzed with linear finite element models.

7.2.2 Linear Eigenvalue Analysis

Mesh convergence studies are performed for the three analyzed shells. This results in a mesh size of 50 mm for the full-scale shell, a size of 12 mm for configuration C.ii, and a size of 5 mm for configuration D. The linear buckling loads and displacements are summarized in Table 7.3. Both parameters are well predicted by the two reduced-scale shells. The buckling modes, shown in Figure 7.2, are nearly identical to the full-scale linear buckling mode. Configuration C.ii will be analyzed with a nonlinear analysis, because it is most interesting: it has a different cone angle, stacking sequence type and radius-to-length ratio than the full-scale shell and it has non-zero, but negligible, flexural anisotropy. These are all parameters which

Table 7.2: Semi-analytical solution and flexural anisotropy results for the different configurations. The difference in K_{xx} with the full-scale value is given between brackets. Note that $i, j = 1, 2$.

Config.	Buckling load [kN]	Buckling mode (m, n)	Nondimensional buckling load K_{xx}	$\frac{D_{16}}{\min(D_{ij})}$	$\frac{D_{26}}{\min(D_{ij})}$
FS	20173	(15,0)	1807	9.42%	9.42%
RS A	325.3	(15,0)	1553 (-14.1%)	63.4%	63.4%
RS B	103.6	(15,0)	1834 (+1.49%)	178%	20.5%
RS C.ii	829.4	(15,0)	1859 (+2.88%)	1.48%	14.1%
RS D	232.9	(15,0)	1858 (+2.82%)	0.0%	0.0%

are known to influence the buckling response and imperfection sensitivity. The isotropic shell, configuration D, is interesting from a practical perspective, but poses less challenges on the scaling methodology. A size comparison of the reduced-scale shell and configuration C.ii is shown in Figure 7.3.

Table 7.3: Linear eigenvalue results for the different configurations. The difference in K_{xx} and U with the full-scale value is given between brackets.

Config.	Buckling load [kN]	Buckling displ. [mm]	Nondimensional buckling load K_{xx}	Nondimensional buckling displ. U
FS	20289	8.43	1817	4399
RS C.ii	829.7	4.65	1859 (+2.31%)	4505 (+2.41%)
RS D	235.0	0.821	1875 (+3.19%)	4527 (+2.91%)

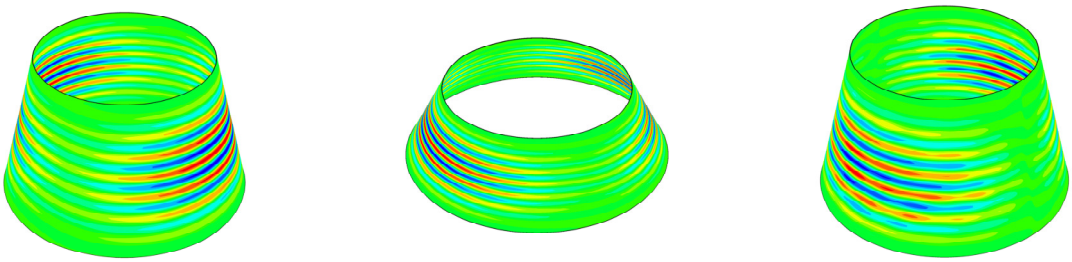

(a) Full-scale shell. **(b)** Configuration C.ii. **(c)** Configuration D.

Figure 7.2: First eigenmode of the full-scale quasi-isotropic composite conical shell and its reduced-scale configurations, showing radial displacement.

7.2.3 Implicit Dynamic Analysis

The full-scale conical shell and reduced-scale configuration C.ii are analyzed with an implicit dynamic analysis. For the former, a displacement rate of 4.32 mm/s is used, for the latter 2.38 mm/s. The other settings are identical to the ones determined in section 4.3. The results are visualized in Figure 7.4 and summarized in Table 7.4. It can be seen that an eigenmode imperfection of 1% of the thickness is added. This is done to avoid the load plateau observed for the reduced-scale shell. This results in a knockdown factor KDF=0.900 for the full-scale shell and KDF=0.871 for the reduced-scale shell.

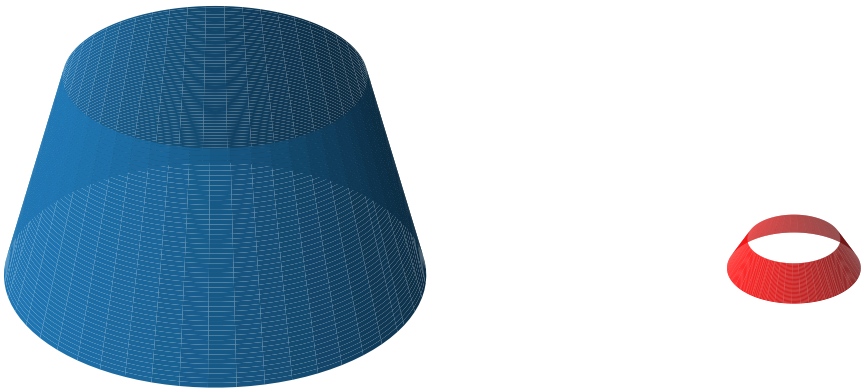

Figure 7.3: Visualization of the full-scale (blue, left) quasi-isotropic conical shell and its reduced-scale configuration (red, right). Both shells are 73x smaller than in reality.

Table 7.4: Buckling load and displacement for the full-scale quasi-isotropic composite conical shell and its reduced-scale configuration.

Config.	Buckling load P_{cr} [kN]	Buckling displ. u_{cr} [mm]
FS	18265	7.67
RS C.ii	723.8	4.08

7.3 Failure Assessment

Next, it is checked if failure occurs after buckling. The failure indices at incipient buckling are all well below 1, as can be seen in Table 7.5, so failure is not expected. For the reduced-scale shell, the innermost ply (i.e. ply 1) is critical, which has a 75° orientation. This ply is located furthest away from the mid-surface and consequently experiences the highest bending strains. It is therefore not surprising that this is the critical ply. According to the Hashin criterion, the critical index is caused by fiber tension. The shell experiences circumferential tension due to the Poisson's effect, which explains this prediction. For the full-scale shell, ply 4, which is the innermost 0° ply, is critical. This ply experiences compression in the fiber direction due to the axial loading, in combination with bending due to the deformation. The compression behavior of the composite is mainly governed by the matrix and the fiber-matrix interface. As a result, the corresponding strength and failure strain are low, thus causing this ply to be critical. The critical location is identical for all indices and for the two shells and occurs near the top edge, but not at it. This is in line with the expectations. Typically, pad-ups are added in this region as a reinforcement.

The strains in the four inner plies are given in Table 7.6. These plies are observed to have the highest strains. The critical ones, yielding to the maximum failure index, are indicated in bold face. Note that these are not necessarily the highest strains, but the highest relative to the failure strain in that direction. From ply 2 and 4 of the full-scale shell, it can be seen that strains are negative in meridional direction and positive in circumferential direction, as expected due to the axial compression. In addition, the shear strain is small for ply 2 and 4, and large for ply 1 and 3, which is in line with the expectation seen the load case. The fiber direction of the inner 0° ply is critical for this shell. The explanation for this was given above. For the reduced-scale shell, the shear strain in ply 1 (75°) is critical. Strain contour plots

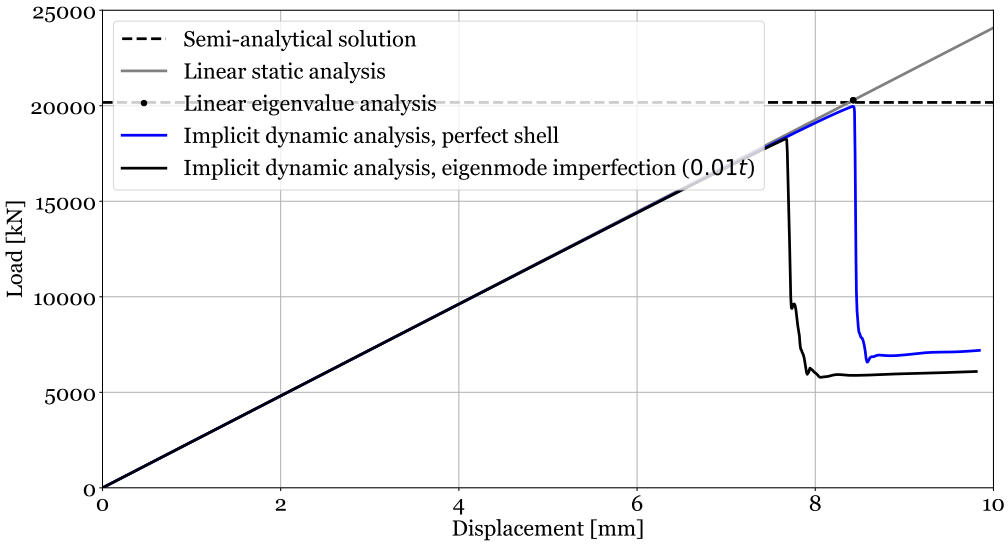

(a) Full-scale conical shell.

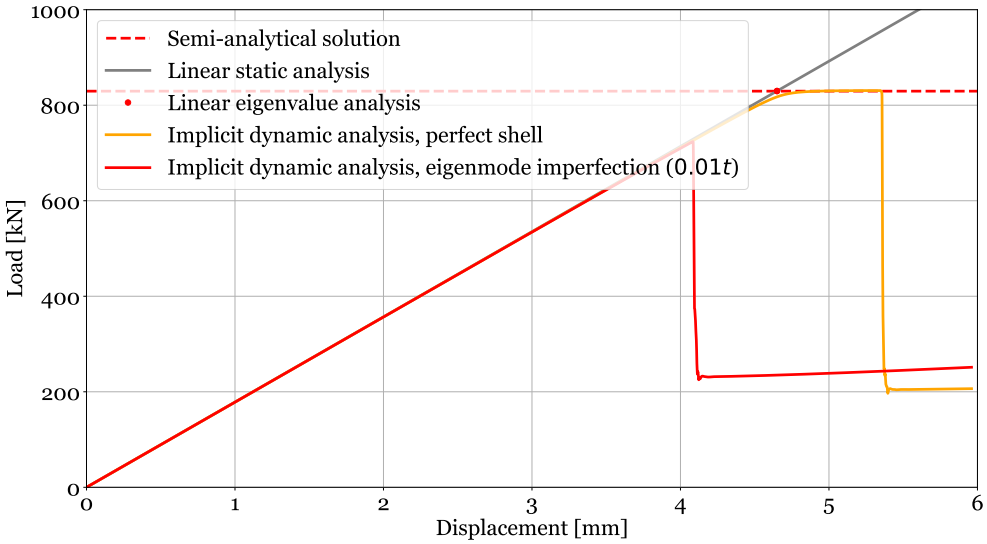

(b) Reduced-scale conical shell configuration C.ii.

Figure 7.4: Load-displacement curves of the full-scale quasi-isotropic composite conical shell and its reduced-scale configuration.

of the critical ply are shown in Figure 7.5. The critical location, close to the edge, can be clearly seen here. Buckling initiation can be recognized as well, creating deformation waves, and thus locally higher strains. These are especially visible in Figure 7.5e.

Table 7.5: Maximum failure indices at incipient buckling for the full-scale quasi-isotropic composite conical shell and its reduced-scale configuration.

Failure criteria	FS	RS C.ii
Max strain	0.201 (ply 4, 0°)	0.208 (ply 1, 75°)
Max stress	0.201 (ply 4, 0°)	0.208 (ply 1, 75°)
Tsai-Hill	0.201 (ply 4, 0°)	0.281 (ply 1, 75°)
Tsai-Wu	0.200 (ply 4, 0°)	0.232 (ply 1, 75°)
Hashin	0.0403 (ply 4, 0°) fiber compression	0.0430 (ply 1, 75°) fiber tension

Table 7.6: Maximum strain values at incipient buckling in the four inner plies for the full-scale quasi-isotropic composite conical shell and its reduced-scale configuration.

	FS				RS C.ii			
	θ [deg]	ϵ_{11} [$\mu\epsilon$]	ϵ_{22} [$\mu\epsilon$]	ϵ_{12} [$\mu\epsilon$]	θ [deg]	ϵ_{11} [$\mu\epsilon$]	ϵ_{22} [$\mu\epsilon$]	ϵ_{12} [$\mu\epsilon$]
Ply 1	45°	-1079	-1105	3183	75°	320.2	-5922	**3568**
Ply 2	90°	862.2	-2332	-789.3	−75°	312.7	-5770	-3499
Ply 3	−45°	-1085	-1061	-3164	−75°	308.0	-5622	-3382
Ply 4	0°	**-2312**	859.7	770.8	75°	309.6	-5476	3258

7.4 Comparison of the Full-Scale and Reduced-Scale Conical Shells

The full-scale and reduced-scale shells are compared nondimensionally. First, the scaling parameters are evaluated, followed by the load-displacement graphs. The deformation shapes are also compared.

7.4.1 Scaling Parameters

The nondimensional parameters are reported in Table 7.7. The agreement is good for all parameters and especially for the Batdorf-Stein equivalent parameter. The difference in orthotropy parameters is caused by the rounding of the ply angle to an integer value, as well as averaging the result to minimize the error with respect to both parameters. The difference in bending parameter is due to the rounding of the cone angle to an integer value and due to not using the radius-to-length ratio as output from this parameter.

7.4.2 Nondimensional Load-Displacement Curves

Next, the nondimensional load-displacement curves are compared, shown in Figure 7.6. The nondimensional load, displacement and stiffness are summarized per analysis in Table 7.8. The nondimensional buckling loads of full-scale and reduced-scale shells match well according to the semi-analytical solution. The linear eigenvalue analysis gives a similar prediction accuracy. The implicit dynamic analysis results are even more accurate. The largest discrepancy occurs for the buckling displacement and measures 1.22%. The nondimensional stiffness is predicted very well. The load-displacement curves have a similar shape and converge to the same postbuckling load. The initial postbuckling path is different, but only during the load drop. The imperfection sensitivity differs slightly: for the full-scale shell, a knockdown factor of KDF=0.900 is observed and for the reduced-scale shell, KDF=0.871.

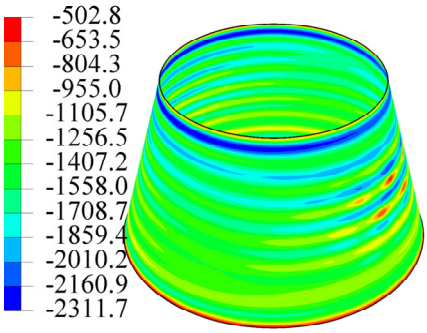

(a) Full-scale shell ply 4 (0°), ϵ_{11} [$\mu\epsilon$].

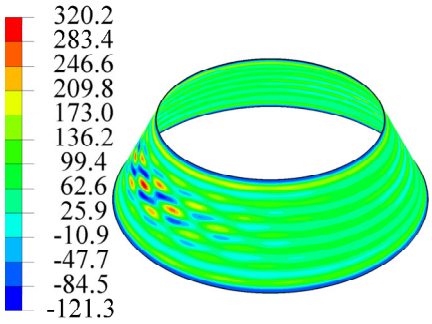

(b) Reduced-scale shell ply 1 (75°), ϵ_{11} [$\mu\epsilon$].

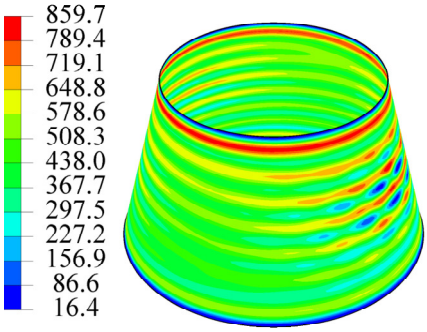

(c) Full-scale shell ply 4 (0°), ϵ_{22} [$\mu\epsilon$].

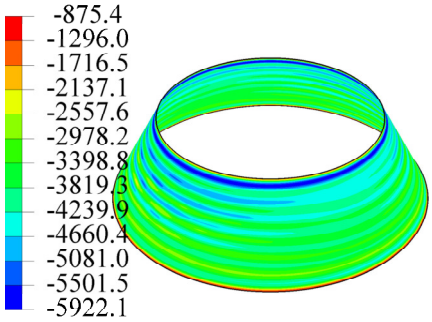

(d) Reduced-scale shell ply 1 (75°), ϵ_{22} [$\mu\epsilon$].

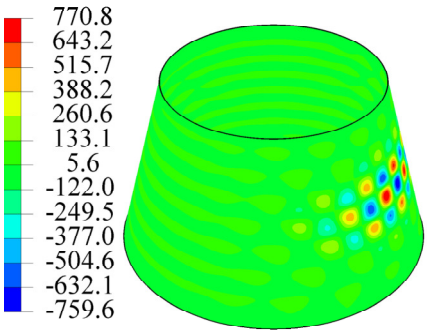

(e) Full-scale shell ply 4 (0°), ϵ_{12} [$\mu\epsilon$].

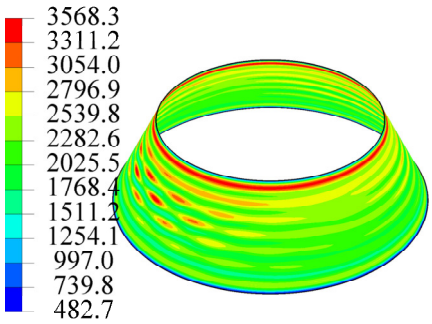

(f) Reduced-scale shell ply 1 (75°), ϵ_{12} [$\mu\epsilon$].

Figure 7.5: Strains in the critical plies at incipient buckling for the full-scale quasi-isotropic composite conical shell and its reduced-scale configuration.

It is surprising that the implicit dynamic analysis gives a more accurate prediction than the semi-analytical solution and the linear eigenvalue analysis. This is believed to be caused by a combination of errors. The semi-analytical prediction gives an overestimation of the buckling load of 2.88% due to the differences in scaling parameters. The linear eigenvalue analysis also overestimates the buckling load, but by 2.32%. The difference in overestimation with the semi-analytical solution of -0.56% ($2.32\%-2.88\%$) can be explained by the small, but non-zero flexural anisotropy of the two shells and by slight differences in the finite element models.

Table 7.7: The nondimensional scaling parameters of the full-scale quasi-isotropic composite conical shell and its reduced-scale configuration.

	Membrane parameter α_m		**Bending parameter α_b**	
	$z_1 = 0$	$z_1 = 1$	$z_1 = 0$	$z_1 = 1$
FS	0.5825	0.8413	0.5657	0.8171
RS C.ii	0.5800	0.8377	0.5800	0.8377
Δ	(-0.428%)	(-0.424%)	(+2.52%)	(+2.52%)
	Batdorf-Stein eq. parameter Z_2		**Membrane orth. parameter μ**	**Flexural orth. parameter β**
	$z_1 = 0$	$z_1 = 1$	$z_1 \epsilon [0, 1]$	$z_1 \epsilon [0, 1]$
FS	266.9	385.5	1.000	1.058
RS C.ii	266.8	385.3	0.9432	1.031
Δ	(-0.0429%)	(-0.0389%)	(-5.68%)	(-2.55%)

The implicit dynamic analysis underestimates the buckling load by 0.85%. Thus, there is a difference of −3.17% (−0.85%−2.32%) with the eigenvalue prediction. This is attributed to the difference in imperfection sensitivity between the two shells. The difference in buckling load between the linear and nonlinear prediction is larger for the reduced-scale shell than for the full-scale shell. As a result, the overestimation observed for the eigenvalue prediction is counteracted by the larger imperfection sensitivity of the reduced-scale shell. In short, it can be concluded that the inclusion of phenomena which are not included in the scaling methodology, such as flexural anisotropy and imperfection sensitivity, change the prediction accuracy. They do not necessarily reduce the similarity between the two shells, because the effects of the phenomena on the prediction accuracy partially balance each other out.

Table 7.8: Comparison of nondimensional buckling load, displacement and stiffness for the full-scale quasi-isotropic composite conical shell and its reduced-scale configuration.

		Buckling load K_{xx}		**Buckling displ. U**	**Stiffness K_{xx}/U**	
		$z_1 = 0$	$z_1 = 1$	$z_1 \epsilon [0, 1]$	$z_1 = 0$	$z_1 = 1$
Semi-analytical solution	FS	1807	2609	n.a.	n.a.	n.a.
	RS C.ii	1859	2685	n.a.	n.a.	n.a.
	Δ	(+2.88%)	(+2.88%)			
Eigenvalue analysis	FS	1817	2624	4399	0.4130	0.5965
	RS C.ii	1859	2685	4505	0.4127	0.5960
	Δ	(+2.32%)	(+2.32%)	(+2.41%)	(−0.0726%)	(−0.0838%)
Implicit dynamic analysis	FS	1636	2363	4006	0.4084	0.5899
	RS C.ii	1622	2343	3957	0.4099	0.5921
	Δ	(-0.856%)	(-0.846%)	(-1.22%)	(+0.367%)	(+0.373%)

7.4.3 Deformation Shapes

For the semi-analytical solution, the buckling mode was predicted to be (15,0) for both conical shells. The linear buckling modes, shown in Figure 7.2, are also very similar, except for the rotation around the central axis. The nonlinear deformation shapes at three points during

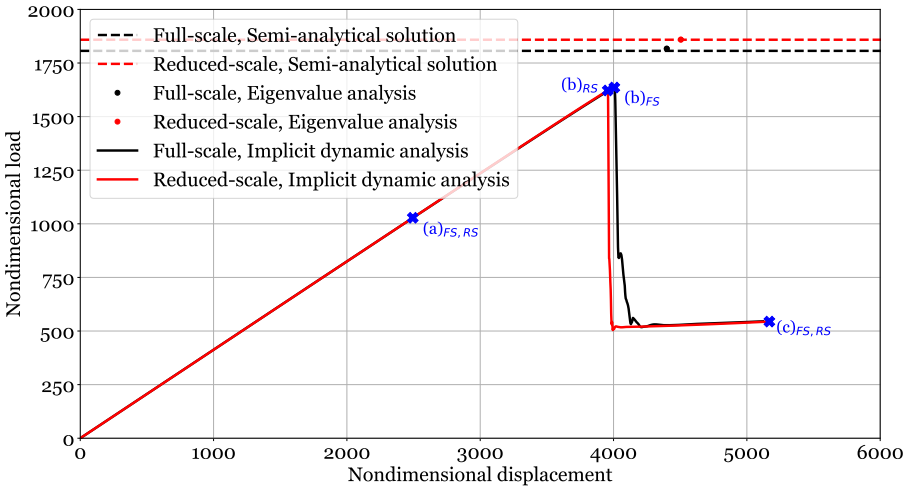

Figure 7.6: Nondimensional load-displacement curve of the full-scale quasi-isotropic composite conical shell and its reduced-scale configuration, using K_{xx} at $z_1 = 0$.

loading are compared in Figure 7.7 and Figure 7.8. The agreement is very good for all instances. Both shells have a (2,11) postbuckling deformation shape. The magnitude of the radial displacement is shown in Figure 7.9. The ratio of maximum to minimum radial displacement equals -0.458 and -0.452 for full-scale and reduced-scale shells, respectively. This is within 1.4% of each other.

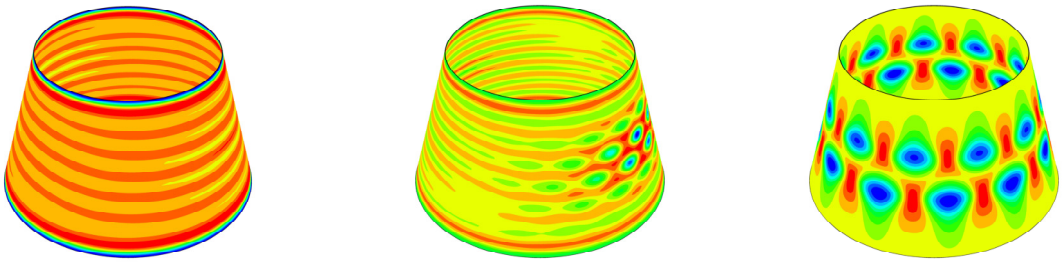

(a) Before buckling, for $U = 2503$. **(b)** At buckling, for $U = 4006$. **(c)** After buckling, for $U = 5121$.

Figure 7.7: Deformation shapes (radial displacement) of the full-scale quasi-isotropic composite conical shell at the instances indicated in Figure 7.6.

The scalability of the radial displacement is analyzed by evaluating its nondimensional form. The result is shown in Figure 7.10. The minimum and maximum values are compared in Table 7.9. The results are good, the values match within 4.07% and the ratios of minimum to maximum displacement differ by 6.92%. These differences are larger than the differences found for the buckling load and meridional displacement, but are still acceptable. Similar to the isotropic shell, this may be caused by the membrane prebuckling assumption and neglecting the presence of imperfections in the methodology. In addition, the comparison is made for a deformation shape in the postbuckling regime, which is not accounted for in the methodology. Overall, the nondimensional radial displacement is well predicted for the whole shell, as can be seen in Figure 7.10. Only near the top edge, there are some differences.

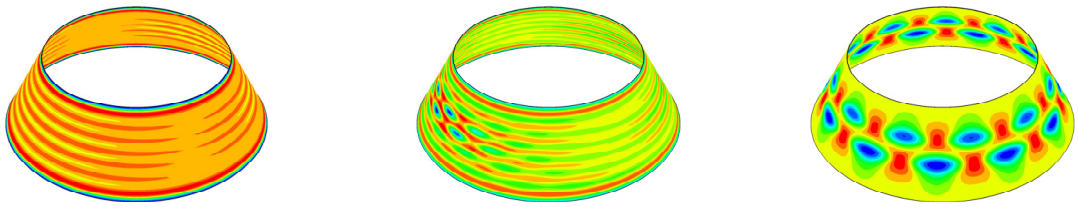

(a) Before buckling, for $U = 2503$. **(b)** At buckling, for $U = 3957$. **(c)** After buckling, for $U = 5123$.

Figure 7.8: Deformation shapes (radial displacement) of the reduced-scale composite conical shell at the instances indicated in Figure 7.6.

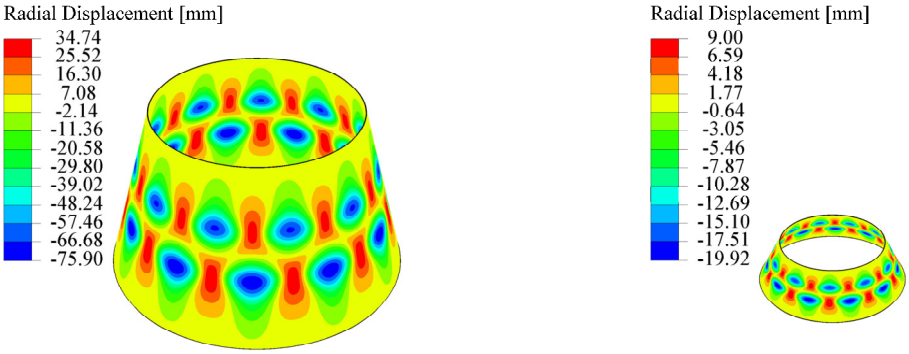

(a) Full-scale conical shell. **(b)** Reduced-scale conical shell.

Figure 7.9: Comparison of the dimensional postbuckling deformation shape. Reduced-scale shell is 1.55x enlarged compared to the full-scale shell for visibility.

Table 7.9: Comparison of the minimum and maximum nondimensional radial displacement for the full-scale quasi-istropic composite conical shell and its reduced-scale configuration.

	Minimum radial displacement $W_{\min}$	**Maximum radial displacement $W_{\max}$**	**Ratio $W_{\max}/W_{\min}$**
FS	-26.1	11.7	-0.448
RS	-26.9	11.2	-0.417
Δ	(+3.07%)	(-4.07%)	(-6.92%)

7.5 Concluding Remarks

The scaling of a quasi-isotropic composite conical shell is discussed in this chapter. For the reduced-scale shell, several designs were developed, considering the laminate assumptions and test equipment constraints. The most promising reduced-scale configuration was selected, based on the flexural anisotropy assumption and the semi-analytical prediction accuracy. Configuration C.ii was analyzed in detail and has a larger cone angle and radius-to-length ratio than the full-scale shell and an angle-ply symmetric layup. Although these parameters are known to affect the buckling response and imperfection sensitivity, the predictions were accurate. Failure is not expected to occur prior to buckling for the full-scale shell, nor for the reduced-scale shell. Good prediction accuracies are obtained for the buckling load and displacement for all three analyses. The scaling methodology neglects several phenomena

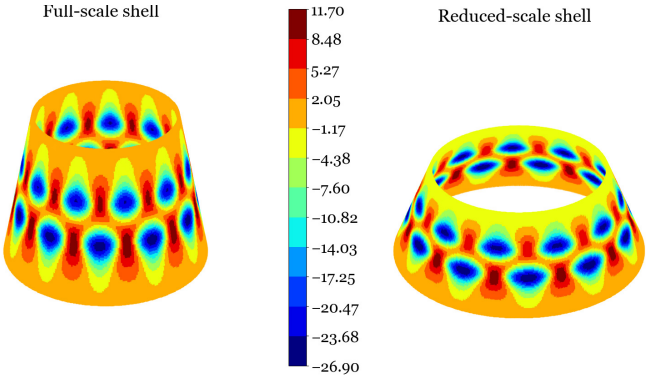

Figure 7.10: Nondimensional radial displacement comparison for the full-scale quasi-isotropic composite shell and its reduced-scale configuration ($U = 5121$).

to simplify the procedure, such as the flexural anisotropy and the presence of imperfections. Inclusion of these phenomena in the comparison shows that they affect the prediction accuracy, but they do not cause the methodology to fail. More specifically, the prediction errors created by these phenomena can partially balance each other out, such that accurate predictions are obtained.

The deformation shapes and stiffness were also accurately predicted. The nondimensional radial displacements are similar as well, but less accurate than the buckling load and displacement. This is explained by the presence of the imperfection, the membrane prebuckling assumption, and the fact that the comparison is made in the postbuckling regime, which is not taken into account in the methodology.

The bottom diameter of configuration C.ii is too large to fit in common test equipment. There is a difficult balance between the test equipment constraints and the requirement on flexural anisotropy. If one wishes to obtain a small reduced-scale shell, the thickness has to be scaled accordingly. As a result, the reduction in size depends on the size and laminate of the full-scale shell, as well as the limitations from test equipment. To have negligible flexural anisotropy, there must be sufficient plies, thus requiring a larger thickness and consequently a larger geometry. The application in this chapter shows that the design space of the reduced-scale shell is heavily limited by these contradicting requirements.

Finally, the full-scale layup is very thick (56 layers) and therefore not very lightweight. A sandwich laminate, as the original SLS USA structure has, is more lightweight and thus a more realistic design.

Chapter 8

Scaling of Sandwich Composite Conical Shell

The application of the scaling methodology to a quasi-isotropic composite in the previous chapter was successful. Nevertheless, it was not the original structure that was being scaled, but a thick, monolithic composite equivalent. The original structure, as discussed in reference [20], is a sandwich composite conical shell. The scaling of the original structure is investigated in this chapter. The designs of the full-scale and reduced-scale shells are first explained. Next, the buckling behavior is evaluated, followed by the nondimensional comparison. The effect of larger imperfections is discussed afterwards and the chapter is ended with concluding remarks.

8.1 Conical Shell Designs

First, the designs of the full-scale and reduced-scale conical shells are discussed. Several reduced-scale shells are designed using the methodology from section 3.6.

8.1.1 Full-Scale Conical Shell Description

The SLS USA is analyzed again, now with the original sandwich stacking sequence taken from reference [20]. In the paper, various core thicknesses and facesheet layups are considered. Here, it is decided to use the one with a 1 inch (i.e. 25.4 mm) core and with a quasi-isotropic facesheet layup, $[45/90/\text{-}45/0]_S$. For the core, aluminum honeycomb is used with the properties given in Table 4.6. The facesheets are made of IM7/8552 carbon fiber, detailed in Table 4.4. The structure details are given in Table 8.1.

8.1.2 Reduced-Scale Conical Shell Design

Similar to the reduced-scale shells in chapter 7, there are many options for the design of the reduced-scale conical shell. Isotropic and monolithic composite designs are considered here as well. For the former, aluminum alloy 2024-T4 is assumed to be used. For the latter, the same material is used as for the facesheets of the full-scale shell. The layup type is still to be

decided. Although the full-scale shell is a sandwich shell, this layup type is not considered for the reduced-scale shell. To obtain small reduced-scale conical shells, large reductions in core thickness are required, which may lead to unproducible designs.

Imposed Limitations and Layup Designs

For the reduced-scale shell designs, the same approach is used as for the quasi-isotropic shell of chapter 7. To reduce the number of possible stacking sequences, the limitations listed in subsection 7.1.2 are imposed. This results in the following four designs.

A. **Same layup basis as the full-scale shell, but without the core.** The ply group [45/90/-45/0] is used as a layup basis. It is opted to use the same layup as the full-scale shell, but leaving out the core. This results in a $[45/90/\text{-}45/0]_{S^2}$ layup. The symmetry and balance requirements are satisfied. The flexural anisotropy parameters and the size of the shell are checked later.

B. **$[\boldsymbol{\theta}/\text{-}\boldsymbol{\theta}]_S$ layup.** This layup considers one variable ply angle. It is the thinnest layup which satisfies the symmetry and balance requirements. Logically, this will also result in a small geometry. Priority is thus given to the size constraints, rather than the negligible flexural anisotropy.

C. **$[\boldsymbol{\theta}/\text{-}\boldsymbol{\theta}]_{mS}$ layup.** This layup also considers only one variable ply angle. The symmetry and balance requirements are satisfied. Compared to configuration B, it is aimed with this configuration to reduce the flexural anisotropy parameters as much as possible, while still complying with the size constraints. The value of m is used to balance the effects of these two limitations.

D. **Isotropic.** This shell automatically satisfies the symmetry, balance and flexural anisotropy requirements. The size is chosen such that the reduced-scale shell fits in common test equipment.

The four design options above are explored. The scaling methodologies in Figure 3.5 and Figure 3.6 are used for the isotropic and composite shells, respectively. The step-by-step application procedure is similar to the one given in subsection 7.1.2. For configuration A, the layup is already fixed, so step 2 of the methodology is omitted. Therefore, μ and β are not used for the reduced-scale design. For configuration C, it is observed that as m increases, the thickness increases, such that the reduced-scale size increases. At the same time, the flexural anisotropy parameters become smaller with respect to the other flexural parameters for increasing m. As a result, the size constraints from test equipment and the flexural anisotropy requirement pose contradicting demands on the reduced-scale design. The value of m is maximized, thus minimizing the flexural anisotropy, while still complying with the size constraints. For the isotropic reduced-scale shell, the thickness is chosen to measure 2 mm, from which the other parameters are derived. This results in a shell which complies with common test equipment constraints.

Final Reduced-Scale Shell Designs

The reduced-scale designs are summarized in Table 8.1. All shells fit in typical lab test equipment. Note that for configurations B and C, two ply angles θ were found in step 2.

To limit the computational effort, it is decided to only analyze configurations B.i and C.i, so configurations B.ii and C.ii are discarded. They have a larger cone angle than the full-scale shell. This has already been analyzed in chapter 7, so now the opposite is examined.

Table 8.1: Geometry description of the full-scale sandwich conical shell and its reduced-scale configurations.

	Cone angle α [deg]	**Length L [mm]**	**Small radius R_1 [mm]**	**Large radius R_2 [mm]**	**Stacking sequence [deg]**
FS	15	4996	2910	4203	$[45/90/\text{-}45/0]_S$ and $t_{\text{core}} = 25.4$ mm
RS A	15	305	178	257	$[45/90/\text{-}45/0]_{S^2}$
RS B.i	8	140	44	140	$[15/\text{-}15]_S$
RS B.ii	29	46	50	72	$[75/\text{-}75]_S$
RS C.i	8	841	263	380	$[15/\text{-}15]_{6S}$
RS C.ii	29	228	249	360	$[75/\text{-}75]_{5S}$
RS D	15	216	126	182	Isotropic, $t = 2$ mm

8.2 Buckling Analyses

The full-scale conical shell and the four remaining reduced-scale shells are first analyzed with the semi-analytical solution. Based on these results, two configurations are selected to be modeled in finite element software.

8.2.1 Semi-analytical Solution

The semi-analytical solution, like the scaling methodology, does not account for transverse shear effects, which may be significant for sandwich shells due to their compliant core. Nonetheless, the solution is used for the full-scale conical shell, because it gives an indication of the methodology accuracy within the limitations of its assumptions. The core is treated as a ply. The results are given in Table 8.2, together with the flexural anisotropy parameters. The buckling mode is identically predicted by the full-scale shell and by configurations A, B.i, and C.i. Configuration D predicts a different mode, which is equal to the second mode predicted for the full-scale shell. Furthermore, the second buckling mode of configuration D is equal to the first mode of the full-scale shell. These modes are within 0.01% of each other for both shells. A small difference in scaling parameters could have caused this.

All reduced-scale designs correctly predict the buckling load. Configuration A is less accurate than the other shells, but the result is still acceptable. This may be caused by neglecting the orthotropy parameters μ and β in the design, as the layup was already fixed a priori. The flexural anisotropy parameter ratios are different for all shells. For configurations A, B.i, and C.i, they are not negligible. Based on these results, it is decided to numerically model configurations A and C.i. Configuration A is chosen because it performs well and because it remains an interesting option due to the stacking sequence. Configuration B.i is very small, because the layup is very thin, but this causes the flexural anisotropy parameters to be very large. Therefore, configuration C.i is opted over option B.i: the flexural anisotropy

parameters are smaller and it still complies with constraints from common test equipment. Although configuration D predicts the buckling load accurately, the option is less interesting because it is an isotropic shell.

Table 8.2: Semi-analytical solution and flexural anisotropy results for the different configurations. The difference in K_{xx} with the full-scale value is given between brackets. Note that $i, j = 1, 2$.

Config.	Buckling load [kN]	Buckling mode (m, n)	Nondimensional buckling load K_{xx}	$\frac{D_{16}}{\min(D_{ij})}$	$\frac{D_{26}}{\min(D_{ij})}$
FS	27596	(7,0)	399.8	0.08%	0.08%
RS A	1618	(7,0)	384.7 (-3.78%)	19.3%	19.3%
RS B.i	66.49	(7,0)	401.0 (+0.296%)	226%	23.7%
RS C.i	2393	(7,0)	399.4 (-0.100%)	37.6%	3.95%
RS D	1054	(2,7)	400.1 (+0.0750%)	0.0%	0.0%

8.2.2 Linear Eigenvalue Analysis

The full-scale shell and configurations A and C.i are modeled with a linear eigenvalue analysis. The core of the full-scale shell is modeled as a ply. Mesh convergence studies are performed, resulting in mesh sizes of 50 mm, 3 mm, and 7 mm for the full-scale shell, configuration A, and configuration C.i, respectively. The analysis results are given in Table 8.3. The nondimensional buckling load and displacement predictions are accurate for both shells. The observed discrepancies may be caused by differences in flexural anisotropy and transverse shear stiffness, next to the differences in scaling parameters. The buckling modes are different from the predicted linear buckling mode of the full-scale shell, see Figure 8.1. Because both configurations give good predictions for the buckling load and displacement, they will both be analyzed with a nonlinear analysis, together with the full-scale shell. The three shells are visualized in Figure 8.2 to give an idea of the difference in size.

Table 8.3: Linear eigenvalue results for the different configurations. The difference in K_{xx} and U with the full-scale value is given between brackets.

Config.	Buckling load [kN]	Buckling displ. [mm]	Nondimensional buckling load K_{xx}	Nondimensional buckling displ. U
FS	25825	37.3	374.2	901.2
RS A	1544	2.23	367.1 (-1.90%)	881.4 (-2.20%)
RS C.i	2336	1.90	389.8 (+4.18%)	920.2 (+2.11%)

8.2.3 Implicit Dynamic Analysis

The three shells are modeled with a nonlinear analysis. A load plateau is observed for all three shells, so an eigenmode imperfection with an amplitude of 1% of the thickness is applied. Based on the sensitivity analysis in subsection 4.3.4, the minimum number of increments is set equal to 250 with an increment size of 0.01 s. To this end, displacement rates of 19.2 mm/s, 1.14 mm/s and 0.976 mm/s are used for the full-scale shell and configurations A and C.i, respectively. The load-displacement curves are shown in Figure 8.3. The buckling loads and displacements of all analyses are summarized in Table 8.4. For the full-scale shell, the

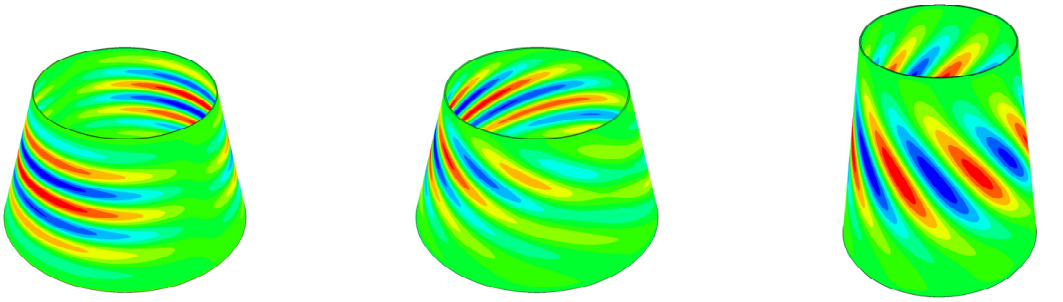

(a) Full-scale shell. **(b)** Configuration A. **(c)** Configuration C.i.

Figure 8.1: First eigenmode of the full-scale sandwich composite conical shell and its reduced-scale configurations, showing radial displacement.

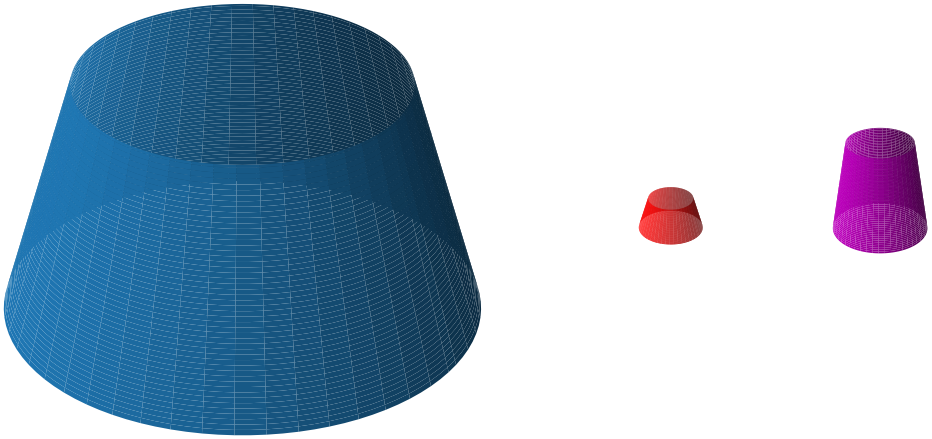

Figure 8.2: Visualization of the full-scale (blue, left), reduced-scale A (red, middle) and reduced-scale C.i (pink, right) conical shells. Full-scale is 65x smaller than in reality, reduced-scale shells are 30x smaller than in reality.

knockdown factor KDF=0.955. For configuration A, KDF=0.903 and for configuration C.i, KDF=0.866. This result is in agreement with Orifici and Bisagni [94] for cylindrical shells, who found that sandwich cylindrical shells are less imperfection sensitive than monolithic composite cylindrical shells. In addition, it is known that the imperfection sensitivity is also affected by the length-to-radius ratio: longer shells, such as configuration C.i, experience less stiffening effect from the boundary conditions and are consequently more imperfection sensitive [6]. Next, it is noted that the applied eigenmode imperfection is different for the full-scale shell than for the reduced-scale shells. Shells are not equally sensitive to all eigenmode imperfections, such that different knockdown factors can be found for different eigenmodes with the same amplitude [6]. Finally, the stacking sequence is also known to affect the imperfection sensitivity [96, 97]. These findings may explain the difference in knockdown factors between configurations A and C.i.

The difference in buckling load between the linear prediction and the nonlinear prediction with a 1% thickness imperfection is large for all shells analyzed in this research. The knockdown factors are consistently found to be around 0.900, except for the sandwich conical shell. Although this result is in agreement with literature [6,94,97], an additional check is performed.

Configuration A is modeled with explicit dynamic analyses, once without imperfections and once with the 1% eigenmode imperfection. The load plateau is not expected to occur for this analysis type. An analysis of 0.5 s is run with a displacement rate of 5 mm/s, applied with a smooth step in the first 0.005 s. No mass scaling is applied. It is checked if the kinetic energy remains below 10% of the internal strain energy to ensure that the dynamic effects remain small [45]. For the perfect shell, the knockdown factor measures KDF=0.973. The load-displacement curve perfectly follows the curve of the implicit dynamic analysis up to buckling. For the imperfect shell, a knockdown factor of KDF=0.904, as good as identical to the implicit result. The stiffness and buckling displacement also agree perfectly. For both analyses, the ratio of kinetic to internal energy does not exceed 10%, except during the first instances of loading and after buckling. The results are therefore considered verified.

Table 8.4: Nonlinear buckling load and displacement for the full-scale sandwich composite conical shell and its reduced-scale configurations.

Config.	Buckling load P_{cr} [kN]	Buckling displ. u_{cr} [mm]
FS	24673	36.4
RS A	1394	2.04
RS C.i	2071	1.71

8.3 Failure Assessment

It is checked if failure occurs after buckling. For the full-scale shell, core failure is evaluated by checking if the critical shear crimping load is higher than the buckling load using Equation 4.8. Shear crimping is expected at a load of 69124 kN, which is well above the buckling load of 24673 kN. Additional analysis should be performed to ensure that no other sandwich failure mechanisms, such as facesheet wrinkling and dimpling [93], occur prior to buckling.

The maximum failure indices right before buckling are summarized in Table 8.5 per criterion. For the full-scale conical shell, failure is almost occurring; the first four criteria are close to, but below, 1. The Hashin criterion predicts a lower index. Four out of five criteria predict ply 4 to be the critical ply (the inner 0° ply), whereas the Tsai-Hill criterion predicts the highest failure index in the innermost ply (45°). The failure index in ply 4, however, is only 1% lower than in the critical ply. If this shell would be manufactured, material failure has to be investigated in more detail. One could, for example, use multiple SC8R elements through the thickness in order to capture the transverse shear effects in more detail. For the scope of the current analysis, this is not relevant and not further examined. For reduced-scale configuration A, the indices are also high, but well below 1, with a maximum of 0.910. For configuration C.i, failure is definitely not expected prior to buckling. The maximum failure index for this shell is 0.569. In line with the previously analyzed shells, the maxima of the three shells occur near the top edge, at the first meridional deformation wave. This is the location of maximum radial displacement. Typically, pad-up reinforcements are added here to avoid preliminary failure at this location.

The maximum strains for the four inner plies of the three conical shells are given in Table 8.6, because these plies are the most critical. It can be seen that the critical ply is different for each shell, which is due to the different layups. The full-scale shell and configuration A have

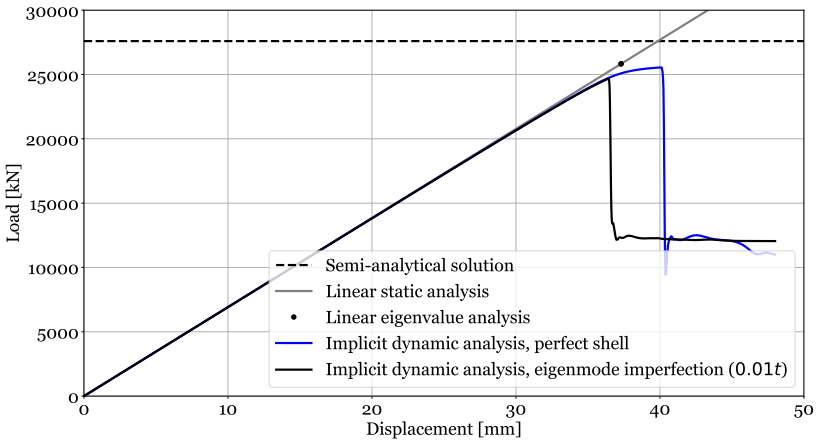

(a) Full-scale conical shell.

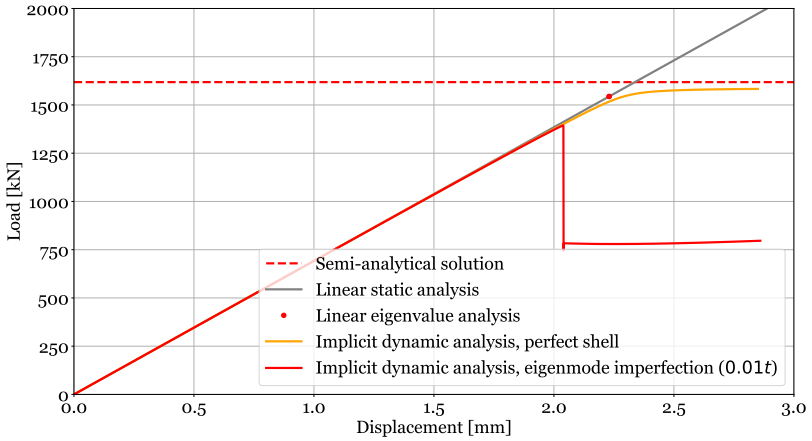

(b) Reduced-scale conical shell, configuration A.

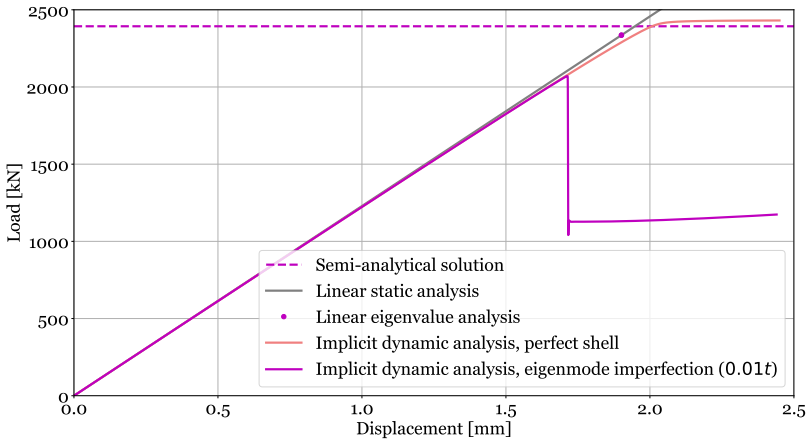

(c) Reduced-scale conical shell, configuration C.i.

Figure 8.3: Load-displacement curves of the sandwich composite conical shells.

Table 8.5: Maximum failure indices at incipient buckling for the full-scale sandwich composite conical shell and its reduced-scale configurations.

Failure criteria	FS	RS A	RS C.i
Max strain	0.936 (ply 4, 0°)	0.852 (ply 1, 45°)	0.536 (ply 2, −15°)
Max stress	0.934 (ply 4, 0°)	0.852 (ply 1, 45°)	0.450 (ply 24, 15°)
Tsai-Hill	0.952 (ply 1, 45°)	0.910 (ply 1, 45°)	0.500 (ply 2, −15°)
Tsai-Wu	0.987 (ply 4, 0°)	0.858 (ply 4, 0°)	0.569 (ply 1, 15°)
Hashin	0.873 (ply 4, 0°) fiber compression	0.677 (ply 4, 0°) fiber compression	0.228 (ply 24, 15°) matrix tension

a similar strain distribution, because they have a similar layup. The strains in configuration C.i are different because of the different geometry and layup.

The critical strain in the full-scale shell occurs in the fiber direction of a 0° ply, similar to the full-scale shell in chapter 7. The same explanation as given in section 7.3 holds. For configuration A, the shear strain in the inner 45° ply is critical. The positive sign of the strain indicates that this ply is critical due to the circumferential tension caused by the Poisson's effect. The critical ply of configuration C.i is a −15° ply. The transverse, matrix-dominated direction of this ply mainly experiences tension, against which the matrix is not very effective. This is also the critical damage type according to the Hashin criterion. The strain plots of the plies with the critical strain are visualized in Figure 8.4. The critical location can be identified near the top edge for all three shells, based on the critical strain direction plot. This is the location of the first meridional wave where the maximum radial displacement occurs. In addition, the eigenmode imperfection shape can be recognized in the strain distributions.

Table 8.6: Maximum strain values at incipient buckling in the four inner plies for the full-scale sandwich composite conical shell and its reduced-scale configurations.

	FS			
	θ [deg]	ϵ_{11} [$\mu\epsilon$]	ϵ_{22} [$\mu\epsilon$]	ϵ_{12} [$\mu\epsilon$]
Ply 1	45°	-3347	-3304	15473
Ply 2	90°	4618	-10827	-840
Ply 3	−45°	-3276	-3320	-15412
Ply 4	0°	**-10766**	4617	830
	RS A			
	θ [deg]	ϵ_{11} [$\mu\epsilon$]	ϵ_{22} [$\mu\epsilon$]	ϵ_{12} [$\mu\epsilon$]
Ply 1	45°	-4045	-4672	**14607**
Ply 2	90°	3976	-10267	-2993
Ply 3	−45°	-4117	-3688	-13782
Ply 4	0°	-9475	3941	2483
	RS C.i			
	θ [deg]	ϵ_{11} [$\mu\epsilon$]	ϵ_{22} [$\mu\epsilon$]	ϵ_{12} [$\mu\epsilon$]
Ply 1	15°	-2703	3611	4021
Ply 2	−15°	-2644	**3660**	-3878
Ply 3	15°	-2591	3591	3911
Ply 4	−15°	-2524	3642	-3777

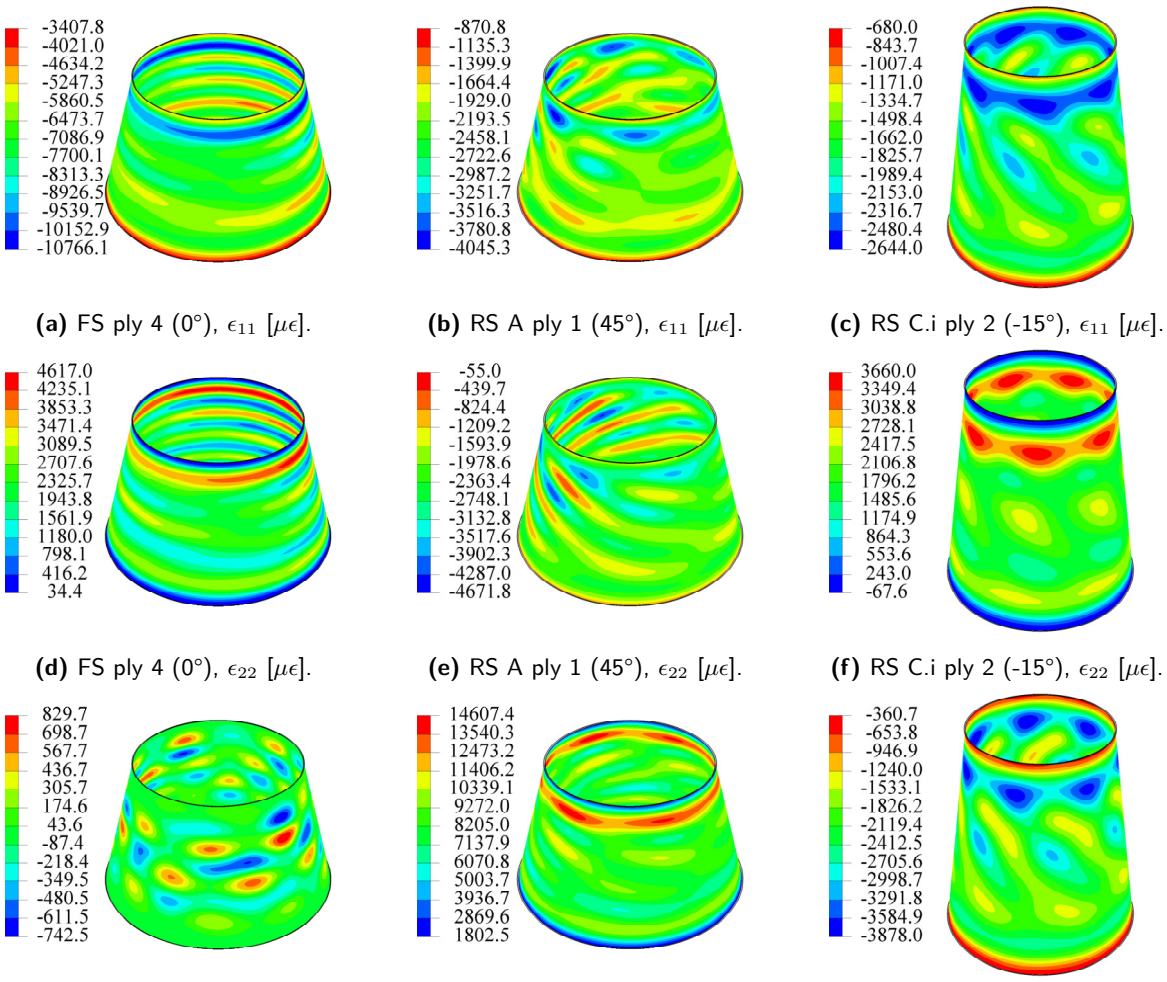

(a) FS ply 4 (0°), ϵ_{11} [$\mu\epsilon$]. **(b)** RS A ply 1 (45°), ϵ_{11} [$\mu\epsilon$]. **(c)** RS C.i ply 2 (-15°), ϵ_{11} [$\mu\epsilon$].

(d) FS ply 4 (0°), ϵ_{22} [$\mu\epsilon$]. **(e)** RS A ply 1 (45°), ϵ_{22} [$\mu\epsilon$]. **(f)** RS C.i ply 2 (-15°), ϵ_{22} [$\mu\epsilon$].

(g) FS ply 4 (0°), ϵ_{12} [$\mu\epsilon$]. **(h)** RS A ply 1 (45°), ϵ_{12} [$\mu\epsilon$]. **(i)** RS C.i ply 2 (-15°), ϵ_{12} [$\mu\epsilon$].

Figure 8.4: Strains in the critical plies at incipient buckling for the sandwich composite conical shells.

8.4 Comparison of the Full-Scale and Reduced-Scale Conical Shells

The three shells have been analyzed, so now the results can be compared using the nondimensional parameters. First, the scaling parameters are compared. Next, the nondimensional load-displacement curves are analyzed. Finally, the deformation shapes are examined.

8.4.1 Scaling Parameters

The values of the scaling parameters of each conical shell are given in Table 8.7. For configuration A, the largest differences occur for the bending parameter α_b and for flexural orthotropy parameter β. This makes sense, because the stacking sequence of configuration A is not designed using parameters μ and β. The consequence hereof is mostly visible in the flexural parameters, because flexural stiffnesses have a cubic dependency on the distance to the mid-surface, thus exaggerating the effect of the mismatch, compared to membrane parameters. For configuration C.i, the largest discrepancies are observed for the orthotropy parameters,

which are only affected by the layup. This error is caused by the rounding of the ply angle θ to an integer value. If $\theta = 14.6°$ instead of $\theta = 15°$, the errors for μ and β would be below 0.2%. This accuracy in ply angle is, however, not realistic for current manufacturing techniques.

Table 8.7: The nondimensional scaling parameters of the full-scale sandwich composite conical shell and its reduced-scale configurations.

	Membrane parameter α_m		**Bending parameter α_b**	
	$z_1 = 0$	$z_1 = 1$	$z_1 = 0$	$z_1 = 1$
FS	0.5825	0.8413	0.5824	0.8412
RS A	0.5836	0.8424	0.5606	0.8093
Δ	(+0.196%)	(+0.136%)	(-3.73%)	(-3.79%)
RS C.i	0.5882	0.8500	0.5882	0.8500
Δ	(+0.988%)	(+1.04%)	(+1.00%)	(+1.05%)
	Batdorf-Stein eq. parameter Z_2		**Membrane orth. parameter μ**	**Flexural orth. parameter β**
	$z_1 = 0$	$z_1 = 1$	$z_1 \epsilon [0, 1]$	$z_1 \epsilon [0, 1]$
FS	57.41	82.93	1.001	1.000
RS A	57.49	82.98	1.000	1.103
Δ	(+0.130%)	(+0.0702%)	(-0.0569%)	(+10.3%)
RS C.i	57.32	82.83	0.9432	1.031
Δ	(-0.169%)	(-0.121%)	(-5.73%)	(+3.10%)

8.4.2 Nondimensional Load-Displacement Curves

Next, the buckling loads and displacements are compared. Figure 8.5 shows the nondimensional load-displacement curves. The buckling values are summarized in Table 8.8. It can be seen that configuration A is not very accurate, with underestimations of 7.34% and 8.47% for the buckling load and displacement, respectively. Configuration C.i is more accurate, with underestimations of 3.33% for the load and 5.83% for the displacement. The stiffness, however, is predicted more accurately by configuration A than by configuration C.i.

To explain these differences, it is important to also look at the predictions by the semi-analytical solution and the linear analysis. For the former solution, configuration A performed worse than the other reduced-scale shells. This is attributed to neglecting the orthotropy parameters μ and β during the design, which propagated to errors in the bending parameter α_b as well. Configuration C.i gave a very accurate prediction using this solution. The linear eigenvalue prediction from configuration A was more accurate than the semi-analytical solution, but still underestimating. Configuration C.i performed worse, overestimating the buckling load and displacement of the full-scale shell. This could be caused by the inclusion of the flexural anisotropy, which is not negligible for either of the reduced-scale shells, in contrast to the full-scale shell. The transverse shear effects, which may be significant for the sandwich shell, can also be a source of discrepancy.

The implicit dynamic analysis includes nonlinearity, as well as an eigenmode imperfection due to the loading plateau. The load-displacement graphs show large reductions in buckling load due to the imperfection. Both reduced-scale shells underestimate the buckling load of the full-scale shell. When compared to the linear results, this implies a difference in imperfection

sensitivity. Because configuration A was already underestimating the buckling load, the accuracy got worse. For configuration C.i, the linear overestimation was compensated by the large imperfection sensitivity, such that the nonlinear prediction is slightly underestimating the buckling load.

Table 8.8: Comparison of nondimensional buckling load, displacement and stiffness for the full-scale sandwich composite conical shell and its reduced-scale configurations.

		Buckling load K_{xx}		**Buckling displ.** U	**Stiffness** K_{xx}/U	
		$z_1 = 0$	$z_1 = 1$	$z_1 \epsilon [0, 1]$	$z_1 = 0$	$z_1 = 1$
Semi-analytical solution	FS	399.8	577.5	n.a.	n.a.	n.a.
	RS A	384.7	555.4	n.a.	n.a.	n.a.
	Δ	(-3.78%)	(-3.83%)			
	RS C.i	399.4	577.2	n.a.	n.a.	n.a.
	Δ	(-0.100%)	(-0.0522%)			
Eigenvalue analysis	FS	374.2	540.5	901.2	0.4152	0.5997
	RS A	367.1	529.9	881.4	0.4165	0.6012
	Δ	(-1.90%)	(-1.96%)	(-2.20%)	(+0.313%)	(+0.250%)
	RS C.i	389.8	563.3	920.2	0.4236	0.6122
	Δ	(+4.18%)	(+4.22%)	(+2.11%)	(+2.02%)	(+2.08%)
Implicit dynamic analysis	FS	357.5	516.3	880.3	0.4061	0.5865
	RS A	331.4	478.4	805.7	0.4113	0.5938
	Δ	(-7.30%)	(-7.34%)	(-8.47%)	(+1.28%)	(+1.24%)
	RS C.i	345.6	499.4	829.0	0.4169	0.6024
	Δ	(-3.33%)	(-3.27%)	(-5.83%)	(+2.66%)	(+2.71%)

8.4.3 Deformation Shapes

The semi-analytical solution predicted a (7,0) buckling mode for the three shells. It was already discussed in subsection 8.2.2 that the linear eigenmodes were different for the reduced-scale shells compared to the full-scale shell. The reduced-scale shells have a skewed and twisted deformation shape, such that the waves are oriented diagonally across the conical shells. The deformation waves of the full-scale shell are oriented horizontally.

Next, the deformation shapes during the loading regime are analyzed. Figure 8.6, Figure 8.7 and Figure 8.8 show the deformation shapes of the full-scale and configurations A and C.i at three points during loading. It can be seen that the prebuckling and buckling shapes are heavily influenced by the eigenmode imperfection. Because the first eigenmodes are different, the prebuckling and buckling deformation shapes are different. The postbuckling deformation shape of the full-scale shell shows an irregularity: there is a location with only one meridional half-wave, instead of two, which is also more radially displaced than all the others. This makes it difficult to express the deformation shape in an (m, n) format. Configuration A and C.i both have a (2,7) deformation shape. The full-scale shell has a similar shape, except for the irregularity. This difference can also be recognized in the load-displacement graph: configuration A and C.i converge to the same postbuckling load, while the full-scale postbuckling load is slightly lower.

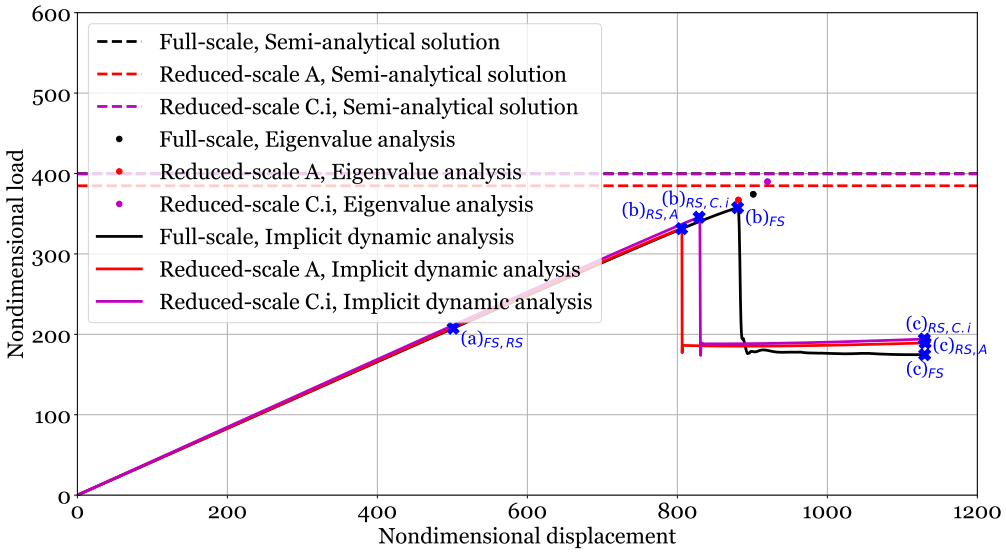

Figure 8.5: Nondimensional load-displacement curve of the full- and reduced-scale sandwich composite conical shells, using K_{xx} at $z_1 = 0$.

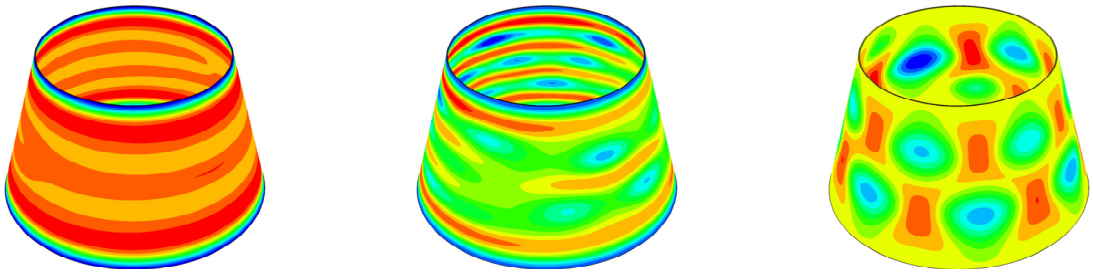

(a) Before buckling, for $U = 500$. **(b)** At buckling, for $U = 880$. **(c)** After buckling, for $U = 1130$.

Figure 8.6: Deformation shapes (radial displacement) of the full-scale sandwich composite conical shell at the instances indicated in Figure 8.5.

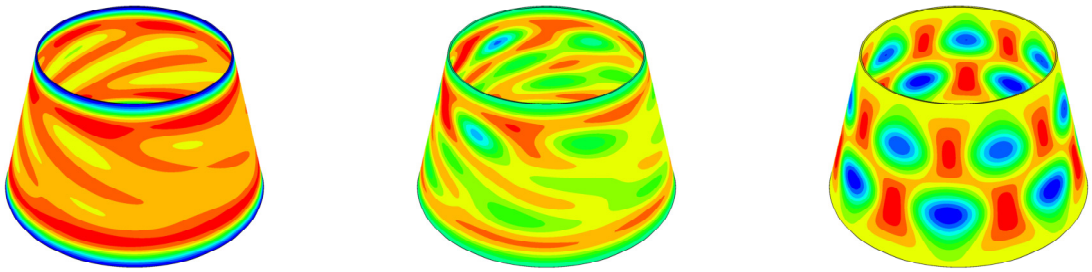

(a) Before buckling, for $U = 500$. **(b)** At buckling, for $U = 806$. **(c)** After buckling, for $U = 1130$.

Figure 8.7: Deformation shapes (radial displacement) of the reduced-scale configuration A conical shell at the instances indicated in Figure 8.5.

The radial displacement in the postbuckling regime is compared as well. The dimensional results are shown in Figure 8.9. The ratios of maximum to minimum radial displacements

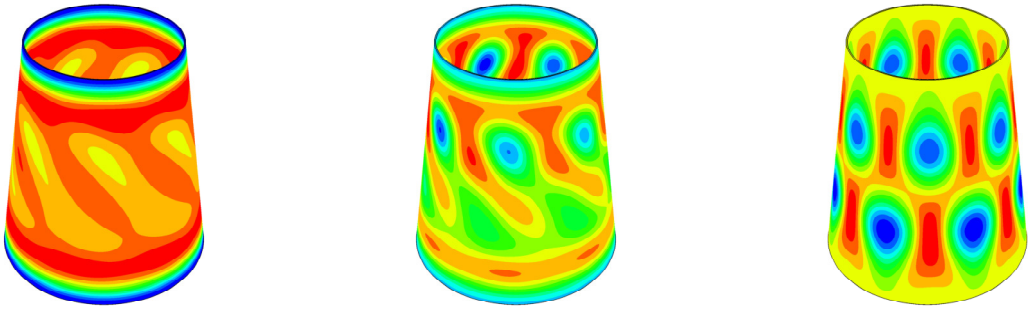

(a) Before buckling, for $U = 500$. **(b)** At buckling, for $U = 829$. **(c)** After buckling, for $U = 1130$.

Figure 8.8: Deformation shapes (radial displacement) of the reduced-scale configuration C.i conical shell at the instances indicated in Figure 8.5.

are equal to -0.464 for all shells. The nondimensional radial displacement is compared in Figure 8.10. The minimum and maximum values are given in Table 8.9. The local dimple in the full-scale shell is much larger than the waves of the reduced-scale shells. Consequently, there are large discrepancies between the nondimensional radial displacements, up to 31.5%. The overall distribution is similar for all three shells. Configuration C.i shows slightly more deformation near the top edge than the full-scale shell and configuration A.

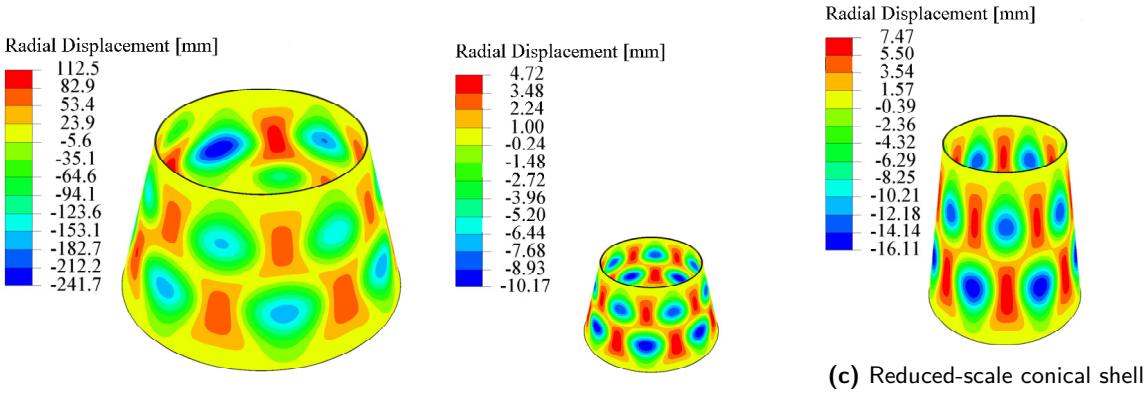

(a) Full-scale conical shell. **(b)** Reduced-scale conical shell A. **(c)** Reduced-scale conical shell C.i.

Figure 8.9: Comparison of the dimensional postbuckling deformation shape. Reduced-scale shells A and C.i are respectively 8x and 6.5x enlarged compared to the full-scale shell for visibility.

Table 8.9: Comparison of the minimum and maximum nondimensional radial displacement for the full-scale sandwich composite conical shell and its reduced-scale configurations.

	Minimum radial displacement $W_{\min}$	**Maximum radial displacement $W_{\max}$**	**Ratio $W_{\max}/W_{\min}$**
FS	-18.1	7.87	-0.435
RS A	-12.4	5.47	-0.441
Δ	(-31.5%)	(-30.5%)	(+1.38%)
RS C.i	-12.5	5.69	-0.455
Δ	(-31.4%)	(-27.7%)	(+4.69%)

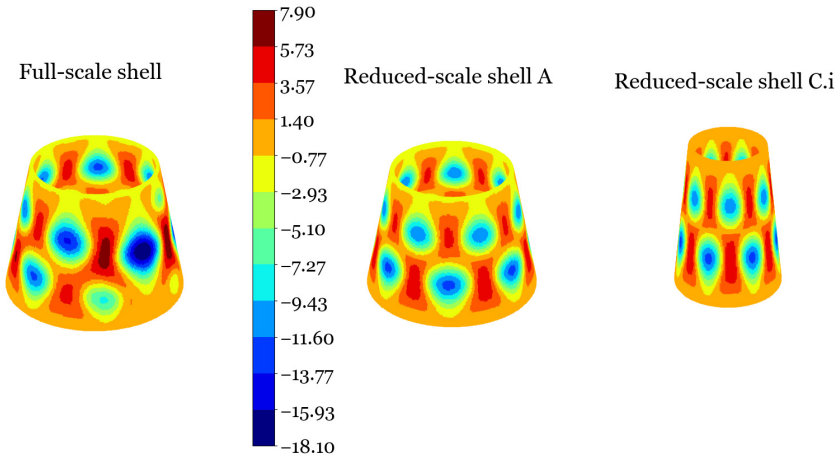

Figure 8.10: Nondimensional radial displacement comparison for the sandwich composite shells ($U = 1130$).

8.5 Effect of Larger Eigenmode Imperfections

The discrepancies between the full-scale shell and its reduced-scale configurations were partially attributed to a difference in imperfection sensitivity. This is now further investigated by applying larger eigenmode imperfections, namely with an amplitude of 10% and 50% of the shell thickness. The shells are then analyzed using the implicit dynamic analysis with the same settings as for the 1% eigenmode imperfection analyses. The nondimensional load-displacement curves are visualized in Figure 8.11. The knockdown factors and the nondimensional buckling values are given in Table 8.10. As expected, the prebuckling stiffness and the buckling load reduce for increasing imperfection amplitude.

For the 10% imperfection, the prediction accuracy of the two reduced-scale configurations is better than for the 1% imperfection. The postbuckling path of the shells, however, is different for this imperfection amplitude and they do not converge to the same postbuckling load. The load-displacement curves of the shells with a 50% imperfection do not show typical buckling behavior in the form of a load drop. The reduced-scale configurations still show a slight increase in load up to the end of the analysis. As a result, comparing the nondimensional displacement and stiffness upon maximum load does not quantify the prediction accuracy. This is why these values are in italic face in Table 8.10. When solely looking at the curves in Figure 8.11, it can be seen that the behavior of the three shells is similar up to a displacement of approximately $U = 550$. Beyond this point, the curves separate. The maximum load and the knockdown factor, however, can still be compared. The prediction accuracy of configuration A is better for the 50% imperfection than for the 1% imperfection. For configuration C.i, the prediction accuracy is lower, with a difference of 11.2% for the buckling load. It is also remarkable that for this imperfection amplitude, the imperfection sensitivity of the full-scale sandwich shell is larger than the reduced-scale monolithic shells in terms of knockdown factor.

This analysis shows that imperfections and the shells' sensitivity to them affects the prediction accuracy of the reduced-scale shells. To understand this better, it is important to also know the nonlinear prediction accuracy without imperfections. This can be investigated through

other analysis types, such as the explicit dynamic analysis. In addition, the effects of other imperfections, such as measured imperfections should be analyzed.

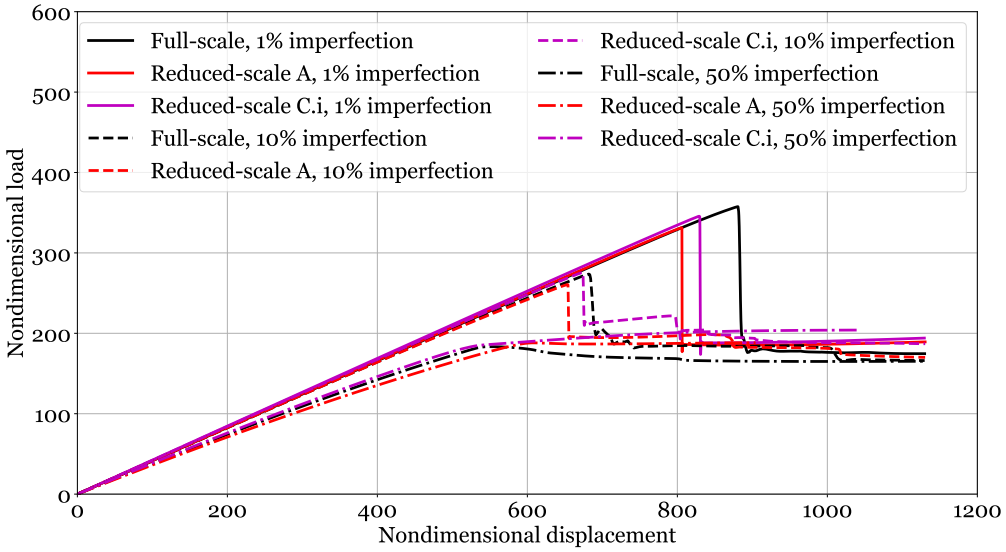

Figure 8.11: Nondimensional load-displacement curve of the full-scale sandwich conical shell and its reduced-scale configurations for different imperfection amplitudes, using K_{xx} at $z_1 = 0$.

Table 8.10: Comparison of nondimensional buckling load, displacement and stiffness for the full-scale sandwich composite conical shell and its reduced-scale configurations.

		KDF	**Buckling load K_{xx}**	**Buckling displ. U**	**Stiffness K_{xx}/U**
10% eigenmode imperfection	FS	0.732	273.7	682.1	0.4013
	RS A	0.710	260.7	653.5	0.3989
	Δ	(-3.01%)	(-4.75%)	(-4.19%)	(-0.598%)
	RS C.i	0.707	275.5	672.9	0.4094
	Δ	(-3.42%)	(+0.658%)	(-1.35%)	(+2.02%)
50% eigenmode imperfection	FS	0.490	183.4	552.0	0.3322
	RS A	0.513	188.3	*904.3*	*n.a.*
	Δ	(+4.69%)	(+2.67%)	*(+63.8%)*	
	RS C.i	0.523	204.0	*1049*	*n.a.*
	Δ	(+6.73%)	(+11.2%)	*(+90.0%)*	

8.6 Concluding Remarks

This chapter discusses the application of the scaling methodology to a sandwich conical shell with quasi-isotropic facesheets. Overall, the application to a sandwich conical shell can be considered successful. Out of six reduced-scale designs, two were selected to be analyzed in detail. Failure is expected to occur after buckling for all shells, but for the full-scale shell, the failure indices are close to 1. It is advised to investigate this in more detail before the shell would be manufactured, together with additional analyses to assess sandwich failure.

Configuration A has the same layup as the full-scale shell, but without the core. The prediction by the semi-analytical solution is good, but not excellent. The discrepancy is attributed to neglecting parameters μ and β during the design. The linear results are accurate, except for the mode shape. The nonlinear analysis yields a very accurate stiffness prediction, but discrepancies of 7.34% and 8.47% in buckling load and displacement compared to the full-scale shell. This is attributed to a combination of neglecting the orthotropy parameters in the design, the non-negligible flexural anisotropy and the difference in imperfection sensitivity between sandwich and monolithic shells. The transverse shear effects could also influence the results, because the full-scale shell has a compliant core, in contrast to the reduced-scale shell. Inclusion of the flexural anisotropy and transverse shear effects in the methodology could improve the accuracy. At the same time, they will impose additional constraints, which can complicate the reduced-scale design. It is therefore recommended to quantify the effects first, such that accuracy improvements can be estimated. Next, the deformation shapes differ throughout the analyzed regime due to the shape difference in the eigenmode imperfection. The postbuckling deformation shape was similar, except for the local dimple for the full-scale shell. This also causes the radial displacement to be predicted with low accuracy. The results for the larger imperfections were better than for the 1% imperfection. This is remarkable and promising for real structures, but it also shows that it is difficult to predict how the real structures, with real imperfections, will respond. It is therefore recommended to investigate the prediction accuracy for the shells without imperfections, for example, using an explicit dynamic solver, as well as for shells with other imperfections, such as measured imperfections. This will give a more complete picture of how the imperfections affect the prediction accuracy.

Configuration C.i, which has a $[15/\text{-}15]_{6S}$ layup, predicted the semi-analytical buckling load of the full-scale shell very accurately. The linear eigenvalue analysis overestimates the buckling load, which can be caused by stiffness parameter D_{16} not being negligible, as well as by the higher transverse shear stiffness than the sandwich shell. The nonlinear analysis underestimates the buckling load of the full-scale shell again, which was explained by its high sensitivity to imperfections due to its large radius-to-length ratio and monolithic stacking sequence. The stiffness, on the other hand, is slightly overestimated, by 2.71%. The prediction accuracy for the shell with a 10% eigenmode imperfection is very good. For the 50% imperfection, the load-displacement cure was similar to the one of the full-scale shell up to $U = 550$. After this point, configuration C.i continued to withstand higher loads, in contrast to the full-scale shell. This highlights again the difficulty in predicting the influence of imperfections on the accuracy.

Chapter 9

Conclusions and Recommendations

In this thesis, the development of a scaling methodology for composite conical shell in axial compression was researched. The methodology allows to design reduced-scale shells, representative of full-scale shells, such that experimental tests can be performed on smaller structures. This is cheaper and more convenient than testing of the original large structures. The work is undertaken in a framework of collaboration between the TU Delft and the NASA Langley Research Center. The methodology was derived using the nondimensional stability equations. This approach allows to scale the buckling phenomenon as a whole and to nondimensionally compare the full-scale and reduced-scale shells straightforwardly. Here, conclusions from the research are drawn and recommendations for future work are made.

First, the dimensional governing equations were derived using the Donnell-Mushtari-Vlasov shell theory for symmetric, balanced composite conical shells with negligible flexural anisotropy. These equations were made nondimensional using the approach of Nemeth for general shells. The nondimensional coefficients of these equations were used as scaling parameters for the methodology. The scaling methodology was set up such that the reduced-scale shell properties could be determined in a sequential manner. First, the symmetric, balanced layup is determined, followed by the radius-to-length ratio, then the cone angle and finally the radius and length. A separate methodology was created for isotropic shells. Due to the simplifications in the constitutive equations, design freedom for the isotropic reduced-scale shell is achieved. As a result, one dimension can be chosen freely, from which the others are derived. For composite shells, there are more scaling parameters than reduced-scale design variables. Nevertheless, representative reduced-scale conical shells can be found by averaging the outputs from two scaling laws. If the full-scale shell has a layup with adjacent plies with the same ply angle, ply-level scaling can be applied, such that all scaling parameters are exactly satisfied. This entails that a full-scale shell with a $[\theta_n/\gamma_n/...]_S$ layup is scaled to a reduced-scale shell with a $[\theta_m/\gamma_m/...]_S$ layup made of the same material with $m < n$.

Second, the analysis and evaluation methods were elaborated upon. The geometry of the Universal Stage Adapter and the Payload Attach Fitting of the Space Launch System were used as references for the full-scale shells. The full-scale and reduced-scale shells were compared with three analyses: a semi-analytical solution, a linear eigenvalue finite element anal-

ysis, and a nonlinear implicit dynamic finite element analysis. The first solution makes the same assumptions as the scaling methodology, thus allowed to verify the methodology within the limitations of its assumptions. The eigenvalue analysis takes into account the flexural anisotropy and transverse shear effects. The nonlinear analysis allowed to evaluate the influence of prebuckling nonlinearity and of imperfections. It was also used to ensure that failure occurs after buckling and to examine the strain distributions. Not only was the scalability of the buckling load investigated, but also that of the displacement upon buckling, the deformation shape and the radial displacement.

The methodology was applied to four full-scale shells with the same geometry, but different material and stacking sequence. First, an isotropic shell and a cross-ply shell were scaled. Both satisfy all laminate requirements and scaling parameters simultaneously. Ply-level scaling was used for the latter shell. Due to the simplifications for these two shells, the methodology comes down to geometric scaling, if the same material is used for full-scale and reduced-scale shells. For the isotropic shell, the scaling factor can be chosen freely. For the ply-level scaled cross-ply shell, the scaling factor is fixed to $\frac{m}{n}$. For both shell types, the semi-analytical buckling load prediction was excellent. Small errors were caused by rounding of the reduced-scale shell dimensions to producible accuracies. The linear eigenvalue and implicit dynamic predictions were accurate in terms of buckling load and displacement; the errors were all smaller than 3.4% and 1.8% for the isotropic and cross-ply shells, respectively. Although the postbuckling behavior is not taken into account in the methodology, it was well predicted for the cross-ply shells. For the isotropic shell, small discrepancies were observed. The influence of a larger cone angle was investigated for the cross-ply shell to evaluate the assumption of mildly varying curvatures. This did not influence the prediction accuracy for any of the evaluated parameters, except for the postbuckling path and corresponding deformations.

The results for the isotropic shell and the cross-ply shell verify the methodology, but ply-level scaling cannot be used for most realistic laminates. Therefore, the methodology was applied to a quasi-isotropic composite shell and a sandwich shell. Several symmetric, balanced laminates were considered for the reduced-scale shells, from which the best performing were analyzed in detail. For the quasi-isotropic shell with layup $[45/90/-45/0]_{7S}$, a reduced-scale shell with a $[75/-75]_{S^3}$ layup was designed. It is slightly too large to fit in common test equipment, but the flexural anisotropy is negligible. For the sandwich shell with a 25.4 mm thick core, two reduced-scale shells were designed. One has the same layup as the full-scale shell, but without the core, resulting in a $[45/90/-45/0]_{S^2}$ layup. The other one has a $[15/-15]_{6S}$ layup. Both reduced-scale shells fit in common test equipment, but do not have negligible flexural anisotropy. The flexural anisotropy requirement and shell size constraints were observed to contradict each other through the thickness requirements they impose.

Because there are more constraints than design parameters, the reduced-scale shell dimensions were determined such that the errors with respect to all scaling parameters are minimized. The corresponding small discrepancies in scaling parameters propagated to the buckling behavior prediction. As a result, the semi-analytical solution predicted the buckling load of the realistic shells with a lower accuracy than for the isotropic and cross-ply shells, but still all within 4%. The linear eigenvalue results showed that the inclusion of the flexural anisotropy affects the prediction accuracy, but not to a large extent for any of the shells. For the sandwich shell, the difference in transverse shear compliance could also have influenced the results. In the nonlinear analyses, eigenmode imperfections with a 1% thickness amplitude were applied. For the quasi-isotropic shell, the difference in imperfection sensitivity actually improved the

prediction accuracy for buckling load and displacement, counteracting the effects of differences in scaling parameters and flexural anisotropy. The maximum discrepancy measured only 1.2%. The deformation shapes were also accurately predicted, even in the postbuckling regime. The radial displacement was predicted with a 4.1% error. For the sandwich shell, the difference in imperfection sensitivity was more pronounced because its reduced-scale configurations have monolithic layups, which are more sensitive to imperfections than sandwich layups. In addition, the imposed eigenmodes were different, such that the nonlinear deformation shapes and radial displacements were also wrongly predicted. The first reduced-scale shell predicted the nonlinear buckling load and displacement with a maximum error of 8.5%. The second reduced-scale shell had a maximum error of 5.8%. The stiffness, on the other hand, was predicted within 2.7% for both shells. For the sandwich shell, eigenmode imperfections with amplitudes of 10% and 50% of the thickness were also applied. For the 10% imperfection, the buckling load and displacement were more accurately predicted than for the 1% imperfection by both reduced-scale configurations. For the 50% imperfection, the typical buckling behavior with load drop was not observed, thus complicating the comparison.

Generally, it can be concluded that the scaling methodology allows to design reduced-scale conical shells, which can accurately predict the behavior of their full-scale shell. The stiffness was accurately predicted in all considered cases with a maximum discrepancy of 2.7%. It may be difficult in some cases to find a shell of convenient size for testing, which also complies with the laminate assumptions. The prediction accuracy is believed to be mainly affected by not being able to satisfy all scaling parameters simultaneously, by non-negligible flexural anisotropy parameters and by differences in imperfection sensitivity between full-scale and reduced-scale shells. For sandwich shells, the transverse shear compliance can also affect the results. Their effects on the prediction accuracy can partially balance each other out, such that accurate results are obtained, even for larger imperfections and in the postbuckling regime. Out of the evaluated parameters, the radial displacement was most difficult to predict, which was attributed to the membrane prebuckling assumption and neglecting the presence of imperfections in the methodology.

Although the potential of the scaling methodology has been proven, it is important to make the methodology more applicable to real conical shells. Therefore, the effect of imperfections on the prediction accuracy should be investigated further. More realistic, measured imperfections could be applied to evaluate the imperfection sensitivities of the full-scale and reduced-scale shells. This is especially important if the two shells have a different stacking sequence or laminate structure, as it was the case for the full-scale sandwich shell. Next, inclusion of flexural anisotropy and transverse shear effects could make the methodology more suitable for other laminate types and for sandwich conical shells, which are commonly used in launch vehicles. In addition, the effects of stiffness variations, intrinsically present in composite conical shells, should be looked into to evaluate their effect on the scalability. This could also be extended to include the effects of stiffeners, pad-ups and cut-outs. Finally, the methodology should be validated through experimental testing of both the full-scale and reduced-scale shell.

References

[1] B. Dunbar. Moon to Mars overview, 2020. Accessed on: 19/04/2021. URL: https://www.nasa.gov/topics/moon-to-mars/overview.

[2] SpaceX. Mars & beyond: the road to making humanity multiplanetary, 2020. Accessed on: 19/04/2021. URL: https://www.spacex.com/human-spaceflight/mars/index.html.

[3] V.I. Weingarten, P. Seide, and J.P. Peterson. Buckling of thin-walled truncated cones (SP8019). Technical Report 19690014753, NASA Langley Research Center, Hampton, Virginia, 1968.

[4] M.K. Chryssanthopoulos, C. Poggi, and A. Spagnoli. Buckling design of conical shells based on validated numerical models. *Thin-Walled Structures*, 31(1):257–270, 1998. doi:10.1016/S0263-8231(98)00006-8.

[5] O. Ifayefunmi. A survey of buckling of conical shells subjected to axial compression and external pressure. *Journal of Engineering Science and Technology Review*, 7(2):182–189, 2014. doi:10.25103/jestr.072.27.

[6] R. Khakimova. *Ply topology based design concept for composite truncated cones manufactured by tape laying*. PhD dissertation, Technical University of Braunschweig, 2017.

[7] E. Ventsel and T. Krauthammer. *Thin plates and shells: theory, analysis, and applications*. CRC Press, New York, United States of America, 2001.

[8] D.O. Brush and B.O. Almroth. *Buckling of bars, plates, and shells*. McGraw-Hill, 1975.

[9] Y. Goldfeld and J. Arbocz. Elastic buckling of laminated conical shells using a hierarchical high-fidelity analysis procedure. *Journal of Engineering Mechanics*, 132(12):1335–1344, 2006. doi:10.1061/(ASCE)0733-9399(2006)132:12(1335).

[10] P. Seide. Axisymmetric buckling of circular cones under axial compression. *Journal of Applied Mechanics*, 23(4):625–628, 1956.

[11] A. Stawiarski, M. Chwał, M. Barski, and A. Muc. The influence of the manufacturing constraints on the optimal design of laminated conical shells. *Composite Structures*, 235:111820, 2020. doi:10.1016/j.compstruct.2019.111820.

[12] M. E. Kazemi, M. A. Kouchakzadeh, and M. Shakouri. Stability analysis of generally laminated conical shells with variable thickness under axial compression. *Mechanics of Advanced Materials and Structures*, 27(16):1373–1386, 2020. doi:10.1080/15376494.2018.1511016.

[13] R. Khakimova, D. Wilckens, J. Reichardt, R. Zimmermann, and R. Degenhardt. Buckling of axially compressed CFRP truncated cones: Experimental and numerical investigation. *Composite Structures*, 146:232–247, 2016. doi:10.1016/j.compstruct.2016.02.023.

[14] A. Casaburo, G. Petrone, F. Franco, and S. De Rosa. A review of similitude methods for structural engineering. *Applied Mechanics Reviews*, 71(3), 2019. doi:10.1115/1.4043787.

[15] C.P. Coutinho, A.J. Baptista, and J. Dias Rodrigues. Reduced scale models based on similitude theory: A review up to 2015. *Engineering Structures*, 119:81–94, 2016. doi:10.1016/j.engstruct.2016.04.016.

[16] R. Khakimova, R. Zimmermann, D. Wilckens, K. Rohwer, and D. Degenhardt. Buckling of axially compressed CFRP truncated cones with additional lateral load: Experimental and numerical investigation. *Composite Structures*, 157:436–447, 2016. doi:10.1016/j.compstruct.2016.08.011.

[17] W.T. Koiter. *Over de stabiliteit van het elastisch evenwicht (The stability of elastic equilibrium)*. PhD dissertation, Technische Hooge School Delft, 1945.

[18] H.N.R. Wagner, C. Hühne, and R. Khakimova. Towards robust knockdown factors for the design of conical shells under axial compression. *International Journal of Mechanical Sciences*, 146-147:60–80, 2018. doi:10.1016/j.ijmecsci.2018.07.016.

[19] M.F. Di Pasqua, R. Khakimova, S.G.P. Castro, M.A. Arbelo, A. Riccio, A. Raimondo, and R. Degenhardt. Investigation on the geometric imperfections driven local buckling onset in composite conical shells. *Applied Composite Materials*, 23:879–897, 2016. doi:10.1007/s10443-016-9490-7.

[20] D.W. Sleight, A. Satyanarayana, and M.R. Schultz. Buckling imperfection sensitivity of conical sandwich composite structures for launch-vehicles. In *2018 AIAA/ASCE/AHS/ASC Structures, Structural Dynamics, and Materials Conference*. American Institute of Aeronautics and Astronautics, 2018. doi:10.2514/6.2018-1696.

[21] J. Arbocz and J.H. Starnes Jr. Future directions and challenges in shell stability analysis. *Thin-Walled Structures*, 40(9):729–754, 2002. doi:10.1016/S0263-8231(02)00024-1.

[22] B. Kriegesmann, R. Rolfes, C. Hühne, J. Teßmer, and J. Arbocz. Probabilistic design of axially compressed composite cylinders with geometric and loading imperfections. *International Journal of Structural Stability and Dynamics*, 10(04):623–644, 2010. doi:10.1142/S0219455410003658.

[23] M.K. Chryssanthopoulos and A. Spagnoli. The influence of radial edge constraint on the stability of stiffened conical shells in compression. *Thin-Walled Structures*, 27(2):147–163, 1997. doi:10.1016/S0263-8231(96)00035-3.

[24] J. Kepple, M.T. Herath, G. Pearce, B. Gangadhara Prusty, R. Thomson, and R. Degenhardt. Stochastic analysis of imperfection sensitive unstiffened composite cylinders using realistic imperfection models. *Composite Structures*, 126:159–173, 2015. doi:10.1016/j.compstruct.2015.02.063.

[25] Y. Goldfeld. Imperfection sensitivity of laminated conical shells. *International Journal of Solids and Structures*, 44(3):1221–1241, 2007. doi:10.1016/j.ijsolstr.2006.06.016.

[26] Y. Goldfeld, J. Arbocz, and A. Rothwell. Design and optimization of laminated conical shells for buckling. *Thin-Walled Structures*, 43(1):107–133, 2005. doi:10.1016/j.tws.2004.07.003.

[27] Y. Goldfeld and J. Arbocz. Buckling of laminated conical shells given the variations of the stiffness coefficients. *AIAA Journal*, 42(3):642–649, 2004. doi:10.2514/1.2765.

[28] A.W. Blom. *Structural Performance of Fiber-Placed Variable Stiffness Composite Conical and Cylindrical Shells*. PhD dissertation, Delft University of Technology, 2010.

[29] A.A. Naderi, G.H. Rahimi, and M. Arefi. Influence of fiber paths on buckling load of tailored conical shells. *Steel and Composite Structures*, 16(4):375–387, 2014. doi:10.12989/SCS.2014.16.4.375.

[30] M. Hilburger, W. Haynie, A. Lovejoy, M. Roberts, J. Norris, W. Waters, and H. Herring. Sub-scale and full-scale testing of buckling-critical launch vehicle shell structures. In *53rd AIAA/ASME/ASCE/AHS/ASC Structures, Structural Dynamics and Materials Conference*. American Institute of Aeronautics and Astronautics, 2012. doi:10.2514/6.2012-1688.

[31] R. Degenhardt. New robust design guideline for imperfection sensitive composite launcher structures. In *CEAS 2011 International Conference of the European Aerospace Societies*. CEAS Air&Space Conference, 2011.

[32] ECSS ESA. *ECSS space engineering: Buckling of structures ECSS-E-HB-32-24A*. ESA Requirements and Standards Division, Noordwijk, first edition, 2010. URL: https://ecss.nl/hbstms/ecss-e-hb-32-24a-buckling-of-structures/.

[33] European Convention for Constructional Steelwork. *Enhancement of ECCS design recommendations and development of Eurocode 3 parts related to shell buckling*. Office for Official Publications of the European Communities, Luxembourg, 1998.

[34] M.R. Schultz, D.W. Sleight, N.W. Gardner, M.T. Rudd, M.W. Hilburger, T. Palm, and N.J. Oldfield. Test and analysis of a buckling-critical large-scale sandwich composite cylinder. Technical Report 20180002092, NASA Langley Research Center, Hampton, Virginia, 2018. doi:10.2514/6.2018-1693.

[35] S.G.P. Castro, R. Zimmermann, M.A. Arbelo, R. Khakimova, M.W. Hilburger, and R. Degenhardt. Geometric imperfections and lower-bound methods used to calculate

knock-down factors for axially compressed composite cylindrical shells. *Thin-Walled Structures*, 74:118–132, 2014. doi:10.1016/j.tws.2013.08.011.

[36] B. Wang, X. Ma, P. Hao, Y. Sun, K. Tian, G. Li, K. Zhang, L. Jiang, and J. Guo. Improved knockdown factors for composite cylindrical shells with delamination and geometric imperfections. *Composites Part B: Engineering*, 163:314–323, 2019. doi:10.1016/j.compositesb.2018.11.049.

[37] H.N.R. Wagner, C. Hühne, and S. Niemann. Constant single-buckle imperfection principle to determine a lower bound for the buckling load of unstiffened composite cylinders under axial compression. *Composite Structures*, 139:120–129, 2016. doi:10.1016/j.compstruct.2015.11.047.

[38] C. Hühne, R. Rolfes, and J. Tessmer. A new approach for robust design of composite cylindrical shells under axial compression. In *Proceedings of European Conference on Spacecraft Structures, Materials & Mechanical Testing*, pages 140.1–140.8, Noordwijk, the Netherlands, 2005.

[39] P. Hao, B. Wang, G. Li, Z. Meng, K. Tian, D. Zeng, and X. Tang. Worst multiple perturbation load approach of stiffened shells with and without cutouts for improved knockdown factors. *Thin-Walled Structures*, 82:321–330, 2014. doi:10.1016/j.tws.2014.05.004.

[40] A. Meurer, B. Kriegesmann, M. Dannert, and R. Rolfes. Probabilistic perturbation load approach for designing axially compressed cylindrical shells. *Thin-Walled Structures*, 107:648–656, 2016. doi:10.1016/j.tws.2016.07.021.

[41] B. Kriegesmann, R. Rolfes, C. Hühne, and A. Kling. Fast probabilistic design procedure for axially compressed composite cylinders. *Composite Structures*, 93(12):3140–3149, 2011. doi:10.1016/j.compstruct.2011.06.017.

[42] M. Alfano and C. Bisagni. Probabilistic buckling analysis of sandwich composite cylindrical shells based on measured imperfections. In *58th AIAA/ASCE/AHS/ASC Structures, Structural Dynamics, and Materials Conference*. American Institute of Aeronautics and Astronautics, 2014. doi:10.2514/6.2017-0886.

[43] R. Khakimova, F. Burau, R. Degenhardt, M. Siebert, and S.G.P. Castro. Design and manufacture of conical shell structures using prepreg laminates. *Applied Composite Materials*, 23:289–312, 2016. doi:10.1007/s10443-015-9461-4.

[44] I.U. Cagdas. Optimal design of variable stiffness laminated composite truncated cones under lateral external pressure. *Ocean Engineering*, 145:268–276, 2017. doi:10.1016/j.oceaneng.2017.09.011.

[45] Dassault Systemes. *Abaqus Analysis 6.14 User's Guide*. Dassault Systemes, Providence, Rhode Island, 2016.

[46] M.F. Di Pasqua, R. Khakimova, S.G.P. Castro, M.A. Arbelo, A. Riccio, and R. Degenhardt. The influence of geometrical parameters on the buckling behavior of conical shell by the single perturbation load approach. *Applied Composite Materials*, 22(1):405–422, 2015. doi:10.1007/s10443-014-9414-3.

[47] I. Uriol Balbin, C. Bisagni, M.R. Schultz, and M.W. Hilburger. Scaling methodology applied to buckling of sandwich composite cylindrical shells. *AIAA Journal*, 58(8):3680–3689, 2020. doi:10.2514/1.J058999.

[48] G.J. Simitses and J. Rezaeepazhand. Structural similitude and scaling laws for laminated beam-plates. Technical Report 19920022667, NASA Langley Research Center, Hampton, Virginia, 1992.

[49] E. Szücs. *Similitude and Modelling*. Elsevier, New York, New York, 1980.

[50] G.J. Simitses and J. Rezaeepazhand. Structural similitude for laminated structures. *Composites Engineering*, 3(7):751–765, 1993. doi:10.1016/0961-9526(93)90094-Z.

[51] G. J. Simitses, J.H. Starnes, and J. Rezaeepazhand. *Structural similitude and scaling laws for plates and shells: A review*, pages 295–310. Springer Netherlands, Dordrecht, 2002. doi:10.1007/0-306-46954-5_19.

[52] K.E. Jackson, editor. *Workshop on Scaling Effects in Composite Materials and Structures*, volume 1, Hampton, Virginia, 1994. NASA Langley Research Center, National Aeronautics and Space Administration.

[53] J.J. Catherine and J.S. Mixson. Comparison of experimental vibration characteristics obtained from a 1/5-scale model and from a full-scale Saturn SA-1. Technical Report 19650001201, NASA Langley Research Center, Hampton, Virginia, 1964.

[54] E.L. Peele, H.W. Leonard, and Leadbetter S.A. Lateral vibration characteristics of the 1/10-scale Apollo/Saturn V replica model. Technical Report 19690013567, NASA Langley Research Center, Hampton, Virginia, 1970.

[55] F.A. Penning. Use of dynamic scale models to determine launch vehicle characteristics. Technical Report 19690031776, NASA Marshall Space Flight Center, Huntsville, Alabama, 1969.

[56] S.A. Leadbetter, W.B. Stephens, J.L. Sewall, J.W. Majka, and J.R. Barrett. Vibration characteristics of 1/8-scale dynamic models of the Space Shuttle solid-rocket boosters. Technical Report 19760016541, NASA Langley Research Center, Hampton, Virginia, 1976.

[57] D.A. Davis, M.J. Gronet, M.K. Tan, and J. Thorne. *Conceptual design and analysis of a dynamic scale model of the space station freedom*. NASA contractor report. NASA Langley Research Center, Hampton, Virginia, 1994.

[58] P.E. McGowan, M. Javeed, and H.H. Edighoffer. Status of DSMT research program. Technical Report 19910011192, NASA Langley Research Center, Hampton, Virginia, 1991.

[59] P. Jiang, W. Wang, and G.J. Zhang. Size effects in the axial tearing of circular tubes during quasi-static and impact loadings. *International Journal of Impact Engineering*, 32(12):2048–2065, 2006. doi:10.1016/j.ijimpeng.2005.07.001.

[60] Y. Zhu, Y. Wang, Z. Luo, Q. Han, and D. Wang. Similitude design for the vibration problems of plates and shells: A review. *Frontiers of Mechanical Engineering*, 12(2):253–264, 2017. doi:10.1007/s11465-017-0418-1.

[61] J. Rezaeepazhand and G. Simitses. Design of scaled down models for stability and vibration studies. In *35th Structures, Structural Dynamics, and Materials Conference*. American Institute of Aeronautics and Astronautics, 1993. doi:10.2514/6.1994-1572.

[62] J. Rezaeepazhand, G.J. Simitses, and J.H. Starnes. Scale models for laminated cylindrical shells subjected to axial compression. *Composite Structures*, 34(4):371–379, 1996. doi:10.1016/0263-8223(95)00154-9.

[63] A. Tabiei and G. Simitses. Scaled down imperfection sensitive composite cylindrical shells under axial compression and lateral pressure. In *38th Structures, Structural Dynamics, and Materials Conference*. American Institute of Aeronautics and Astronautics, 1997. doi:10.2514/6.1997-1250.

[64] V. Ungbhakorn and N. Wattanasakulpong. Structural similitude and scaling laws of anti-symmetric cross-ply laminated cylindrical shells for buckling and vibration experiments. *International Journal of Structural Stability and Dynamics*, 7(4):609–627, 2007. doi:10.1142/S0219455407002459.

[65] C.P. Coutinho, A.J. Baptista, and J. Dias Rodriges. Modular approach to structural similitude. *International Journal of Mechanical Sciences*, 135:294–312, 2018. doi:10.1016/j.ijmecsci.2017.11.005.

[66] S.L. Canfield, J. Peddieson, and G. Garbe. Similarity rules for scaling solar sail systems. Technical Report 20040161547, NASA Marshall Space Flight Center, Huntsville, Alabama, 2010.

[67] S. Torkamani, H.M. Navazi, A.A. Jafari, and M. Bagheri. Structural similitude in free vibration of orthogonally stiffened cylindrical shells. *Thin-Walled Structures*, 47(11):1316–1330, 2009. doi:10.1016/j.tws.2009.03.013.

[68] M.W. Hilburger, C.A. Rose, and J.H. Starnes, Jr. Nonlinear analysis and scaling laws for noncircular composite structures subjected to combined loads. In *42nd AIAA/ASME/ASCE/AHS/ASC Structures, Structural Dynamics, and Materials Conference*. American Institute of Aeronautics and Astronautics, 2001. doi:10.2514/6.2001-1335.

[69] M. Stein. Postbuckling of orthotropic composite plates loaded in compression. *AIAA Journal*, 21(12):1729–1735, 1983. doi:10.2514/6.1982-778.

[70] M.P. Nemeth. Nondimensional parameters and equations for nonlinear and bifurcation analyses of thin anisotropic quasi-shallow shells. Technical Report 20100027403, NASA Langley Research Center, Hampton, Virginia, 2010.

[71] M.R. Schultz and M.P. Nemeth. Buckling imperfection sensitivity of axially compressed orthotropic cylinders. In *51st AIAA/ASME/ASCE/AHS/ASC Structures, Structural dynamics, and Materials Conference*. American Institute of Aeronautics and Astronautics, 2010. doi:10.2514/6.2010-2531.

[72] V. Ungbhakorn and P. Singhatanadgid. A scaling law for vibration response of laminated doubly curved shallow shells by energy approach. *Mechanics of Advanced Materials and Structures*, 16(5):333–344, 2009. doi:10.1080/15376490902970430.

[73] W. Yu and Z.L. Li. Structural similitude for prestressed vibration and buckling of eccentrically stiffened circular cylindrical panels and shells by energy approach. *International Journal of Structural Stability and Dynamics*, 16(10):1550074, 2016. doi:10.1142/S0219455415500741.

[74] S. De Rosa, F. Franco, X. Li, and T. Polito. A similitude for structural acoustic enclosures. *Mechanical Systems and Signal Processing*, 30:330–342, 2012. doi:10.1016/j.ymssp.2012.01.018.

[75] U. Cho and K.L. Wood. Empirical similitude method for the functional test with rapid prototypes. In *International Solid Freeform Fabrication Symposium*. University of Texas at Austin, 1997. URL: http://hdl.handle.net/2152/71434.

[76] H. Yılmaz, E. Özyurt, A. Önder, and P. Tomek. Elastic limit load estimation including similarity approach for different end conditioned conical shells with high semi-vertex angle under axial compression. *Thin-Walled Structures*, 149:106543, 2020. doi:10.1016/j.tws.2019.106543.

[77] M.P. Nemeth. Nondimensional parameters and equations for buckling of symmetrically laminated thin elastic shallow shells. Technical Report 19910013084, NASA Langley Research Center, Hampton, Virginia, 1991.

[78] A.E.H. Love. *A treatise on the mathematical theory of elasticity*. Cambridge University Press, 1892.

[79] L.H. Donnell. *Beams, plates, and shells*. McrGraw-Hill, New York, United States of America, 1976.

[80] K.M. Mushtari. Certain generalizations of the theory of thin shells. *Izv Fiz Mat ob-va pri Kazan Univ*, 11(8), 1938.

[81] V.Z. Vlasov. *General theory of shells and its application in engineering*. NASA TT F-99, 1964.

[82] M. Jabareen and I. Sheinman. Effect of the nonlinear pre-buckling state on the bifurcation point of conical shells. *International Journal of Solids and Structures*, 43(7):2146–2159, 2006. doi:10.1016/j.ijsolstr.2005.05.024.

[83] C. Kassapoglou. *Design & analysis of composite structures (with applications to aerospace structures)*. Wiley, Hoboken, New Jersey, 2010.

[84] R.M. Jones. *Buckling of Bars, Plates, and Shells*. Bull Ridge Publishing, 2006.

[85] K. Schiffner. *Spannungs- und Stabilitätsuntersuchungen an dünnwandigen Kegelschalen bei axialsymmetrischen Randbedingungen*. PhD dissertation, RWTH Aachen University, 1966.

[86] G.Q. Zhang. *Stability analysis of anisotropic conical shells*. PhD dissertation, Delft University of Technology, 1993.

[87] B. Dunbar. NASA explores with Space Launch System, 2021. Accessed on: 29/03/2021. URL: https://www.nasa.gov/exploration/systems/sls/index.html.

[88] T. Reckart. NASA Space Launch System Universal Stage Adapter, 2020. Accessed on: 14/04/2021. URL: https://www1.grc.nasa.gov/space/usa/.

[89] M. Rudd Tillotson, M.R. Schultz, Waters A.W., N.W. Gardner, and C. Bisagni. Buckling testing of a subscale composite cylinder. In *AIAA Scitech 2021 Forum*. American Institute of Aeronautics and Astronautics, 2021. doi:10.2514/6.2021-0205.

[90] M. Bauccio. *ASM metals reference book*. American Society for Metals International, Metals park, Ohio, 1993.

[91] K. Marlett, Y. Ng, and J. Tomblin. Hexcel 8552 IM7 unidirectional prepreg 190 gsm & 35%RC qualification material property data report. Technical report, National Center for Advanced Materials Performance, CAM-RP-2009-015 Rev. A, Wichita, KS, 2011.

[92] C.D. Reese and C.W. Bert. Simplified design equations for buckling of axially compressed sandwich cylinders with orthotropic facings and core. *Journal of Aircraft*, 6(6):515–519, 1969. doi:10.2514/3.44098.

[93] A. Przekop, M.R. Schultz, and M.W. Hilburger. Design of buckling-critical large-scale sandwich composite cylinder test articles. In *2018 AIAA/ASME/ASCE/AHS/ASC Structures, Structural Dynamics, and Materials Conference*. American Institute of Aeronautics and Astronautics, 2018. doi:10.2514/6.2018-1694.

[94] A. Orifici and C. Bisagni. Perturbation-based imperfection analysis for composite cylindrical shells buckling in compression. *Composite Structures*, 106:520–528, 2013. doi:10.1016/j.compstruct.2013.06.028.

[95] J. Rezaeepazhand, A. Tabiei, and G. Simitses. Imperfection sensitivity of scaled down laminated cylindrical shells. In *37th Structure, Structural Dynamics and Materials Conference*. American Institute of Aeronautics and Astronautics, 1996. doi:10.2514/6.1996-1474.

[96] R. Khakimova, C.J. Warren, R. Zimmermann, S.G.P. Castro, M.A. Arbelo, and R. Degenhardt. The single perturbation load approach applied to imperfection sensitive conical composite structures. *Thin-Walled Structures*, 84:369–377, 2014. doi:10.1016/j.tws.2014.07.005.

[97] C. Bisagni. Numerical analysis and experimental correlation of composite shell buckling and post-buckling. *Composites Part B: Engineering*, 31(8):655–667, 2000. doi:10.1016/S1359-8368(00)00031-7.